Characterisation and Optimisation of Novel Sol-Gel Materials for Luminescence-Based O_2 Sensing

by
Clare Higgins B.Sc. (Hons)

A thesis presented to Dublin City University
For the Degree of Doctor of Philosophy

Supervisor:
Prof. Colette McDonagh
School of Physical Sciences,
Dublin City University.

January 2007

Declaration

I hereby certify that this material, which I now submit for assessment on the programme of study leading to the award of Doctor of Philosophy is entirely my own work and has not been taken from the work of others save and to the extent that such work has been cited and acknowledged within the text of my work.

Signed: Claire Higgins (Candidate)
ID No.: 95405909
Date: 19/6/2007

Dedication

To Mam and Dad

Acknowledgements

A second, and possibly third volume of this thesis would be required if I were to attempt to adequately thank each and every person who has given me their time, lab equipment, advice, encouragement, support during the lows and their company to share in the highs over the long course of the last four years in DCU. These acknowledgements serve as a brief thank you to you all and a quick mention for a few.

First and foremost, my supervisor Colette for everything but most of all her generosity with her time and ideas, both of which were central to this work. Thanks too to Brian for the opportunity to work here in OSL. Many, many thanks to all in OSL and the extended scientific community throughout DCU who have contributed to this thesis, especially Mary Pryce for the lifetime measurements and also Henry Barry for both the initial ellipsometry training and his ongoing support with day-to-day issues. In particular, I must thank the Tübingham gang and Deepa et al. who make life here all the more lighthearted. Special thanks to my office buddy Dorota for all the chemistry advice, I would have been hopelessly lost without you.

Now down to brass tacks, my great mates, my college-part-one gang from AP. You guys are the best. Thanks so much for understanding the madness of the past months and my virtual disappearance from the social scene over the last few years, and indeed for standing me the beers when I did venture out. I'm so very much looking forward to celebrating the completion of this thesis with you guys.

To my old school Swords crowd, I don't get to see y'all near as often as I should, thanks for all the good times. Most of all the Fibbers crowd - Peter Ward and all the McCanney clan. A special mention for Rose, a true lady and my favorite employer to date, thanks for always showing an interest. A mention also for the late but wonderfully great Michael McCanney, who was always such great company, you are missed terribly but will never be forgotten.

My extended family for all the craic, good times, the pearls of wisdom from Kathleen and the late night pearls of wisdom from Manus!

To my fabulous friend, beautician and ex-Logi-bod, Mags, thanks for all the tea&smarties&chats sessions.

To the glamorous Eimear O'Reilly who is another tea&chats girl, thanks for your very calming influence. Thanks to Breada too for all the top-notch Friday feasts.

Thanks to the Brackens for all their support and kindness, especially for feeding my gardening habit.

My bud Emma-Rose, party girl, domestic goddess, fashionista and multi-media genius, truly a girl's best friend, thanks for everything my girl. Now this is done, I'm so looking forward to helping organise your wedding to the lovely Comhghall Casey.

My wee sis JeanBean, thanks for nothing neighbour's kid. No, no, joking of course, I'm sure you helped, just can't think how. :o)

To the gorgeous man in my life, Nigel, a v.big thank you, for all of it. You've gone way above and beyond the call of boyfriend duty. You must have wondered at times if this college business would ever end. Well, get the champagne on ice Darlin', as it's nearly done now!

To Mam and Dad, the wonder-parents. You guys have given me so much. From practical stuff like late-night lifts home from The Grove, Western Union wires to all corners of the globe, and everything right up to proof reading this thesis. But even more important than that stuff, you've given me an interest in so many aspects of life and encouraged and supported everything I've done (with the possible exception of the blond hair phase). I can't possibly tell you how much it's all appreciated or ever thank you properly for that, but dedicate this thesis to you both as a gesture.

Contents

Abstract

Current sensor trends, such as multi-analyte measurement, miniaturisation and printability, are important drivers for materials to be used in optical chemical sensors. In recent years, there has been a focus on sol-gel materials for sensor applications due to their excellent optical properties, ease of entrapment of analyte-sensitive dyes and the compatibility of the sol-gel process with a range of deposition techniques. This study focuses on the fabrication, characterisation and optimisation of novel sol-gel ORMOSIL (ORganically MOdified SILicate) matrices for luminescence-based O_2 sensing. The O_2 sensing scheme is based on the luminescence quenching of the highly O_2-sensitive ruthenium complex [Ru(II)-tris(4,7-diphenyl-1,10-phenanthroline) dichloride], entrapped in a porous sol-gel film. A phase fluorometric detection scheme was employed which capitalised on the inherent advantages of frequency-domain rather than time- or intensity-domain measurements. This study focuses on optimisation of the O_2 sensor response under a variety of headings including, sensitivity, dynamic range, photobleaching effects and sensor interferences caused by solvent vapour. Key film parameters include porosity and film hydrophobicity. These parameters are intimately related to the precursors used, in addition to sol-gel processing parameters. The xerogel microstructure was investigated using spectroscopic ellipsometry. O_2 diffusion coefficients were also measured and the results were correlated to porosity and sensor sensitivity data. A study of the phase fluorometric response as a function of LED modulation frequency highlighted the importance of optical filter selection in order to produce the optimum sensor response. It is clear from this work that the O_2 sensitivity of the film can be tailored via the sol-gel precursor used. Furthermore, there is a general correlation between the hydrophobicity of the film and the length of the precursor alkyl chain. Good correlation was obtained between porosity, diffusion coefficient and O_2 sensing data. Finally, the work highlights the versatility of the sol-gel route to provide application-specific materials, thereby providing solutions to a variety of sensing problems.

List of Figures

List of Tables

Abbreviations and Symbols

Γ	emissive rate
Δ	change in phase that occurs upon relfection or difference
Ψ	change in amplitude that occurs upon relfection
γ	surface tension
δ_p, δ_s	phase of p- or s-component, relative to the other
ϵ_0	rate of evaporation
λ	wavelength
υ_0	kinematical viscosity
ϕ	phase angle
ϕ_R	resultant phase angle
ϕ_S	sample signal phase angle
ϕ_0/ϕ_{100}	ratio of the phase angle recorded at 0 % O_2 concentration to that recorded at 100 % O_2 concentration
ρ	density or ratio of Fresnel reflection coefficients
τ	excited state lifetime
τ_{obs}	observed excited state lifetime
τ_0	excited state lifetime in the absence of O_2
ω	angular frequency or angular velocity
A	absorbtion or average intensity of the emission
A_p	total surface area of the pores
a	average intensity of incident light
BET	Brunauer-Emmett-Teller
B	modulated amplitude of the emission
b	modulated amplitude of incident light
CCD	charge coupled device
CMOS	complementary metaloxidesemiconductor
c_0	initial sol concentration
D	diffusion coefficient
ETEOS	ethyltriethoxysilane
F	fluoresence

FTIR	Fourier transform infra-red (spectroscopy)
f	modulation frequency
f_{opt}	optimum modulation frequency
f_i	fractional contribution of total emission of luminophore located at site i
GSS	Gas Sensing Solutions
g	spin statistical factor or acceleration due to gravity
HCl	hydrochloric acid
HNO_3	nitric acid
h	thickness
h_f	final film thickness
I	luminescence intensity
I_0	luminescence intensity in the absence of O_2
IC	internal conversion
IR	infra-red
ISC	inter-system crossing
K_S	static quenching constant
K_{SV}	Stern-Volmer constant
K_{SVi}	Stern-Volmer constant associated with luminophore site i
k_{nr}	rate of non-radiative decay
k_q	bimolecular quenching constant
L	uncomplexed luminophore population
MLC	metal-ligand complex
^{3}MLCT	triplet metal-to-ligand charge transfer state
MTEOS	methyltriethoxysilane
m	demodulation factor
N	Avogadro's number
n_{ads}	refractive index of adsorbent
n_{dry}	refractive index at under N_2, i.e. dry conditions
n_f	refractive index of film
n_p	refractive index of pores
n_s	refractive index of solid skeleton
$n_{skeletal}$	refractive index of solid skeleton

n_{wet}	refractive index at saturated conditions
n_0	refractive index at 0 % relative humidity
ORMOSIL	organically modified silicate
OTEOS	octyltriethoxysilane
P	phosphorescence or permeability
PDMS	polydimethylsiloxane
PEM	photo-elastic modulator
PhTEOS	phenyltriethoxysilane
PMT	photomultiplier tube
PSD	pore size distribution
PSU	polysulfone
PTEOS	propyltriethoxysilane
PTMOS	propyltrimethoxysilane
precursor	starting material in the sol-gel process
pO_2	O_2 partial pressure
Q	quencher or uncomplexed quencher concentration
[Q]	quencher concentation
R	(in the context of the Stern-Volmer equation) luminophore-quencher interaction distance
R	(in the context of organosilicon precursor formula) Et (in this work)
R'	(in the context of organosilicon precursor formula) the organic group
R_h	average pore radius
R_p, R_s	effective Fresnel reflection coefficients for multiple layer systems (the summation of all r_p or r_s for each layer)
RH	relative humidity
R-value	molar ration of water to precursor
$[Ru(dpp)]^{2+}$	Ru(II)-tris(4,7-diphenyl-1,10-phenanthroline) dichloride
r_p, r_s	Fresnel reflection coefficients for single layer sytems
S	solubility
S_i	singlet energy state
SOPRA	a surface metrology company, based in France and the USA (http://www.sopra-sa.com)

SUNY	State University of New York
SQ	static quenching
T_i	triplet energy state
TEOS	tetraethoxysilane
TFP-TMOS	3,3,3-trifluoropropyltrimethoxysilane
TQ	transient quenching
t_{90}	time taken for luminescence intensity to decrease (or increase) to 90 % of its original value
U	dip-speed
UV	ultra-violet
V_{ads}	volume of adsorbent in pores
V_p	volume porosity
VSI	vertical scanning interferometry
xerogel	a dried gel

Chapter 1

Introduction

1.1 Introduction

A sensor is defined as a device capable of continuously monitoring a physical parameter or concentration of an analyte. Sensors extend to virtually every facet of modern life. From medicine, where monitoring physiological parameters provides vital diagnostic information in health care, to environmental temperature sensors monitoring phenomena such as global warming and even to recreational applications such as force sensing technology in video games. Additionally, the current market for sensors is forecast to grow as industry requirements for intelligent networked systems increases [1, 2].

This work centers on chemical sensors, which Wolfbeis et al. have defined as "miniaturised analytical devices that can deliver real-time and on-line information on the presence of specific compounds or ions in complex samples" [3]. To give the most simplified example of a chemical sensor, a sensor element is placed into the environment under examination, returning a signal which may be interpreted in terms of analyte concentration.

The different types of sensor may be classified in terms of the method of transduction, such as, mechanical, electrochemical and optical. Optical sensors are becoming increasingly popular in chemical sensing, due to the inert nature of the optical transduction signal which avoids the interference

issues associated with electrical signals. This is the sensor class of interest to this work.

In particular, this work is concerned with the development and optimisation of optical sol-gel-derived O_2 sensor elements for use in monitoring bio-processes. For example, O_2 is an important parameter to monitor during the fermentation process, since successful fermentation and quality control depends on optimum conditions being maintained throughout the process.

In this work, the transparent, porous sol-gel-based materials provides a host support medium in which a luminescent ruthenium-based compound is immobilised. The luminescence is quenched through interaction with O_2 molecules, that access the compound via the pores in the sol-gel-based material. The sol-gel approach to glass production is used here, as its versatile nature enables glasses to be customised to meet the requirements of the desired application.

Since the sensors in this work are intended to be supplied commercially, they have been produced with a reproducible, simple fabrication process which lends itself to mass production. In addition, the optoelectronic components used to implement the sensing procedure are low-cost, widely available and suitable for miniaturisation.

This thesis details the fabrication of the sol-gel-based sensor elements and, through various characterisation methods, follows the processes by which they have been optimised for the bio-pharm market and also presents the implementation of the phase fluorometric sensing technique.

1.2 Optical sensing

Sensors are classified in terms of transduction method, such as, acoustic, electrical, electrochemical, mechanical, optical and thermal. The transduction method of interest in this work is optical.

Optical sensors operate by monitoring an optical property or signal which is dependent on the parameter of interest. Optical sensors have been developed

to monitor a range of physical (temperature [4], pressure [5], rotation [6]), biological (bacteria [7], hormones [8]) and chemical (various chemical species [9–12]) parameters. Chemical sensing is the focus of this work, where O_2 is the analyte of interest.

Optical, rather than the other previously mentioned transduction techniques, is particularly suited to chemical sensing, for the following reasons:

- the sensing mechanisms are generally reversible and the analyte is not consumed.
- widely available optical fibre allows an optical signal to be transmitted great distances via the optic fibre to the detection electronics. This allows for remote sensing and for the possibility of sensing in harsh environments, for example where temperatures are high, or in locations were access is an issue.
- unlike an electrical transduction signal an optical signal does not present the risk of sparking, and it eliminates the possibility of electrical interference.
- optical sensing techniques facilitate a range of design possibilities for sensor platforms, since they exploit the availability of a wide range of low-cost opto-electronic devices allowing miniaturisation and also allowing for the design of portable sensor systems. The low cost allows for the possibility of disposable sensors.
- patterns of sensor elements, each sensitive to particular substances, may be imaged via techniques such as Charge-Coupled Device (CCD) cameras, enabling multi-analyte sensing.

Optical chemical sensors may be subclassified by the nature of the optical signal. The most widely reported groups are refractometric-, reflection-, absorbance- and luminescence-based sensors. Refractometric-based sensors

monitor an analyte-dependent change in refractive index [13]. Reflection-based sensors monitor changes in the analyte-dependent reflectance spectrum of a suitable compound [14]. Absorbance-based sensors operate on the principle that each chemical species absorbs at a particular wavelength [15]. Luminescence-based sensors either monitor the intrinsic luminescence of the target analyte [16] or an analyte-sensitive luminescence property of an indicator complex [17]. The sensor elements in this work employ luminescence-based sensing to monitor gaseous O_2 concentration via variations in the luminescence signal of an indicator complex.

1.2.1 Luminescence-based sensing

The transduction signal in the sensors developed in this work, is a luminescence signal arising from the excited-state of a ruthenium-based complex. This signal is quenched through interaction with O_2 molecules, which reduces both the excited-state lifetime and also the intensity of the emitted luminescence. As such, O_2 concentration may be determined by monitoring variations in the excited-state lifetime or the intensity of the luminescence signal.

Sensing based on luminescence properties offers several advantages over the alternative optical sensing methods, such as refractometric- or absorbance-based methods. These advantages include:

- low levels of analyte concentration may be more conveniently determined. Luminescence is an intrinsically more sensitive process than, for example, absorption, since absorption involves detecting a small change against a large background signal. Also, much work has already been done to amplify luminescence signals and improve efficiency, for example the luminescence of an indicator may be enhanced using metallic nano-particles which induces surface plasmon resonance, enhancing the luminescence signal and improving photostability [18].

- a wide range of analytes may be monitored via luminescence signals in the visible spectrum, whereas, for many analytes absorption occurs in

the UV or IR. As such, investigations into luminescence sensing may be easily implemented since a variety of low-cost excitation sources, such as LEDs, and detectors, such as photodiodes, are available for operation in the visible region.

- a wide range of luminescent indicator complexes are available, particularly for O_2, which is the analyte relevant to this work.

Despite the advantages of luminescence-based sensing, there are areas that require consideration when implementing this type of sensing:

- the issue of photobleaching plagues any sensor system using a luminophore [19]. This issue must be addressed or minimised according to the particular operating requirements of the sensor application
- while the sol-gel technique provides a relatively simple method to encapsulate luminophores, it is only a physical entrapment. Such immobilisation is susceptible to luminophore molecules leaching from the sol-gel-based material. This must be prevented to avoid both signal drift and sample contamination.
- signal drift due to excitation source drift is an issue with sensors operating in the intensity-domain. Theoretically, this may be minimised by operating in the frequency-domain, however in practice, great care must be taken to ensure that all intensity artifacts actually are eliminated.
- optoelectronic components are liable to drift with temperature, and so referencing is required. However, this issue is not exclusive to the optical sensor classes.
- the selection of indicator probes tends to be limited to those that are excited and emit in the visible spectrum. This limits the range of analytes it is possible to detect optically and limits the design possiblities. This is beginning to change as UV LEDs are being introduced.

1.2.2 O_2 sensing

O_2 is one of the most important and abundant chemical species. Comprising 20.9 % of the earth's atmosphere, it is essential for plant and animal life. Without a sufficient O_2 supply, a person will fall unconscious within seconds, and die within minutes. At the same time, prolonged exposure to high concentrations of O_2 can be harmful to one's health. As such, O_2 concentration is an important parameter to monitor and accordingly O_2 detection and analysis are used in a wide spectrum of applications ranging from science and medicine, to industrial processes.

Historically, Winkler titration is the most reliable and precise method to quantify O_2 [20]. This is a time consuming, classical technique that requires large sample volumes and is not suitable for continuous on-line monitoring [21].

The Clark-electrode has been the traditional means by which dissolved O_2 is measured over the last few decades. The Clark cell consist of a pair of electrodes separated from the sample by a semi-permeable membrane. This membrane permits the O_2 dissolved in the sample to pass through it to the electrodes, while preventing liquids and ionic salts from entering.

The cathode is a hydrogen electrode and carries a negative potential with respect to the anode. Electrolyte surrounds the electrode pair and is contained by the membrane. In the absence of O_2, the cathode becomes polarised with hydrogen and resists the flow of current. When O_2 passes through the membrane, the cathode is depolarised and electrons are consumed. The cathode electrochemically reduces the O_2 to hydroxyl ions:

$$O_2 + 2H_2O + 4e^- = 4OH^-$$

The anode reacts with the product of the depolarisation with a corresponding release of electrons.

$$Zn + 4OH^- = Zn(OH)_4^{2-} + 2e^-$$

The electrode pair permits current to flow in direct proportion to the amount of O_2 entering the system. The magnitude of the current gives us a

direct measure of the amount of O_2 entering the probe [22].

Optical sensing is deemed more appealing than either of these examples for reasons mentioned earlier, particulary, that O_2 is not consumed during sensing and that miniaturisation is a possibility.

Luminescence-based O_2 sensing is implemented in the literature by monitoring the luminescence-quenching of an indicator by O_2 molecules [23–28]. That is the technique employed in this work.

1.2.3 Luminescence-based O_2 sensor applications

Since O_2 is vital for life and an important parameter in many different interactions, the range of applications for O_2 detection is wide and varied. The advantages presented by the technique of luminescence-based sensing further extend the possible situations where O_2 sensing can be applied. A sample of these applications will be presented here.

Luminescence-based sensors developed for O_2-in-breath analysis provide non-invasive diagnostic information about a patient's state of health [29]. Luminescent O_2-sensitive labels, developed for food packaging, provide on-the-spot information regarding the integrity of the packaging seal. This presents a major advantage over random package testing which can only examine one package in an entire batch and requires destruction of that package [30]. In aerodynamic design applications, pressure-sensitive paints allow the entire surface of an aeroplane wing or automobile to be monitored, providing comprehensive pressure information. This provides an attractive alternative to traditional methods that only report on discrete areas [5]. Water-quality monitoring, which has applications in environmental monitoring and commercial fish farms, also requires O_2 monitoring for which luminescence-based sensing techniques provide for the possibility of remote sensing [31].

O_2 concentration can also be used as an indirect indicator of another process, of which O_2 is a product. For example Hashimoto et al. report an ethanol sensor that employs luminescence sensing to detect the O_2 consumption induced by an oxidation reaction of ethanol [32]. Wolfbeis et al. use the

same principle to determine lactate concentration by sensing the consumption of O_2 as lactate is oxidised [33]. Wolfbeis et al. have also implemented enzyme screening, through the luminescence-based detection of O_2 concentration [34].

Luminescence-based O_2 sensors can also provide a sensing solution in the bio-pharm industry. Monitoring the O_2 produced during the fermentation processes in bio-reactors is essential for quality control purposes but the humid environment and presence of ethanol can prove too harsh for electrical sensing techniques. Any in-built sensor element must also be capable of withstanding steam-sterilisation as re-calibration is not possible. This thesis will present such luminescence-based O_2 sensor elements, produced for the bio-pharm industry.

1.3 The sol-gel method and sol-gel materials

The sol-gel technique is a route to producing porous glasses at room temperature. In this work, sol-gels are produced via the formation of an interconnected 3-D network, through the simultaneous hydrolysis and polycondensation of an organosilicon precursor. This leads to the formation of a porous gel which, usually through a temperature programme, finally forms a hardened, porous, glassy material.

There is great flexibility in the production of a sol-gel glass, since the process requires that a liquid sol be produced initially, which then dries to form a gel and then a glass. For example, the liquid sol can be coated onto all manner of substrates and a variety of deposition techniques may be employed.

Additionally, particles of an indicator compound can be added to the liquid sol so that as the glass is formed, the molecules of the compounds are entrapped within it.

The main advantage of the sol-gel technique is the ability to modify the resulting glass by altering the processing parameters, such as heat treatment, pH and R-value [35]. Since changes in fabrication cause changes in the mi-

crostructure, the technique can be altered to produce the glass most suitable for the ultimate application. For example, elevating the drying temperature will increase the extent of evaporation of excess water and solvent molecules, thereby increasing the average pore size of the resulting material. This has a direct impact on the transport of O_2 through the glass implying that O_2 sensitivity can be tuned via heat treatment.

The versatility of the sol-gel technique is highlighted by the range of new materials discussed in this work and the range of sol-gel-based sensor elements reported in the literature for chemical sensing [12, 36, 37].

1.4 Industrial requirements and considerations

Fermentation refers to any of a group of chemical reactions that split complex organic compounds into relatively simple substances, most notably the anaerobic conversion of sugar to carbon dioxide and alcohol by yeast. Biofermentation is the process by which micro-organisms are grown in a suitable medium for the production of yogurt, cheese, alcoholic beverages and many other food products.

The development of micro-organisms is greatly influenced by their environment. O_2 is critical to their growth and, by extension, to the quality of the intended end-product. Traditionally, O_2 concentration during the fermentation process has been monitored using the Clark electrode. The Clark electrode presents some disadvantages, detailed in Section 1.2.2, in particular the consumption of O_2. The advent of luminescence-based sensing, with all its afore mentioned advantages, provides a non-invasive alternative solution.

In this project the sensor element is required to:

- detect O_2 in the range 0 - 100 %
- have a response of $\leq$ 5 s
- operate in the temperature range 4 - 40 °C

- operate in high humidity
- operate without the need for calibration after steam-sterilisation in an autoclave

1.5 Structure of thesis

This chapter prefaces the thesis with a review of: luminescence-based sensors; the sol-gel process and the relevance of O_2 sensing in bio-fermentation.

Chapter 2 reviews the theory of the sensing principles upon which the O_2 sensing in this work is based.

Chapter 3 introduces the sol-gel process, explaining the stages involved and the implications of its versatility.

Chapter 4 outlines the procedure by which the O_2-sensitive membranes are produced, including the deposition techniques used. This chapter also details each of the characterisation techniques used in this work. An account of phase fluorometry is presented, as this technique is used extensively in this work as a means of determining the O_2 sensitivity of the membranes. A section is also devoted to the principles of spectroscopic ellipsometery, explaining the principles of this technique, its precision and the interpretation of the data.

Chapter 5 introduces the various ORMOSIL-based sensor layers that are central to this work and characterises them according to O_2 sensitivity. The requirements of the applications, for which the materials in this work are ultimately intended, are outlined. The chapter then proceeds to show how these requirements have been met, by exploiting the versatile nature of the sol-gel process.

Chapter 6 presents the results of the phase fluorometry study. This chapter includes a discussion of the initial results and highlights the motivation behind the detailed study into the phase fluorometry technique which ultimately produced a laboratory-based system capable of returning accurate phase data.

Chapter 7 outlines the various attempts to obtain information on the porosity of the sensor membranes. In this chapter, the results from the ethanol interference study of Chapter 8 are given context. The dependence of membrane porosity on the starting precursor and processing parameters is presented and discussed.

Chapter 8 deals with the ethanol interference study. The study was initiated by a query from a commercial company interested in the effects of ethanol vapour on the O_2 sensitivity of sensor membranes. This chapter describes the approach undertaken in investigating this issue and discusses the results. The results in this chapter are linked to the study in Chapter 7.

Chapter 9 presents a review of the deposition techniques employed in this laboratory to produce sol-gel-based sensor layers.

Chapter 10 is the final chapter of this thesis and summarises the conclusions of this work.

1.6 Objectives of thesis

The ultimate goal of this thesis was the characterisation and optimisation of novel materials for luminescence-based O_2 sensing applications in the biopharm industry. This goal required several criteria be addressed, particularly:

- to optimise the O_2 sensitivity of sol-gel-derived sensor layers, through gaining an understanding of the origins of O_2 sensitivity in these materials.
- to produce O_2-sensitive materials capable of withstanding steam-sterilisation without requiring recalibration.
- to address the performance of the sensor layers in the presence of ethanol, since this is a likely interferant in a bio-fermenter.
- to address the issue of photobleaching.

- to execute O_2 sensing by a technique, such as phase fluorometry, which will lend itself to miniaturisation and the use of low-cost electronic components, since the sensor platform will be designed for a commercial application.

Overall, this work should emphasise the versatility of the sol-gel route, which has enabled the industrial requirements to be met. The work extends to a review of deposition techniques, suitable for producing discrete sensor elements from liquid sol. All areas are covered, from sol fabrication, deposition, characteristion and the implementation of the phase-domain sensing technique. This work provides a concise overview of the research program undertaken to achieve a satisfactory basis for a commercial sensing solution.

Bibliography

[1] Kerstin Purucker. Sensor technology: facts and forecasts. *Pictures of the Future, http://www.siemens.com*, 2004.

[2] Philips Research HomeLab. *http://www.research.philips.com/technologies*.

[3] K. Cammann, E.A.H. Hall, R. Kellner, H.L. Schmidt, and O.S. Wolfbeis. The Cambridge definition of chemcial sensors. 1995.

[4] A. Mills, C. Tommons, R.T. Bailey, M.C. Tedford, and P.J. Crilly. Luminescence temperature sensing using poly(vinylalcohol)-encapsulated $Ru(bpy)_3^{2+}$ films. *The Analyst*, 131:495–500, 2006.

[5] J. Handril, C. Davis, K. Mongey, C. McDonagh, and B.D. MacCraith. Temperature-corrected pressure-sensitive paint measurements using a single camera and a dual-lifetime approach. *Measurement Techniques*, 13:1552–1557, 2002.

[6] Chao-Xiang Shi. A novel pulsed fiber-optic rotation sensor with opto-electronic feedback. *Optics Communications*, 131:47–52, 1996.

[7] N. V. Kulagina, M. E. Lassman, F. S. Ligler, and C. Rowe Taitt. Antimicrobial peptides for detection of bacteria in biosensor assays. *Analytical Chemistry*, 77:6504–6508, 2005.

[8] K. Schult, A. Katerkamp, D. Trau, F. Grawe, K. Cammann, and M. Meusel. Disposable optical sensor chip for medical diagnostics: new ways in bioanalysis. *Analytical Chemistry*, 71:5430–5435, 1999.

[9] A. Mills and Q. Chang. Fluorescence plastic thin-film sensor for carbon dioxide. *Analyst*, 118:839–843, 1993.

[10] C. Malins, M. Niggemann, and B.D. MacCraith. Multi-analyte optical chemical sensor employing a plastic substrate. *Measurement Science and Technology*, 11:1105–1110, 2000.

[11] S.R. Johnson, J.M. Sutter, H.L. Engelhardt, P.C. Jurs, J. White, J.S. Kauer, T.A. Dickinson, and D.R. Walt. Identification of multiple analytes using an optical sensor array and pattern recognition neural networks. *Anal. Chem*, 69:4641–4648, 1997.

[12] O. Worsfold, C. Malins, M.G. Forkan, I.R. Peterson, B.D. MacCraith, and D.J. Walton. Optical NO sensing based on sol-gel entrapped azobenzene dyes. *Sensors and Actuators B*, 56(1521):1521, 1999.

[13] K.R. Kribich, R. Copperwhite, H. Barry, B. Kolodziejczyk, J.-M. Sabattie, K. O'Dwyer, and B.D. MacCraith. Novel chemical sensor/biosensor platform based on optical multimode interference (MMI) couplers. *Sensors and Actuators B*, 107:188–192, 2005.

[14] N. Mahendraa, P. Gangaiya, S. Sotheeswarana, and R. Narayanaswamy. Investigation of a fibre optic copper sensor based on immobilised α-benzoinoxime (cupron). *Sensors and Actuators B*, 90(1-3):118–123, 2003.

[15] C.S. Burke, L. Polerecky, and B.D. MacCraith. Design and fabrication of enhanced polymer waveguide platforms for absorption-based optical chemical sensors. *Measurement Science and Technology*, 15:11401145, 2004.

[16] T. Hirschfeld, T. Deaton, F. Milanovich, and S.M. Klainer. The feasibility of using fiber optics for monitoring groundwater contaminates. *Applied Optics*, 22(5):527–531, 1983.

[17] C. Malins, H.G. Glever, T.E. Keyes, J.G. Vos, W.J. Dressick, and B.D. MacCraith. Solgel immobilised ruthenium II polypyridyl complexes as

chemical transducers for optical pH sensing. *Sensors and Actuators B*, 67:89–95, 2000.

[18] O. Stranik, R. Nooney, C. McDonagh, and B.D. MacCraith. Plasmonic enhancement using core-shell nanoparticles. *Opto-Ireland 2005: Nanotechnology and Nanophotonics*, Proceedings of SPIE – Volume 5824, 2005.

[19] O. S. Wolfbeis. *Fiber optic chemical sensors and biosensors*. Boca Raton : CRC Press, 1991.

[20] D.A. Skoog, D.M. West, and F.J. Holler. *Fundamentals of analytical chemistry*. Fort Worth : Saunders College Pub, c1996, New York, 7th edition, 1996.

[21] J.R. Bacon and J.N. Demas. Determination of oxygen concentrations by luminescence quenching of a polymer-immobilized transition-metal complex. *Analytical Chemistry*, 59:2780–2785, 1987.

[22] L.C. Clark. Electrochemical device for chemical analysis, US patent 2913386, Nov. 7 1959.

[23] P.A.S. Jorge, P. Caldas, C.C. Rosa, A.G. Oliva, and J.L. Santos. Optical fiber probes for fluorescence based oxygen sensing. *Sensors and Actuators B*, 103:209–299, 2004.

[24] B.D. MacCraith, C.M. McDonagh, G. O'Keeffe, E.T. Keyes, J.G. Vos, B. O'Kelly, and J.F. McGlip. Fibre optic oxygen sensor based on fluorescence quenching of evanescent-wave excited ruthenium complexes in sol-gel derived porous coatings. *Analyst*, 118:385–388, 1993.

[25] S.B. Bambot, R. Holavanahali, and J.R. Lakowicz. Phase fluorometric sterilizable optical oxygen sensor. *Biotechnology and Bioengineering*, 43:1139–1145, 1994.

[26] M.E. Cox and B. Dunn. Detection of oxygen by fluorescence quenching. *Applied Optics*, 24(14):2114, 1985.

[27] R.A. Potyrailo and G.M. Hieftje. Oxygen detection by fluorescence quenching of tetraphenylporphyrin immobilized in the original cladding of an optical fiber. *Analytica Chimica Acta*, 370(1):1–8, 1998.

[28] W. Xu, K.A. Kneas, J.N. Demas, and B.A. DeGraff. Oxygen sensors based on luminescence quenching of metal complexes: osmium complexes suitable for laser diode excitation. *Analytical Chemistry*, 68:2605–2609, 1996.

[29] Y. Zhao, A. Richman, C. Storey, N. B. Radford, and P. Pantano. In situ fiber-optic oxygen consumption measurements from a working mouse heart. *Analytical Chemistry*, 71:3887–3893, 1999.

[30] C. von Bultzingslowen, A.K. McEvoy, C. McDonagh, B.D. MacCraith, I. Klimant, C. Krause, and O.S. Wolfbeis. Sol-gel based optical carbon dioxide sensor employing dual luminophore referencing for application in food packaging technology. *Analyst*, 127:1478–1483, 2002.

[31] A.K. McEvoy, C.M. McDonagh, and B.D. MacCraith. Dissolved oxygen sensor based on fluorescence quenching of oxygen-sensitive ruthenium complexes immobilized in sol-gel-derived porous silica coatings. *Analyst*, 121(6):785–788, 1996.

[32] K. Mitsubayashi, T. Kon, and Y. Hashimoto. Optical bio-sniffer for ethanol vapor using an oxygen-sensitive optical fiber. *Biosensors and Bioelectronics*, 19:193–198, 2003.

[33] W. Trettnak and O. S. Wolfbeis. A fiber optic lactate biosensor with an oxygen optrode as the transducer. *Analytical Letters*, 22(9):2191 – 2197, 1989.

[34] S. Arain, G.T. John, C. Krause, J. Gerlach, O.S. Wolfbeis, and I. Klimant. Characterisation of microtiterplates with intergrated optical sensors for oxygen and pH, and their applications to enzyme activity screening, respirometry, and toxicological assays. *Sensors and Actuators B*, 113:639 – 648, 2006.

[35] R. Gupta, S. Mozumdar, and N.K. Chaudhury. Effect of ethanol variation on the internal environment of sol-gel bulk and thin films with aging. *Biosensors and Bioelectronics*, 21:549–556, 2005.

[36] S. Ferretti, S-K Lee, B.D. MacCraith, A.G. Oliva, D.J. Richardson, D.A. Russell, , K.E. Sapsforda, and M. Vidalc. Optical biosensing of nitrite ions using cytochrome cd_1 nitrite reductase encapsulated in a solgel matrix. *Analyst*, 125:1993–1999, 2000.

[37] P.H. Kaye, J.E. Barton, E. Hirst, and J.M. Clark. Simultaneous light scattering and intrinsic fluorescence measurement for the classification of airbourne particles. *Applied Optics*, 39(21):3738–3745, 2000.

Chapter 2

Principles of O_2 Sensing by Luminescence Quenching

2.1 Introduction

This chapter outlines the theory behind the luminescence-based sensing techniques employed in this work. The definitions for fluorescence and phosphorescence processes and excited-state lifetime are given. The photochemistry of the transition metal ligand complex, Ru(II)-tris(4,7 diphenyl-1,10-phenanthroline) dichloride, $[Ru(dpp)_3]Cl_2$ [1], is discussed in terms of its relevance as a luminescent O_2 indicator. Luminescence quenching and the processes by which it occurs are explained. The principles governing luminescence sensing and how they are applied to O_2 quenching are also covered. This chapter also includes the theory of luminescence lifetime measurement techniques used in this work to determine the O_2 sensitivity of sensor membranes, including phase fluorometry.

[1] Denoted in the remainder of this document by the abbreviation, $[Ru(dpp)_3]^{2+}$

2.2 The luminescence process and luminescence lifetime

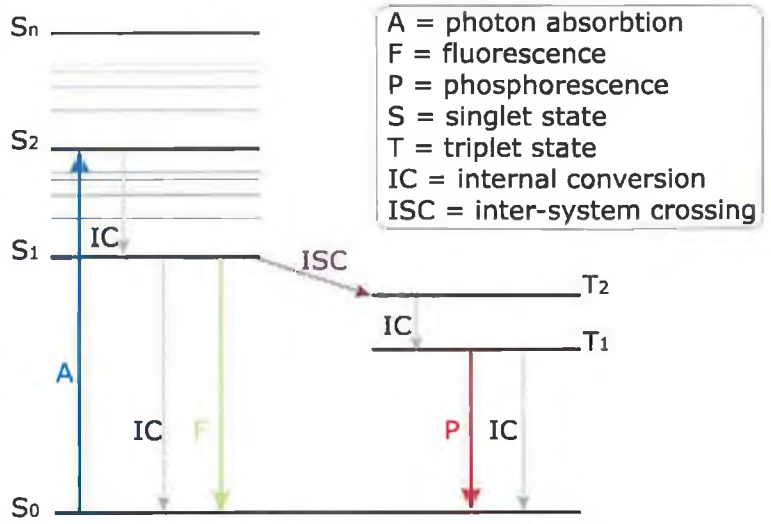

Figure 2.1: Simplified Jablonski energy level diagram illustrating fundamental excitation and emission processes

Luminescence is the emission of light from electronically excited states, where the external energy is not derived from the temperature of the emitting body. Of interest to this work is photoluminescence, where the external energy for the luminescence process is provided by light. Figure 2.1 is a simplified Jablonski diagram which schematically describes the processes associated with photoluminescence. In this figure, A denotes the absorption of a photon of light; IC denotes internal conversion, the transition of an electron between electronic states having similar electronic spin, such as between triplet states or between singlet states; and ISC denotes inter-system crossing, the transition of an electron between electronic states of differing electronic spin.

Photoluminescence is divided into two categories, fluorescence and phosphorescence, denoted in Figure 2.1 as F and P, respectively. These categories differ depending on the nature of the excited state.

Fluorescence refers to the process where an electron in an atom or molecule, having been excited from a ground state energy level, S_0, via an absorption process, to a singlet excited state, S_1, de-excites to ground state resulting in the emission of a photon. Emission rates are rapid, typically $10^8 s^{-1}$, and so fluorescence lifetimes are typically in the orders of nanoseconds [1].

Excited electrons may undergo a spin conversion from S_1 to the triplet excited state, T_1, by ISC. Phosphorescence refers to the emission of light from T_1 where the electron in the excited orbital has the same spin orientation as the ground-state electron. Here emission rates are slow, in the region of $10^3 - 10^0 s^{-1}$, so that phosphorescence lifetimes are typically milliseconds to seconds [1].

The distinction between fluorescence and phosphorescence is not always clear, for example transition-metal-ligand complexes (MLCs), which contain a metal and one or more organic ligands, display mixed singlet-triplet states [1, 2]. Such complexes are of interest to this work and so when referring to the emission of light from these complexes the general term luminescence will be used.

The average time interval that the electron spends in the excited state, prior to its return to ground state, is known as the luminescence lifetime, τ [1]. The observed lifetime, τ_{obs}, of a luminophore is given by Equation 2.1, where, Γ is the emissive rate of the luminophore and k_{nr} is the rate of non-radiative decay. The intrinsic lifetime of a luminophore refers to the time interval that the electron spends in the excited state, prior to its return to ground state, without any contribution from non-radiative processes.

$$\frac{1}{\tau_{obs}} = \frac{1}{\Gamma + k_{nr}} \tag{2.1}$$

In this work, O_2 concentration is measured as a function of the observed luminescence lifetime of a ruthenium complex while the complex undergoes collisional quenching by O_2. Collisional quenching will be explained in Section 2.4. The luminescence properties of ruthenium complexes are discussed in the next section.

2.3 Transition metal complexes and ruthenium complexes

Luminescent transition metal complexes (MLCs) represent a family of organometallic luminophores that have been widely used as indicator dyes, owing to features such as, strong visible absorption, efficient emissions and long-lived excited states [3, 4]. Examples of previous uses of luminescence-based sensors for O_2, CO_2, pH, temperature and several chemicals have been reported extensively [5–14]. In these examples, changes in the luminescence intensity or luminescence lifetime are monitored to indicate changes in analyte concentration [15].

The MLC of interest to this work, is the O_2-sensitive Ru(II)-tris(4,7 diphenyl-1,10-phenanthroline), $[Ru(dpp)_3]^{2+}$. This complex is widely accepted as an ideal choice for O_2 sensing, largely due to its emission at room temperature from a long-lived triplet metal-to-ligand-charge transfer state (^{3}MLCT). The rates of such emissions are slow since this is a partially forbidden transition and this gives rise to a relatively long excited-state lifetime [2]. This extended lifetime contributes to increased sensitivity according to the Stern-Volmer equation (this will be discussed later in Section 2.4). The long excited-state lifetime also allows lifetime-based sensing to be performed using inexpensive detection devices such as photodiodes [16, 17].

While the long excited-state lifetime is clearly an attractive feature, $[Ru(dpp)_3]^{2+}$ possesses additional characteristics relevant to O_2 sensing applications. These include: chemical stability, arising from the covalent nature of the metal-ligand bonds; photostability; solubility in typical sol-gel precursors [18]; broad absorption band due to MLCT; and large Stoke's shift with an excitation centered at 450 nm and emission maximum of ca. 610 nm. This significant Stoke's shift allows separation of the absorption and emission peaks and also reduces the likelihood of reabsorption or self-quenching [1]. Such a Stoke's shift simplifies design considerations for sensor platforms and allows for the use of relatively low-cost filters.

The broad absorption band in the blue region of the spectrum can be

seen in Figure 2.2. In this figure, the emission profile of a standard blue LED (blue line) is superimposed on the absorption spectrum of $[Ru(dpp)_3]^{2+}$ (black line). This illustrates the suitability of readily available, relatively low-cost LEDs as excitation sources for sensor platforms employing the $[Ru(dpp)_3]^{2+}$ complex.

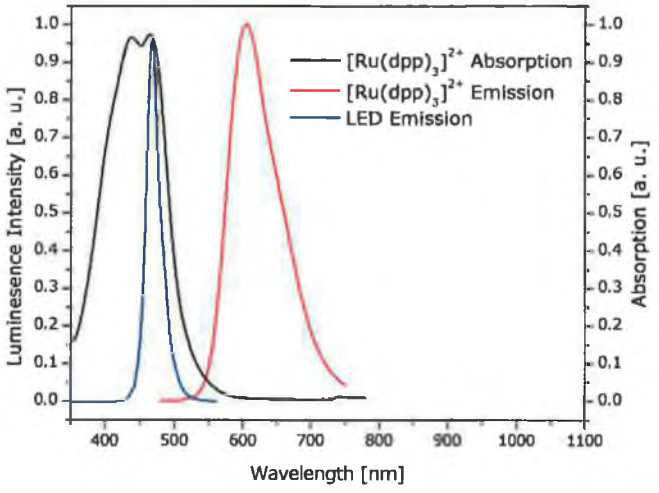

Figure 2.2: Absorption spectrum of $[Ru(dpp)_3]^{2+}$, emission spectrum of $[Ru(dpp)_3]^{2+}$ and emission profile of LED. Absorbtion spectrum acquired using a UV-Vis spectrometer (Varian, Cary 50 Scan). Emission spectra recorded with a fluorometer (Jobin Yvon, Spex FluoroMax 2).

A further interesting feature of $[Ru(dpp)_3]^{2+}$ is that its structure, shown in Figure 2.3, ensures the complex is shielded from external environmental effects. Previous work in this laboratory has found that this shielding effect is due to the phenyl groups and reduces the possibility of interference with the O_2-sensitive signal [19, 20]. Other authors have also reported on this effect [21, 22].

These features, in addition to the thermal, chemical and photochemical stability that the $[Ru(dpp)_3]^{2+}$ complex exhibits, make this an ideal choice of luminophore for use in a durable and robust O_2 sensor platform.

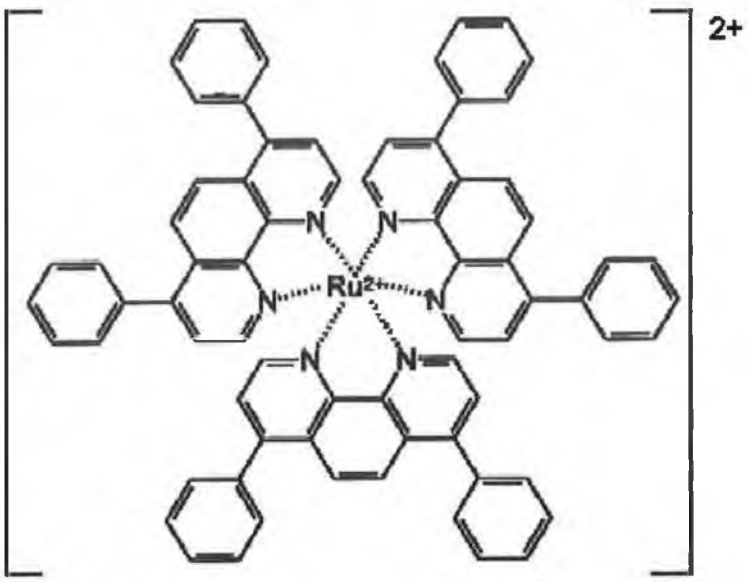

Figure 2.3: Structure diagram of $[Ru(dpp)_3]^{2+}$

2.4 Luminescence quenching and the Stern-Volmer equation

The term, non-radiative decay, refers to any process by which an excited electron is returned to ground state without the emission of a photon. The subsequent decrease in luminescence caused by non-radiative decay is referred to as luminescence quenching [1].

Luminescence quenching can occur by several means. Two of these process, collisional quenching and complex formation, are detailed here.

2.4.1 Dynamic Quenching

Dynamic, or collisional, quenching requires molecular contact between luminophore and quencher, in this case $[Ru(dpp)_3]^{2+}$ and O_2, respectively. The quencher must diffuse to the luminophore during the excited state lifetime of the luminophore. O_2 has been widely reported as a strong collisional

quencher [23]. When the O_2, represented as the quencher, Q, in Figure 2.4, interacts with the luminophore, $[Ru(dpp)_3]^{2+}$, the luminophore returns to the ground state without the emission of a photon. This occurs via the formation of an excited charge-transfer complex referred to as an exciplex. This is known as collisional, or dynamic, quenching.

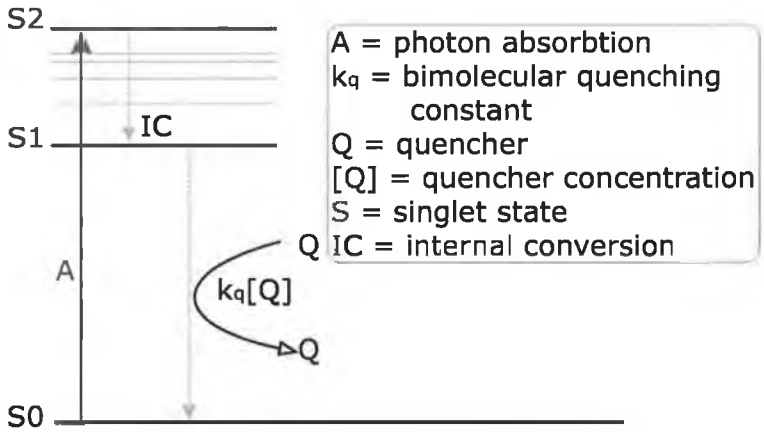

Figure 2.4: Simplified Jablokski diagram illustrating dynamic quenching

As dynamic quenching is a non-radiative process, it contributes to the non-radiative decay rate, k_{nr}, in Equation 2.1. From Equation 2.1, it can be seen that a change in k_{nr} yields a change in the observed lifetime, τ_{obs} , and therefore, a corresponding change in luminescence intensity. Since the extent of dynamic quenching is proportional to the quantity of O_2 present, this can be exploited as a sensing mechanism.

Collisional quenching is described by the Stern-Volmer equation which is given in its generalised form in Equation 2.2 [1]:

$$\frac{I_0}{I} = \frac{\tau_0}{\tau} = [1 + 4\pi gRND[Q]\tau_0/1000][SQ/TQ] \tag{2.2}$$

where I_0 or τ_0, are the luminescence intensity, or lifetime, in the absence of quencher; I or τ, is the intensity, or lifetime, at any quencher concentration ([Q] in units of molarity); g is the spin statistical factor reflecting the state type being quenched; R is the luminophore-quencher interaction

distance (in cm); N is Avogadro's number; D is the quencher diffusion coefficient (in cm ^{2}s^{-1}). The factor of 1000 is required to convert molarity units to molecules/cm^3. SQ and TQ represent static quenching and transient quenching, respectively.

Considering O_2 as the quencher at room-temperature, the term Q can be replaced in terms of pO_2 as follows [24]:

$$[Q] = [O_2] = (0.041)(S)(pO_2) \tag{2.3}$$

where the term 0.041 originates from the O_2 Henry's law constant [24], S is the O_2 solubility constant within the host matrix (in units of molL^{-1}atm^{-1}), and pO_2 is the O_2 partial pressure (in atm).

Assuming $[Ru(dpp)_3]^{2+}$ emits from a triplet state, this gives a value for g of 1/9, R may be assigned a value of 1×10^{-7} cm. The product of $D \times S$ is P, the host matrix permeability to O_2, and under quenching conditions SQ and TQ are essentially unity [24]. Allowing for all of these conditions, Equation 2.2 may be recast as:

$$\frac{I_0}{I} = \frac{\tau_0}{\tau} = 1 + (3.4 \times 10^{12}) P \tau_0 [pO_2] = 1 + K_{SV}[O_2] \tag{2.4}$$

therefore,

$$K_{SV} = (3.4 \times 10^{12}) P \tau_0 \tag{2.5}$$

where, K_{SV} is the Stern-Volmer constant. In O_2 sensing, K_{SV} represents the sensor sensitivity and from Equation 2.5, is dependent on P and τ_0.

τ_0 is an intrinsic property of the luminophore but it can also be influenced by the immediate environment of the luminophore. For example, the lifetime of $[Ru(dpp)_3]^{2+}$ in solution is shorter than that of the same molecule immobilised in a solid matrix. P is proportional to the O_2 diffusion coefficient, D, of the matrix in which the luminophore is immobilised. Therefore, for optimum sensor design, K_{SV} can be tuned by selecting a luminophore and immobilisation matrix with the optimum τ and P values [24, 25].

For homogeneous environments, according to the ideal case described by

Equation 2.4, a plot of I_0/I or τ_0/τ versus $[O_2]$ will be linear, with a slope equal to K_{SV} and an intercept of unity. If a more complex system is considered, the Stern-Volmer plot deviates from linearity. This is the case for a luminophore population immobilised in an amorphous matrix, as for the sensor platforms described in this work. This behaviour is associated with the distribution of the luminophore population in the glassy matrix, where the embedded luminescent species encounters different environmental influences. The host microheterogeneity causes luminophore populations in different sites to experience different quenching rates with a resultant downward curve in the Stern-Volmer plot [26].

Various models have been developed to describe quenching data that deviate from the Stern-Volmer model [27, 28] . For the sensor systems in this work, the Demas model, described by Equation 2.6, is employed, in addition to the Stern-Volmer model, to analyse the O_2 quenching data. These models have been chosen on account of their simplicity but also to facilitate comparison with current work in other laboratories, as these models are commonly used among other authors in this field [29–31].

$$\frac{I_0}{I} = \frac{\tau_0}{\tau} = \left[\frac{f_1}{1 + K_{SV1}[O_2]} + \frac{f_2}{1 + K_{SV2}[O_2]}\right]^{-1} \tag{2.6}$$

In Equation 2.6, f_i represents the fractional contribution of the total emission from the luminophore located at site i, under unquenched conditions that exhibits a discrete Stern-Volmer quenching constant, given by K_{SVi}.

Determining O_2 concentration by monitoring the luminescent properties of the O_2-quenchable excited-state of $[Ru(dpp)_3]^{2+}$ is the sensing mechanism at the core of this work. The principles behind the most popular techniques for monitoring the changes in luminescence lifetime or intensity are discussed the following section.

2.4.2 Static Quenching

Static quenching refers to the combination of a quencher molecule with an excited luminophore molecule, to form a non-luminescent complex. This non-luminescent complex returns to the ground state without the emission of a photon [32].

Since the luminophore molecule is no longer in the excited state the observed luminescence intensity is decreased [33]. Static quenching is proportional to quencher concentration, as governed by Equation 2.7.

$$\frac{I_0}{I} = 1 + K_S[Q] \tag{2.7}$$

where,

$$K_S = \frac{[L-Q]}{[L][Q]} \tag{2.8}$$

In Equations 2.7 and 2.8, I_0 and I refer to the luminescence intensity in the absence and presence of quencher; K_S is the static quenching constant; L denotes the uncomplexed luminophore population and Q is the uncomplexed quencher population.

From Equations 2.4 and 2.7, it is apparent that observation of intensity measurements alone does not provide information as to whether the quenching process is static or dynamic. Additional techniques must be applied to distinguish the quenching process. For example, at increased temperature, diffusion coefficients are found to increase, hence the Stern-Volmer constant will increase in the case of dynamic quenching. Conversely, in the case of static quenching the Stern-Volmer constant is found to decrease with increasing temperature, since the increased temperature causes the complexes to become unstable.

Excited-state lifetime measurement is the definitive technique to distinguish static from dynamic quenching. Since the process of complex formation reduces the luminophore population, it follows that the luminescence inten-

sity will be reduced. However, the excited-state lifetime is not disturbed and so static quenching is not detected by direct lifetime measurements. As such, for static quenching $\tau_0/\tau = 1$ whereas, for dynamic quenching $\tau_0/\tau = I_0/I$, as detailed in the previous section.

Static quenching is not observed for the systems central to this work as will be discussed in Chapter 6.

2.5 Luminescence lifetime measurement techniques

Luminescence-based O_2 sensors have been extensively researched in recent years, due to the importance of O_2 concentration determination in industrial, environmental and biomedical applications [34–36]. These optical O_2 sensors present an alternative to traditional O_2 detectors, such as the Clark electrode, as they do not suffer from electrical interference, O_2 consumption or the other issues suffered by electrochemical sensors [37, 38]. In addition, luminescence-based O_2 sensors provide versatility in sensor design, by combining the intrinsic sensitivity and selectivity of the luminescence process with the wide availability of optoelectronic components, thereby allowing a range of various sensor configurations.

Luminescence-based O_2 sensors are based on luminescence quenching by O_2, of either the intensity or excited-state lifetime of the luminophore. Lifetime-based detection is preferred, providing reliable measurements by remaining insensitive to factors such as excitation source drift. Lifetime-based detection can be achieved in both the time- and frequency-domain [39]. This section highlights the principles underlying the determination of the excited-state lifetime in each domain.

2.5.1 Time-domain measurements

The time-domain approach employed here is one of impulse response, where the sample emission following pulsed excitation, from a low repetition rate laser, is recorded using a high speed detection system, such as a photomultiplier tube (PMT) and a digital oscilloscope. Excited-state lifetimes can then be determined by analysing time-dependent decays of luminescence intensity. [40]

When a luminophore is excited by a short pulse of light, the excited-state decays as it is depleted of excited luminophores. Equation 2.9 describes this process as an exponential decay law:

$$I(t) = I_0 e^{-t/\tau} \tag{2.9}$$

where, I_0 is the luminescence intensity at the time excitation is terminated and τ is the excited-state luminescence lifetime. In many cases, the intensity decay is not accurately described by a single exponential decay law. In these situations, the observed intensity decay is often given by a sum of exponentials:

$$I(t) = \sum_{i=1}^{n} \alpha_i e^{-t/\tau} \tag{2.10}$$

where, α_i is the pre-exponential factor denoting the contribution to the total time-resolved decay of the component with lifetime τ_i.

The excited state lifetime is then recovered by curve fitting the collected intensity decay trace [41]. Instrumentation details are described in Chapter 5.

2.5.2 Frequency-domain measurements

Intensity measurements of the luminophore's emission at known O_2 concentrations can be used to characterise O_2-sensitive membranes. However, life-

time measurements are preferred as they will not be influenced by external variations such as detector drift or changes in sample alignment [42]. Unfortunately, directly measuring the lifetime of a luminophore requires sophisticated light sources, costly detectors and involves considerable data analysis, as outlined in the section above. Phase fluorometry offers a cheaper and less complex alternative to direct lifetime measurements for O_2 sensing [43].

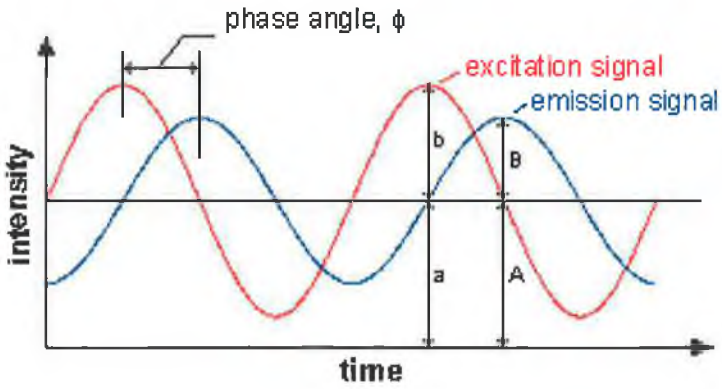

Figure 2.5: Illustration of phase measurements

When a luminophore is excited by a sinusoidally modulated light signal, its resulting emission is modulated at the same frequency but phase shifted relative to the excitation signal [44]. The phase angle, ϕ, in Figure 2.5, refers to the phase lag between the modulated excitation signal (red line) and the emitted luminescence (blue line). The phase angle can be used to calculate the lifetime from Equation 2.11, where ω represents the angular frequency of the luminescence ($\omega = 2\pi f$).

$$\tan \phi = \omega\tau \tag{2.11}$$

For a given error in ϕ, maximum lifetime measurement accuracy can be obtained using the optimum modulation frequency. The optimum frequency f_{opt} may be defined, from Equation 2.11, as that frequency for which the following expression is satisfied:

$$2\pi f_{opt}\tau = 1 \tag{2.12}$$

that is, the frequency for which $\phi = 45°$ [8].

Lifetime can also be determined by measuring the demodulation factor. From Equation 2.13, the demodulation factor m is given by the ratio of the modulation of the emission signal to the modulation of the excitation signal. In Equation 2.13, a is the average intensity of the incident light, b is the modulated amplitude of the incident light, A is the average intensity of the emission and B is the modulated amplitude of the emission. Figure 2.5 shows a, b, A and B. Equation 2.14 relates the demodulation factor to the lifetime [45].

$$m = \frac{B/A}{b/a} \tag{2.13}$$

$$m = [1 + \omega^2\tau_m^2]^{-\frac{1}{2}} \tag{2.14}$$

2.6 Conclusions

This chapter has defined luminescence in terms of fluorescence and phosphorescence. The excited-state lifetime has also been defined. The principles of luminescence quenching are explained and the manner in which luminescence quenching is exploited as the sensing mechanism at the core of this work has been outlined. The theory underlying techniques using both time- and frequency-domain measurements to monitor luminescence as a function of analyte concentration, have been presented. The implementation of these techniques will be detailed in Chapter 4. Frequency-domain, as opposed to time- or intensity-domain, measurement has been highlighted as the optimum detection technique for this work.

Bibliography

[1] J. R. Lakowicz. *Principles of fluorescence spectroscopy*. Kluwer Academic/ Plenum Publishers, New York, 2nd edition, 1999.

[2] E. R. Carraway, J. N. Demas, B. A. DeGraff, and J. R. Bacon. Photophysics and photochemistry of oxygen sensors based on luminescent transition-metal complexes. *Analytical Chemistry*, 63:337–342, 1991.

[3] J. N. Demas and B. A. DeGraff. Applications of luminescent transition metal complexes to sensor technology and molecular probes. *Journal of Chemical Education*, 74(6):690–695, 1997.

[4] J. N. Demas and B. A. DeGraff. Design and applications of highly luminescent transition metal complexes. *Analytical Chemistry*, 63(17):829A, 1991.

[5] K. P. McNamara, X. Li, A. D. Stull, and Z. Rosenzweig. Fiber-optic oxygen sensor based on the fluorescence quenching of tris (5-acrylamido, 1, 10 phenanthroline) ruthenium chloride. *Analytica Chimica Acta*, 361:73–83, 1998.

[6] B. D. MacCraith, C. M. McDonagh, G. O'Keeffe, A. K. McEvoy, T. Butler, and F. R. Sheridan. Sol-gel coatings for optical chemical sensors and biosensors. *Sensors and Actuators B*, 29:51–57, 1995.

[7] R. A. Potyrailo and G. M. Hieftje. Oxygen detection by fluorescence quenching of tetraphenylporphyrin immobilized in the original cladding of an optical fiber. *Analytica Chimica Acta*, 370(1):1–8, 1998.

[8] S. B. Bambot, R. Holavanahali, and J. R. Lakowicz. Phase fluorometric sterilizable optical oxygen sensor. *Biotechnology and Bioengineering*, 43:1139–1145, 1994.

[9] W. XU, R. Schmidt, M. Whaley, J. N. Demas, B. A. DeGraff, E. K. Karikari, and B. L. Fanner. Oxygen sensors based on luminescence quenching: interactions of pyrene with the polymer supports. *Analytical Chemistry*, 67:3172–3180, 1995.

[10] C. Malins, M. Niggemann, and B. D. MacCraith. Multi-analyte optical chemical sensor employing a plastic substrate. *Measurement Science and Technology*, 11:1105–1110, 2000.

[11] B. Higgins and B.A. DeGraff. Luminescent transition metal complexes as sensors: structural effects on pH response. *Inorganic Chemistry*, 2005.

[12] C. Malins, H.G. Glever, T.E. Keyes, J.G. Vos, W.J. Dressick, and B.D. MacCraith. Solgel immobilised ruthenium II polypyridyl complexes as chemical transducers for optical pH sensing. *Sensors and Actuators B*, 67:89–95, 2000.

[13] O. Worsfold, C. Malins, M.G. Forkan, I.R. Peterson, B.D. MacCraith, and D.J. Walton. Optical NO sensing based on sol-gel entrapped azobenzene dyes. *Sensors and Actuators B*, 56(1521):1521, 1999.

[14] O. S. Wolfbeis, I. Klimant, T. Werner, C. Huber, U. Kosch, C. Krause, G. Neurauter, and A. Durkop. Set of luminescence decay time based chemical sensors for clinical applications. *Sensors and Actuators B*, 51:17–24, 1998.

[15] Andrew Mills. Controlling the sensitivity of optical oxygen sensors. *Sensors and Actuators B*, 51:60–68, 1998.

[16] C. S. Burke, A. Markey, R. I. Nooney, P. Byrne, and C. McDonagh. Development of an optical sensor probe for the detection of dissolved carbon dioxide. *Sensors and Actuators B*, 119:288–294, 2006.

[17] A. K. McEvoy, C. M. McDonagh, and B. D. MacCraith. Dissolved oxygen sensor based on fluorescence quenching of oxygen-sensitive ruthenium complexes immobilized in sol-gel-derived porous silica coatings. *Analyst*, 121(6):785–788, 1996.

[18] G. A. Baker, B. R. Wenner, A. N. Watkins, and F. V. Bright. Effects of processing temperature on the oxygen quenching behavior of tris(4,70-diphenyl-1,100-phenanthroline) ruthenium (II) sequestered within sol-gel-derived xerogel films. *Journal of Sol-Gel Science and Technology*, 17:71–82, 2000.

[19] K. Mongey, J.G. Vos, B.D. MacCraith, and C.M. McDonagh. The photophysical properties of ruthenium polypyridyl complexes within a sol-gel matrix. *Journal of Sol-Gel Science and Technology*, 8:979–983, 1997.

[20] K. F. Mongey, J. G. Vos, B. D. MacCraith, C. M. McDonagh, C. Coates, and J. J. McGarvey. Photophysics of mixed-ligand polypyridyl ruthenium(II) complexes immobilised in silica sol-gel monoliths. *Journal of Materials Chemistry*, 7(8):1473–1479, 1997.

[21] E. R. Carraway and J. N. Demas. Photophysics and oxygen quenching of transition-metal complexes on fumed silica. *Langmuir*, 7:2991–2998, 1991.

[22] J. R. Bacon and J. N. Demas. Determination of oxygen concentrations by luminescence quenching of a polymer-immobilized transition-metal complex. *Analytical Chemistry*, 59:2780–2785, 1987.

[23] A. Mills, C. Tommons, R. T. Bailey, M. C. Tedford, and P. J. Crilly. Luminescence temperature sensing using poly(vinylalcohol)-encapsulated $Ru(bpy)_3^{2+}$ films. *The Analyst*, 131:495–500, 2006.

[24] H.Liu, S. C. Switalski, B. K. Coltrain, and P. B. Merkel. Oxygen permeability of sol-gel coatings. *Applied spectroscopy*, 46(8):1266, 1992.

[25] A. Mills and F. C. Williams. Chemical influences on the luminescence of ruthenium diimine complexes and its response to oxygen. *Thin Solid Films*, 306:163–170, 1997.

[26] I. Klimant and O. Wolfbeis. Oxygen-sensitive luminescent materials based on silicone-soluble ruthenium diimine complexes. *Analytical Chemistry*, 67:3160–3166, 1995.

[27] W. XU, R. C. McDonough, B. Langsdorf, J. N. Demas, and B. A. DeGraff. Oxygen sensors based on luminescence quenching: interactions of metal complexes with polymer supports. *Analytical Chemistry*, 66:4133–4141, 1994.

[28] A. Mills. Optical sensors for oxygen: a log-gaussian multisite-quenching model. *Sensors and Actuators B*, 51:69–76, 1998.

[29] E. J. Cho and F. V. Bright. Pin-printed chemical sensor arrays for simultaneous multianalyte quantification. *Analytical Chemistry*, 74:1462–1466, 2002.

[30] P. Roche, R. Al-Jowder, R. Narayanaswamy, J. Young, and P. Scully. A novel luminescent lifetime-based optrode for the detection of gaseous and dissolved oxygen utilising a mixed ormosil matrix containing ruthenium (4,7-diphenyl-1, 10-phenanthroline)$_3$Cl$_2$. *Analytical and Bioanalytical Chemistry*, 386:1245–1257, 2006.

[31] P.A.S. Jorge, P. Caldas, C.C. Rosa, A.G. Oliva, and J.L. Santos. Optical fiber probes for fluorescence based oxygen sensing. *Sensors and Actuators B*, 103:209–299, 2004.

[32] O.S. Wolfbeis. *Fluorescence spectroscopy : new methods and applications*. Springer-Verlag, New York, 1993.

[33] J. Wang, D. Wang, E. K. Miller, D. Moses, and A. J. Heeger. Static and dynamic photoluminescence (PL) quenching of polymer:quencher systems in solutions. *Synthetic Metals*, 119:591–592, 2001.

[34] M. Fitzgerald, D.B. Papkovsky, M. Smiddy, J.P. Kerry, C.K. O' Sullivan, D.J. Buckley, and G.G. Guilbault. Nondestructive monitoring of oxygen profiles in packaged foods using phase-fluorimetric oxygen sensor. *Journal of Food Science*, 66(1):105, 2001.

[35] E. Vander Donckt, B. Camerman, R. Herne, and R. Vandeloise. Fibre-optic oxygen sensor based on luminescence quenching of a Pt(II) complex embedded in polymer matrices. *Sensors and Actuators B*, 32:121–127, 1996.

[36] G. A. Holst, T. Koster, E. Voges, and D. W. Lubbers. Flox an oxygen-flux-measuring system using a phase-modulation method to evaluate the oxygen-dependent fluorescence lifetime. *Sensors and Actuators B*, 29(1-3):231–239, 1995.

[37] J. Ji, N. Rosenzweig, I. Jones, and Z. Rosenzweig. Novel fluorescent oxygen indicator for intracellular oxygen measurements. *Journal of Biomedical Optics*, 7(3):404–409, 2002.

[38] Y. Amao, T. Miyashita, and I. Okura. Novel optical oxygen sensing material: platinum octaethylporphyrin immobilized in a copolymer film of isobutyl methacrylate and tetrafluoropropyl methacrylate. *Reactive and Functional Polymers*, 47:49–54, 2001.

[39] I. M. Warner, G. Patonay, and M. P. Thomas. Multidimensional luminescence measurements. *Analytical Chemistry*, 57(3):463A – 483A, 1985.

[40] F. V. Bright and C. A. Munson. Time-resolved fluorescence spectroscopy for illuminating complex systems. *Analytica Chimica Acta*, (500):71–104, 2003.

[41] J. N. Demas. *Excited state lifetime measurements*. Academic Press, London, 1983.

[42] C. McDonagh, C. Kolle, A.K. McEvoy, D.L. Dowling, A.A. Cafolla, S.J. Cullen, and B.D. MacCraith. Phase fluorometric dissolved oxygen sensor. *Sensors and Actuators B*, 74:124–130, 2001.

[43] G. O'Keeffe, B. D. MacCraith, A. K. McEvoy, C. M. McDonagh, and J. F. McGilp. Development of a led-based phase fluorimetric oxygen sensor using evanescent wave excitation of a sol-gel immobilized dye. *Sensors and Actuators B*, 29:226–230, 1995.

[44] Q. Chang, J. R. Lakowicz, and G. Rao. Fluorescence lifetime-based sensing of methanol. *Analyst,*, 122:173–177, 1997.

[45] D. Andrzejewski, I. Klimant, and H. Podbielska. Method for lifetime-based chemical sensing using the demodulation of the luminescence signal. *Sensors and Actuators B*, 84:160–166, 2002.

Chapter 3

The Sol-Gel Process

3.1 Introduction

As far back as the 1840s, it was observed that the hydrolysis and condensation of the silicon alkoxide, tetraethoxysilane (TEOS), produces silica gel [1]. However, significant interest in the sol-gel process only really began in the 1970s, when the process was exploited as a route to producing porous glasses at low temperatures [2]. The process affords the possibility of tuning the resulting glasses by varying the process parameters [3]. Before the densified glass is formed, a liquid sol state is reached, which lends itself to moulding or coating onto a range of substrates.

This chapter describes how the tunability of the process has been employed in this work to produce materials suitable for use as sensor membranes. The versatility of the sol state allows the formation of thin films via deposition techniques such as dip-coating, which will be described in Section 3.7.

3.2 Sol-gel processing

Before delving into the various processing parameters and applications of the sol-gel techniques, it is useful to define the relevant terms. The term

sol, refers to a colloidal suspension of small particles (1-1000 nm) in a liquid medium. A **gel** is formed when attractive forces in the sol cause the particles in a sol to interconnect to form a network. Therefore, a gel is a substance containing a continuous solid skeleton which contains a continuous liquid phase. A dried gel is known as a **xerogel**. A **precursor** in the sol-gel process, consists of a metal element surrounded by ligands [4]. In this work silicon alkoxide precursors are used.

A sol-gel material is formulated by combining a precursor with water, a catalyst and a co-solvent. The subsequent hydrolysis and polycondensation of the precursor, results in the formation of a sol. This sol may be used to coat the required substrate. The coated layer undergoes a densification process during a drying period, becoming a gel, leading to the formation of a xerogel. The xerogel formation can be hastened by applying a temperature program during the drying period [5]. The process is illustrated in Figure 3.1.

The process parameters and relative quantities of precursor, water, catalyst and the choice of solvent used in this work, have been selected in order to produce low density xerogels, exhibiting a level of porosity suitable for sensing applications [6–9].

The various stages of the sol-gel process will be introduced in this chapter. Since some questions still remain regarding the exact mechanisms of these processes and the influence of endless processing parameters on the properties of the resulting xerogel [2,3,10], only an overview will be given here, focusing on those parameters manipulated to produce xerogel characteristics relevant to this work.

A more complete understanding of the complex interactions of the sol-gel process is available in the literature [3,4,11,12].

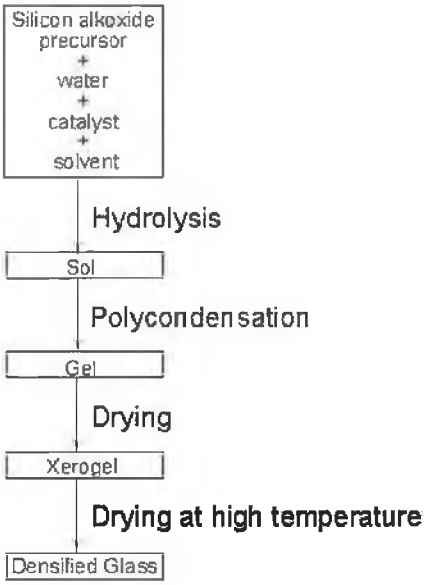

Figure 3.1: The sol-gel process

3.3 Hydrolysis and condensation

The reaction of metal alkoxides with water is known as **hydrolysis**. In the reaction, a hydroxyl ion becomes attached to the metal atom, according to the following reaction:

$$\equiv Si - OR + H_2O \quad \rightleftharpoons \quad \equiv Si - OH + ROH. \tag{3.1}$$

where, R is an alkyl group, C_xH_{2x+1} and ROH is an alcohol.

In a **condensation** reaction, two partially hydrolysed molecules link together, with the release of a small molecule, such as water or alcohol, as in the following two reactions:

Alcohol condensation:

$$\equiv Si - OR + HO - Si \equiv \quad \rightleftharpoons \quad \equiv Si - O - Si \equiv + ROH. \tag{3.2}$$

Water condensation:

$$\equiv Si - OH + HO - Si \equiv \quad \rightleftharpoons \quad \equiv Si - O - Si \equiv + H_2O. \tag{3.3}$$

The hydrolysis and polycondensation of the precursor is initiated with the addition of water to the alkoxysilanes. A mutual solvent is required to aid miscibility. A catalyst, either acid or base, controls the rate of the hydrolysis and polycondensation thereby influencing the structure of the condensed material. The influence of the catalyst conforms to the general rule that acid-catalysed reactions lead to less highly branched products than based-catalysed [4].

The hydrolysis and polycondensation reactions continue, building up chains of $\equiv Si - O - Si \equiv$ molecules, which become interconnected, increasing the viscosity of the solution, to form the more rigid porous network of the gel.

While it is accepted that hydrolysis and polycondensation play an important part in developing the structural properties of the resulting glass, it is difficult to separate these two processes [13]. That is, the condensation reaction, be it Equation 3.2 or 3.3, begins while hydrolysis is taking place. Essentially, hydrolysis controls the condensation rate, since hydrolysis provides the starting material for the condensation reactions, as can be seen from Equation 3.1.

Hydrolysis and condensation are controlled by numerous parameters, such as, catalyst type as mentioned above, and water content. By controlling these process parameters, to adjust the rate of hydrolysis and subsequently condensation, it is possible to control properties such as porosity and homogeneity. In this way, xerogels may be produced with the characteristics required for a desired application.

Those processing parameters of relevance to this work will be discussed in the following section.

3.4 Factors affecting the sol-gel process

3.4.1 Influence of water:precursor ratio (R-value)

The R-value is the molar ratio of water to precursor. It has been found R-value controls the rate of hydrolysis with a subsequent impact on the resulting xerogel microstructure. For example, at low pH values, sols prepared with increasing R-value, exhibit increased density and a smaller average pore size. [14].

In this work, we require xerogels of sufficient porosity to allow for O_2 diffusion into the matrix, while retaining a level of cross-linking sufficient to prevent leaching of entrapped luminophore molecules. Therefore, intermediate R-values of 3 or 4 are used, with an acid catalyst, to yield sols suited to producing materials of the relevant density [15].

3.4.2 Influence of sol aging and drying

In addition to hydrolysis and condensation, the conditions concerning the aging of the sol and drying of the deposited film, also contribute to the structural properties of the final material.

Aging refers to the process of change in structure and properties that takes place due to the bond formations that continue to occur between particles, as a sol-gel is forming. [4].

Aging takes place after the initial mixing step. The liquid sol to be aged, is left to stand for a period of time to allow hydrolysis and polycondensation to continue. A heat treatment may be applied to accelerate the process.

Prolonging the period of hydrolysis and polycondensation increases the degree of cross-linking and has the effect of increasing the viscosity of the

sol. The viscosity of the sol is of particular relevance for thin film formation, where a certain minimum viscosity must be obtained in order to allow coating of substrates [16].

Following deposition, **drying** refers to the process during which the remaining liquid and solvent is expelled from the skeletal structure, resulting in the formation of a xerogel.

During drying, xerogels can crack, loose porosity and become dense, so process parameters must be controlled to ensure desirable properties are retained after drying.

3.5 ORMOSILs

Organically modified silicates (ORMOSILs), are materials composed of a mixture of inorganic and organic components [17]. Countless materials fall into this classification since there are endless possibilities available by combining inorganic network formers, or modifiers, with organic network formers, or modifiers [18].

Schmidt declares organically modified glasses to exhibit characteristics such as, high transparency, hardness and amorphous structure usually attributed to inorganic glasses [19]. Additionally, each organosilicon precursor impacts on the hydrolysis rate and subsequently affects the xerogel formation, thereby varying some structural properties and chemical behaviour of these glasses [20, 21]. In this way, ORMOSIL glasses have all the aforementioned attributes of inorganic glasses, while selected characteristics may be altered through considered choice of organic component.

Organosilicon precursors contain a non-hyrolysable Si-C bond, $R_{4-x}Si(OR')_x$, where R' represents the desired functional group. A common example is methyltriethoxysilane (MTEOS $CH_3(C_2H_5O)_3Si$). This precursor has been used to provide hydrophobic surfaces [22].

The hydrophobicity of a surface is characterised by the contact angle of water on that surface. The contact angle of a drop of liquid on a surface refers

to the angle between the tangent to the drop and the surface. A contact angle greater than 90 ° characterises a hydrophobic surface, while a contact angle less than 90 ° characterises a hydrophilic surface.

A TEOS-xerogel layer is an example of a hydrophilic surface. Where a TEOS-xerogel will have hydroxyl groups at its surface, rendering the surface hydrophilic, in an MTEOS-xerogel these hydroxyls are replaced by alkyl groups. The alkyl groups, through their relatively low affinity for water, render the xerogel surface hydrophobic [23].

Since there are countless inorganic/organic component combinations available, with each combination offering particular properties, this implies that ORMOSILs can be used to provide glasses with whatever range of characteristics an application may require [24–28]. In this work, ORMOSILs are used to reduce cracking, increase glass porosity and also to increase the hydrophobicity of the glass surface, as in the example given above.

Producing hydrophobic surfaces of is particular importance in this work since the xerogels are fabricated for use as O_2 sensitive films. For the O_2 sensing mechanism to occur, the O_2 must first diffuse through the xerogel to the luminophore, as described in Section 2.4. In a humid environment, the xerogel surface will be exposed to water vapour. The nature of the xerogel surface determines how the water vapour will interfere with the O_2 sensing.

Water spreads out on a hydrophilic surface creating a barrier to O_2. In this instance, the O_2 molecules must partition through the water layer first and then diffuse through the sensor membrane. This increases the response time and can decrease the observed sensitivity of the sensor membrane.

A further disadvantage of hydrophilic membranes is the tendency to adsorb moisture from the atmosphere, causing changes in the microstructure of the host matrix. These changes lead to fluctuations in the emission signal of a luminophore embedded in such a matrix, resulting in an unreliable sensor system.

For a hydrophobic sensor membrane in a humid environment, water minimises contact with the surface and tends to form beads. Since the water

does not spread out on the surface, a much smaller surface area is covered by water and so O_2 can diffuse freely into the remaining surface area of the membrane.

Xerogels with high contact angles have been found to exhibit increased O_2 sensitivity in both gaseous and dissolved phase [29], and so such materials are desirable in this work.

In addition, combinations of organosilicon precursors are also used in this work to incorporate multiple features into the films, further exploiting the versatility of the sol-gel process.

3.6 Encapsulation of luminophores within the sol-gel matrix

Luminophores are probe or sensing molecules, that report on their environment by changes in their photophysical or photochemical properties.

The immobilisation of these probe molecules in a support matrix is required to produce a useable sensor platform. Since the probes report via variations in their luminescent properties, care must be taken to ensure that such variations do not occur by any means other than by the process under investigation (in this work the luminescence signal should vary only due to varying O_2 concentration). As such, the support matrix should provide a stable environment for the probe molecules, ideally, forming a barrier to substances that may interfere with their luminescent properties, preventing the molecules themselves contaminating the sample region, yet allowing sufficient access to the probe by the desired analyte. The support matrix itself should have a chemically inert microstructure, that will not undergo any structural changes which might in turn lead to fluctuations in the luminescent properties of the probe [30–32].

Additionally, the immobilistion process itself must not hamper the desirable luminescent properties of the probe molecules. Standard immobilisation

techniques can present difficulties, for example, the technique of physisorption can be prone to probe leaching, while the technique of covalent attachment is time consuming and may render the probe molecules less sensitive to the target analyte [33, 34]. The sol-gel route overcomes these issues, presenting the possibility of immobilising luminophores by encapsulation [35].

While glassy materials provide the characteristics required of a support matrix outlined above, the photophysical and photochemical properties of luminophores cannot withstand the high temperatures used in the production of conventional glasses. Sol-gel-based xerogels are produced at relatively low temperatures, in contrast to the elevated thermal conditions generally required in conventional melt glass production. It is this low temperature curing that allows the sol-gel process to be used to entrap luminescent molecules without altering their luminescence properties [36].

The encapsulation technique, by which luminophores can be immobilised in sol-gel glasses, involves adding the luminophore molecules to the sol solution prior to the formation of the gel. In this way, the sol-gel matrix is formed around the luminophore molecules. As such, the resulting glass/luminophore system is less susceptible to leaching than techniques such as post-doping [37].

3.7 Deposition techniques

3.7.1 Dip-coating

The dip-coating process can be divided in to five stages: immersion, start-up, deposition, drainage and evaporation [4]. The dip-coating apparatus used in this work allows the substrate to be fixed above a movable platform, which holds a vial containing the liquid sol. The vertical motion of the platform is controlled by the user via a software interface. Since the speed is controlled, reproducibility is ensured.

To begin coating, the platform is raised until the substrate is immersed in the liquid sol. The platform is then lowered at constant speed. The inner

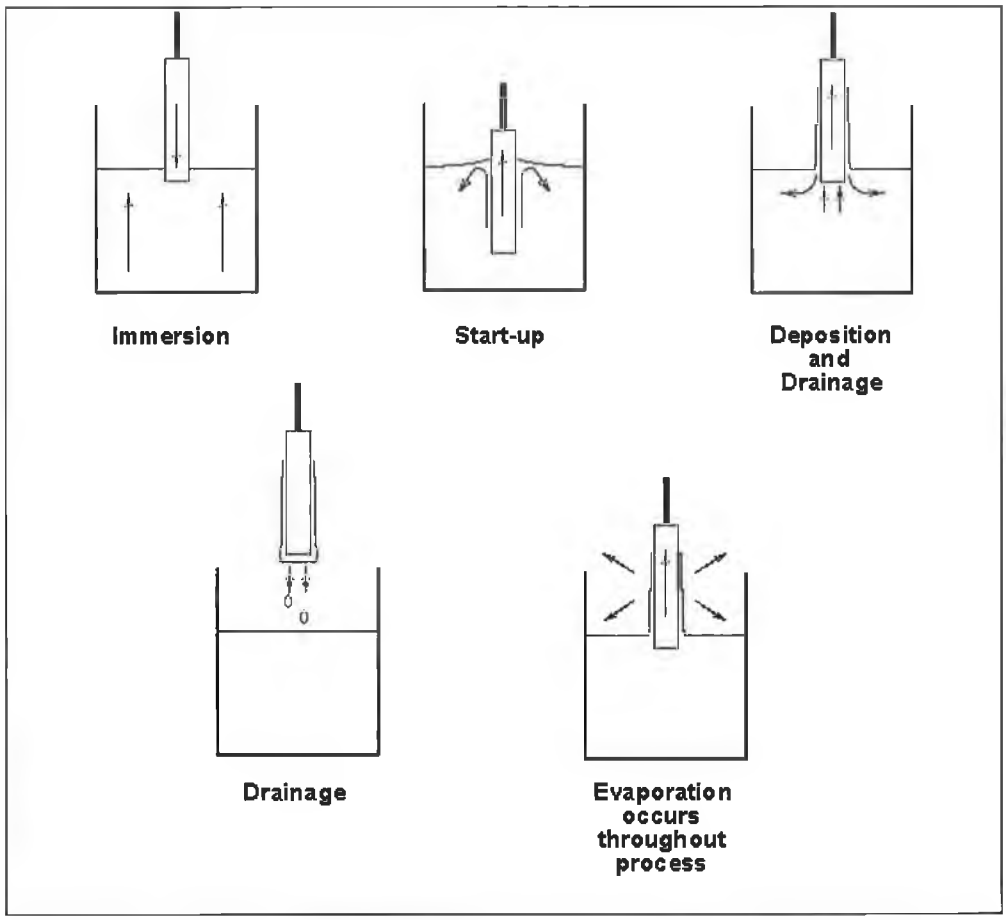

Figure 3.2: The dip-coating process

layer of sol, close to the substrate, moves upwards with the substrate, while the outer layer returns to the vial. The thickness of the resulting film is related to the distance between these two layers. The thickness and the position of these upward- and downward-moving layers are governed by six forces:

1. viscous drag upward on the liquid by the moving substrate,
2. the force of gravity,
3. resultant force of surface tension in the concavely curved meniscus,

4. inertial force of the boundary layer liquid arriving at the boundary region,

5. surface tension gradient and

6. the disjoining or conjoining pressure which is of importance for films less than 1μm thick, such as the films in this work.

Generally, for Newtonian fluids the relationship between the thickness, h, of the resulting coating and these six forces is governed by the following relationship:

$$h = 0.94 \frac{(\eta U)^{\frac{2}{3}}}{\gamma_{LV}^{\frac{1}{6}} (\rho g)^{\frac{1}{2}}} \tag{3.4}$$

where, η is the viscosity, ρ is the density, g is the acceleration due to gravity, γ is the surface tension and U is the dip speed.

However, due to the constantly evolving nature of sol-gels, this relationship does not hold for every sol. Small deviations from predicted behaviour can be explained by such factors as, non-Newtonian viscosity due to aggregation in the sol (especially after long aging times) and concentration dependence of the viscosity due to evaporation [14]. The main point to note is that the thickness of the deposited layer increases with dip speed.

3.7.2 Spin-coating

The spin-coating process may be divided into four stages: deposition, spin-up, spin-off and evaporation. The substrate to be coated is held in place via a chuck and a vacuum, with its surface in the horizontal plane. To begin coating, a quantity of liquid sol is deposited onto the centre of the substrate. In the spin-up stage, the substrate is set to rotate, causing the liquid to be drawn out toward the edges via centrifugal force. This is followed by the spin-off stage, where excess liquid, having flowed to the substrate edge, now leaves the substrate surface in droplets. The rate of removal of excess

liquid in this way, slows as the film becomes thinner and resistance to flow increases. In the fourth and final stage, evaporation becomes the primary cause of thinning [4].

The excellent film uniformity, typical of spin-coating, is due the balancing of the competing forces of the inward viscous drag and the outward centrifugal force [38].

Film thickness may be predicted using the following relation [39]:

$$h_f = c_0 \left[\frac{3\nu_0 \epsilon}{2(1 - c_0)\omega^2} \right]^{1/3} \tag{3.5}$$

where, h_f represents the final film thickness, c_0 is the initial sol concentration, ν_0 is the kinematical viscosity, ϵ is the rate of evaporation, and ω is the angular velocity. This relation assumes Newtonian fluid behaviour. As mentioned in the precious section, the sols in this work may deviate from Newtonian behaviour, however, the important point to note is that generally, film thickness is inversely proportional to spin speed.

3.7.3 Pin-printing

Pin-printing uses a conical pin-head to collect the liquid sol from a well and deposit it onto the substrate. The dimensions of the deposited discrete sensor layer are a function of, the pin dimensions, the relative humidity during printing, the pin contact time with the substrate, the nature of the substrate surface and the sol-gel solution's composition and chemistry [40].

Pin-printing has become a popular deposition choice due to the ease with which it may be used to produce microarrays of sensor elements. In addition, printing parameters and pattern details are preprogrammed, ensuring a high level of reproducibility while also facilitating high throughput techniques. These attractive features have been particulary exploited in the field of DNA microchip processing [41–43].

As the technique allows arrays of discrete sensor elements, small format sensor platforms may be produced, well suited to the current drive towards

miniturisation and portable sensor platforms. A further attractive feature is presented in that several wells may be used, each containing a sol solution, each sol being sensitive to a different analyte. This allows for the possibility of producing multianalyte sensor arrays.

3.7.4 Ink-jet-printing

Ink-jet-printing is a non-impact deposition technique where small droplets are directed, in rapid succession, onto the surface of a substrate under computer control. Of the various methods by which ink-jet-printing may be implemented the two most suited to practical applications are 'continuous jet' and 'drop on demand' [44].

The 'drop on demand' technique is implemented here. The liquid sol is held in a reservoir, the opening nozzle of which is controlled by a piezo-electric crystal. Commands at a software interface determine when and for how long the nozzle should open. In this work, patterning is made possible by placing the substrate on a moveable x-y stage, which is also controlled via a software interface.

Ink-jet-printing provides a practical alternative to dip- and spin-coating deposition, neither of which are practical for producing large quantities of sensor elements or for patterning. Ink-jet-printing is also relatively easy to implement in a production line setting, where neither dip- or spin-coating could be implemented. These considerations are of importance when considering the production of sensor elements for commercial use.

3.7.5 Gravure-printing

With gravure-printing an image is etched on the surface of a metal plate, the etched area is filled with ink, then the plate is rotated on a cylinder that transfers the image to the paper or other material. Gravure-printing is often used for high-volume printing of packaging, wallpaper, and giftwrap using

fast-drying inks. In this work, gravure-printing is highlighted as an excellent deposition solution for high throughput processing of sol-gel layers.

3.8 Gas transport in sol-gel films

As already described, the sensor platform in this work is based on an O_2-sensitive luminophore entrapped in a porous xerogel. As explained in Chapter 2, the sensing mechanism employed is collisonal luminescence quenching. By its nature, such a mechanism requires molecular contact of analyte and luminophore. This section illustrates the relevance of the process by which this contact is achieved.

The luminescence quenching of $[Ru(dpp)_3]^{2+}$ by O_2 is governed by the Stern-Volmer equation, see Equation 2.4. K_{SV} is the measure of O_2 sensitivity and, from Equation 2.5, this is dependent on τ_0 and P, the excited-state lifetime of the luminophore entrapped in the host material and the O_2-permeability of the host material, respectively. As given in Equation 3.6, P is a product of the O_2 diffusion coefficient, D, and O_2 solubility, S, in the host material.

$$P = D \times S \tag{3.6}$$

P is also related to the average pore radius of the material via Equation 3.7:

$$P = (1 - \rho)\frac{R_h^2}{f_s f_t} \tag{3.7}$$

where, ρ is the relative density of the film, R_h is the average pore radius, and f_s and f_t are factors accounting for the shape of the pores and the non-linear path in real materials [4]. The average pore radius is related to the volume porosity, V_p, of a material according to Equation 3.8. In this relation, A_p is the total surface area of the pores.

$$V_p = R_h \times A_p \tag{3.8}$$

Equations 3.6, 3.7 and 3.8, show the diffusion coefficient to be directly proportional to the square of the average pore radius which in turn is proportional to the volume porosity. Therefore, variations in D from material to material may be attributed to variations in volume porosity, all other terms being equal.

3.9 Conclusions

The principles behind the sol-gel process have been explained. The tunability of the process has been highlighted as the reason this process is used here to produce sensor support matrices. The influence of the process parameters and organosilicon alkoxide precursors on the resulting glass structure and chemical behavior have been outlined in terms of relevance to this work.

The sol-gel process produces glass at low temperatures and this has been noted as the reason this process is suited for the encapsulation of luminophores into the resulting glassy xerogels.

The deposition techniques of interest to this work have been described. Dip-coating has been presented as the primary technique by which thin films are produced in this work.

Diffusion in sol-gel xerogels is explained; since it is the diffusion of O_2 in the sol-gel matrix, to achieve molecular collision with the encapsulated luminophore, that forms the basis of the sensing mechanism at the core of this work.

The following chapter will present the experimental techniques used to produce and characterise sol-gel sensor layers.

Bibliography

[1] M. Ebelmen. Mémoire sur de nouvelles combinaisons de l'acide borique avec les éthers, et sur l'éther sulfureux. *Annales de Chimie et de Physique*, 17:54–73, 1846.

[2] J. D. MacKenzie. Sol-gel research-achievements since 1981 and prospects for the future. *Journal of Sol-Gel Science and Technology*, 26:23–27, 2003.

[3] *Sol-Gel processing*, volume 1 of *Handbook of Sol-Gel Science and Technology*. Kluwer Academic Publishers, Boston, 2005.

[4] C.J. Brinker and G.W. Scherer. *Sol-Gel Science: The Physics and Chemistry of Sol-Gel Processing*. Academic Press Inc., San Diego, 1990.

[5] J. Lin and C.W. Brown. Sol-gel glass as a matrix for chemical and biochemical sensing. *Trends in analytical chemistry*, 16(4):200–211, 1997.

[6] C. McDonagh, B.D. MacCraith, and A.K. McEvoy. Tailoring of sol-gel films for optical sensing of oxygen in gas and aqueous phase. *Analytical Chemistry*, 70:45–50, 1998.

[7] J.Y. Ying and J.B. Benziger. Structure tailoring of alkoxide silica. *Journal of Non-Crystalline Solids*, 147-148:222–231, 1992.

[8] I.M. Miranda Salvado, J. Santos Sousa, F.M.A. Margaca, and J. Teixeira. Structure of SiO_2 gels prepared with different water contents. *Physica B*, 276-278:388–389, 2000.

[9] B.D. MacCraith, C.M. McDonagh, G. O'Keeffe, A.K. McEvoy, T. Butler, and F.R. Sheridan. Sol-gel coatings for optical chemical sensors and biosensors. *Sensors and Actuators B*, 29:51–57, 1995.

[10] H. Schmidt. Chemistry of material preparation by the sol-gel process. *Journal of Non-Crystalline Solids*, 100:51–64, 1988.

[11] J.D. Mackenzie and D.R. Ulrich. *Ultrastructure Processing of Advanced Ceramics*. Wiley-Interscience, New York, 1988.

[12] L.C. Klein. *Sol-Gel technology for thin films, fibers, preforms, electronics, and specialty shapes*. Noyes Publications, Park Ridge, NJ, 1988.

[13] H. Schmidt, H. Scholze, and A. Kaiser. Principles of hydrolysis and condensation reaction of alkoxysilanes. *Journal of Non-Crystalline Solids*, 63:1–11, 1984.

[14] C. McDonagh, F. Sheridan, T. Butler, and B.D. MacCraith. Characterisation of sol-gel-derived silica films. *Journal of Non-Crystalline Solids*, 194:72–77, 1996.

[15] C. McDonagh, P. Bowe, K. Mongey, and B.D. MacCraith. Characterisation of porosity and sensor response times of sol -gel-derived thin films for oxygen sensor applications. *Journal of Non-Crystalline Solids*, 306:138–148, 2002.

[16] R. Gupta, S. Mozumdar, and N.K. Chaudhury. Effect of ethanol variation on the internal environment of sol-gel bulk and thin films with aging. *Biosensors and Bioelectronics*, 21:549–556, 2005.

[17] B. Linter, N. Arfsten, H. Dislich, H. Schmidt, G. Philipp, and B. Seiferling. A first look at the optical properties of ormosils. *Journal of Non-Crystalline Solids*, 100:378–382, 1988.

[18] J.D. Mackenzie and E.P. Bescher. Structures, properties and potential applications of ormosils. *Journal of Sol-Gel Science and Technology*, 13:371–377, 1998.

[19] H. Schmidt. Organic modification of glass structure. *Journal of Non-Crystalline Solids*, 112:419–423, 1989.

[20] G.R. Atkins and R.B. Charters. Optical properties of highly fluorinated and photosensitive organically-modified silica films for integrated optics. *Journal of Sol-Gel Science and Technology*, 26:919–923, 2003.

[21] C. Rottman, G. Grader, and D. Avnir. Polarities of sol-gel-derived ormosils and of their interfaces with solvents. *Chemistry of Materials*, 13:3631–3634, 2001.

[22] A.K. McEvoy, C.M. McDonagh, and B.D. MacCraith. Dissolved oxygen sensor based on fluorescence quenching of oxygen-sensitive ruthenium complexes immobilized in sol-gel-derived porous silica coatings. *Analyst*, 121(6):785–788, 1996.

[23] M. Park, S. Komarneni, and J. Choi. Effect of substituted alkyl groups on textural properties of ormosils. *Journal of Materials Sciences*, 33:3817–3821, 1998.

[24] J. Wen and G.L. Wilkes. Organic/inorganic hybrid network materials by the sol-gel approach. *Chem. Mater.*, 8:1997–1681, 1996.

[25] U. Schubert, N. Husing, and A. Lorenz. Hybrid inorganic-organic materials by sol-gel processing of organofunctional metal alkoxides. *Chemistry of Materials*, 7:2010–2027, 1995.

[26] K. Satoh and H. Nakazumi. Sol gel preparation of photosensitive fluorinated inorganic organic thin films for printing plates. *Thin Solid Films*, 460:217–221, 2004.

[27] K. Haas. Hybrid inorganic-organic polymers based on organically modified si-alkoxides. *Advanced Engineering Materials*, 2(9):571–582, 2000.

[28] M.R. Phelps, J.B. Hobbs, D.G. Kilburn, and R.F.B. Turner. An autoclavable glucose biosensor for microbial fermentation monitoring and control. *Biotechnology and bioengineering*, 46:514–524, 1995.

[29] Z. Tao, E.C. Tehan, Y. Tang, and F.V. Bright. Stable sensors with tunable sensitivities based on class II xerogels. *Analytical Chemistry*, 78(6):1939–1945, 2006.

[30] R.T. Bailey M.C. Tedford R.N. Gillanders, P.J. Crilly. Thin film dissolved oxygen sensor based on platinum octaethylporphyrin encapsulated in an elastic fluorinated polymer. *Analytica Chimica Acta*, 502:1–6, 2004.

[31] G.A. Baker, B.R. Wenner, A.N. Watkins, and F.V. Bright. Effects of processing temperature on the oxygen quenching behavior of tris(4,70-diphenyl-1,100-phenanthroline) ruthenium (II) sequestered within sol-gel-derived xerogel films. *Journal of Sol-Gel Science and Technology*, 17:71–82, 2000.

[32] B.C. Dave, B. Dunn, J. Selverstone Valentine, and J.I. Zink. Sol-gel encapsulation methods for biosensors. *Analytical Chemistry*, 66(22):1120A, 1994.

[33] C.M. Ingersoll and F.V. Bright. Toward sol-gel-processed chemical sensing platforms: effects of dopant addition time on sensor performance. *Journal of Sol-Gel Science and Technology*, 11:169–176, 1998.

[34] C. Rottman and D. Avnir. Effects of water/silane r-ratio and of humidity on properties of sol-gel entrapped indicators. *Sol-Gel Optics V - Proceedings of SPIE Vol. 3943 (2000)*, 2000.

[35] B.D. MacCraith. Enhanced evanescent wave sensors based on sol-gel-derived porous glass coatings. *Sensors and Actuators B*, 11:29–34, 1993.

[36] D. Avnir, D. Levy, and R. Reisfeld. The nature of the silica cage as reflected by spectral changes and enhanced photostability of trapped rhodamine 66. *The Journal of Physical Chemistry*, 88:5956–5959, 1984.

[37] O. Lev, M. Tsionsky, L. Rabinovich, V. Glezer, S. Sampath, I. Pankratov, and J. Gun. Organically modified sol-gel sensors. *Analytical Chemistry*, 67(1):A22–A30, 1995.

[38] A.G. Emslie, F.T. Bonner, and L.G. Peck. Flow of a viscous liquid on a rotating disk. *Journal of Applied Physics*, 28(5):858–862, 1958.

[39] D. Meyerhofer. Characteristics of resist films produced by spinning. *Journal of Applied Physics*, 49(7):3993–3997, 1978.

[40] E.J. Cho and F.V. Bright. Integrated chemical sensor array platform based on a light emitting diode, xerogel-derived sensor elements, and high-speed pin printing. *Analytica Chimica Acta*, 470:101–110, 2002.

[41] J. Ziauddin and D.M. Sabatini. Microarrays of cells expressing defined cDNAs. *Nature*, 411:107–110, 2001.

[42] B. Lemieux, A. Aharoni, and M. Schena. Overview of DNA chip technology. *Molecular Breeding*, 4:277–289, 1998.

[43] M. Schena, D. Shalon, R.W. Davis, and P.O. Brown. Quantitive monitoring of gene epression patterns with a complementary DNA microarray. *Science*, 270:467–470, 1995.

[44] *The printing ink manual.* Kluwer Academic Publishers, Dordrecht, The Netherlands, 5th edition, 1993.

Chapter 4

Experimental Characterisation Systems, Techniques & Fabrication of Sensor Elements

In this work, optical O_2 sensing is achieved by observing the collisional quenching, by O_2, of a luminophore, entrapped in a porous sol-gel xerogel.

O_2-sensitivity is characterised in terms of the Stern-Volmer constant, K_{SV}. As already discussed, K_{SV} is a function of both τ_0, which is a characteristic of the luminophore; and P, which is a characteristic of the host matrix in which the luminophore resides. By determining the values of τ_0 and P for each luminophore-doped xerogel, we can establish the origins of O_2-sensitivity.

Luminescence lifetime and intensity measurements are made in order to determine the dependence of the luminophore lifetime on O_2 concentration and also on the host membrane. The laser system, employed to monitor the luminescence lifetime, and the LED-based system, used to obtain intensity data, are presented in this chapter.

The principles governing the phase fluorometry technique have already been explained in Chapter 2. In this chapter, the laboratory apparatus used to implement this technique will be described.

Spectroscopic ellipsometry is introduced as the means by which the refractive index of xerogel layers was determined. The techniques by which porosity information has been obtained from refractive index data are explained here.

The host materials are characterised in order to understand the transport of O_2 to the luminophore. This requires the determination of, the hydrophobicity of the xerogel, the solubility of O_2 in the xerogel and the O_2 diffusion coefficient of the xerogel. This chapter describes each of the characterisation techniques used in this work to determine these properties.

4.1 Sensor Element Fabrication

Both luminophores and sol-gel materials have been discussed in Chapter 2 and Chapter 3, respectively. In this section, the details of combining the two to form O_2-sensitive membranes are presented.

The process parameters particular to film formation are outlined. The deposition techniques used are also detailed.

It will be shown that all O_2-sensitive xerogels in this work are produced in a simple, reproducible fabrication process, that would lend itself to mass production and commercialisation.

4.1.1 Fabrication of O_2-sensitive xerogels

Xerogels are produced with the following precursors: tetraethoxysilane (TEOS), phenyltriethoxysilane (PhTEOS), methyltriethoxysilane (MTEOS), ethyltriethoxysilane (ETEOS), n-propyltriethoxysilane (PTEOS).

Sols were prepared by acid-catalysed hydrolysis and polycondensation of the relevant precursor. An R-value of 4 was maintained in each sol. Typically, the luminophore was combined with ethanol, to which aqueous HCl at pH 1 was added. The precursor was then added drop-wise to give a final luminophore concentration of 2.5g/L, with respect to the total vol-

ume of the solution. The total molar ratio of silane:ethanol:water:HCl, was 1:6.25:4:0.007.

The final mixture was magnetically stirred under ambient conditions to ensure adequate mixing. Following stirring, sols were aged, as required, to achieve a level of viscosity suitable to allow coating of substrates.

This work does not extend to developing sol formulations, rather the details of the formulation of these sols have been developed by other authors and have been reported previously [1, 2].

Xerogels have also been formed from precursor solutions of n-octyltriethoxysilane and TEOS (OTEOS:TEOS); and also 3,3,3-trifluoropropyltrimethoxysilane and n-propyltrimethoxysilane (TFP-TMOS:PTMOS).

OTEOS:TEOS and TFP-TMOS:TMOS sols were produced as described by Bright et al. [3, 4].

4.1.2 Substrate preparation

Glass microscope slides were used as substrates for: luminescence quenching experiments; contact angle and thickness measurements; and obtaining absorption and emission spectra. Pieces of silica wafer, were used as substrates for: ellipsometeric and FTIR measurements. Substrates were treated by soaking in 30% HNO_3 for at least 24 hours. Substrates were removed from the acid, then rinsed with copious amounts of deionised water and ethanol, before drying under a N_2 flow.

4.1.3 Xerogel formation

A study of deposition techniques has been carried out as part of this work. The techniques studies are: dip-coating, spin-coating, stamp-coating, ink-jet-printing, pin-printing and gravure-printing. The details of the implementation of these techniques is presented in this section. Following deposition all samples are cured via a temperature program.

Dip-coating

Thin film xerogels were formed by dip-coating liquid sols onto glass subtrates in a controlled environment using a computer controlled dipping apparatus. A dip-speed of 3 mm/s was used for all samples, unless otherwise stated. The glass substrates were 1 cm x 2 cm pieces scribed from 1mm thick microscope slides (Menzel Glass). Samples produced in this way represent the majority of samples described in this work.

Spin-coating

For each sample, 50μL of liquid sol was deposited onto the glass substrate, using a micropipette. The film was formed by rotating the substrate at 3000 rpm for 30 s, unless otherwise stated.

Stamp-coating

Substrates to be coated are placed in a glass petri-dish. Stamp-coated films are formed by depositing the liquid sol-gel onto the substrate surface with the use of a PDMS stamp.

As stamp-coating is done by hand, the technique is not suited to producing a large number of samples nor is it reproducible. However, it is useful when preparing samples for experiments that require a coating to be either thicker, or of a smaller surface area, than is possible to obtain with dip-coating. In this work the experimental apparatus used to determine the response time of the sensor elements, requires stamp-coated samples.

Pin-printing

A Cartesian Technologies MicroSys 5100 MicroArrayer (Genomic Solutions, UK) was employed to deposit patterns of discrete sensor elements onto substrates. At the software interface, the pin speed and dimensions of the required patterns were specified. Since the pin-printing mechanism is contained

in an environmental chamber the relative humidity could be controlled during deposition.

Ink-jet-printing

Patterns of sensor elements were deposited onto substrates using an ink-jet printing system (MicroFab Technologies). The amount of sol to deposit and dimensions of the required patterns were specified at a software interface. A moveable x-y stage was used to align the substrates.

Gravure-printing

A commercial company, Gas Sensing Solutions (GSS), provided samples deposited by gravure-printing. The samples were produced from an MTEOS-based sol. Details of these samples complete the review of deposition techniques presented in Chapter 9.

4.2 Luminescence Lifetime Measurements

In this work, the intrinsic excited state lifetime of $[Ru(dpp)_3]^{2+}$ in each xerogel, was determined by experiments using a pulsed laser system both in the School of Chemical Sciences in DCU and also in the State University of New York (SUNY), at Buffalo, as part of collaborative work with colleagues in the USA.

The DCU system has been described elsewhere [5]. Briefly, it consists of a Nd:Yag laser (λ = 355 nm). Samples were excited with 15 ns pulses. Samples were degassed in N_2 prior to measurements. The emitted decay signal was detected using a photomultiplier tube and captured using a digital oscilloscope. The luminescence lifetime was calculated by analysing the decay trace in Microcal Origin.

Experiments in SUNY, were conducted in a similar manner [6].

4.3 Determination of the O_2 response of sensor membranes

4.3.1 Intensity Measurements

The O_2-sensitivity of luminophores embedded in xerogels can be quantified by luminescence intensity measurements [7]. In this work, the intensity of the luminescence signal, from a sensor sample contained in a flow cell and excited by a blue LED (Nichia, NSPE590), is detected by a silicon photodiode (Radionics, 194-290), the output of which is connected to the lock-in amplifier (Signal Recovery, Model 7225). The output from the lock-in amplifier, in millivolts, is written to file on the PC, via a National Instruments data acquisition card, at known O_2 concentrations. The Stern-Volmer plot can then be produced from this data.

4.3.2 Phase Fluorometry

It has been established that intensity-based measurements can suffer from issues such as, baseline drift due to light source and detector fluctuations [8]. As such, lifetime measurements are preferred. However, direct lifetime measurements, as those describe above, require costly equipment and involve significant data analysis, by fitting data to exponential decay models [9, 10].

Phase fluorometry offers a low-cost alternative to direct lifetime measurements, while remaining free of the artifacts associated with intensity-based measurements [11].

The principles of phase fluorometry have been presented in Chapter 2. The experimental system used here to examine the performance of the O_2 sensor membranes has been published previously [12]. Briefly, the characterisation system consists of a blue LED (Nichia, NSPE590), which is modulated at a frequency of 20 kHz and whose emission spectrum overlaps very well with the absorption band of the ruthenium complex used here, as shown in Figure

2.2. A silicon photodiode (Radionics, 194-290) was used for the detection of the O_2-sensitive luminescence signal.

In order to examine their performance, O_2 sensor xerogels were placed in a flow cell into which controlled mixtures of O_2 and N_2 were introduced using mass flow controllers (Celerity, Ireland). The concentration of O_2 flowing into the flow cell can be set via a Labview user interface. O_2 concentration is increased from 0 to 100%, in predefined intervals. Gas quantities are accurate to $\pm$ 1%. The duration of each interval is typically 1.5 min to ensure a new equilibrium point has been reached.

Response times of this system when using the xerogels reported here is <5 s. However, the intrinsic response time of the membranes is <1s [13]. The phase angle at each concentration is recorded (as in the previous section) and from this data, the corresponding Stern-Volmer plot can be recovered.

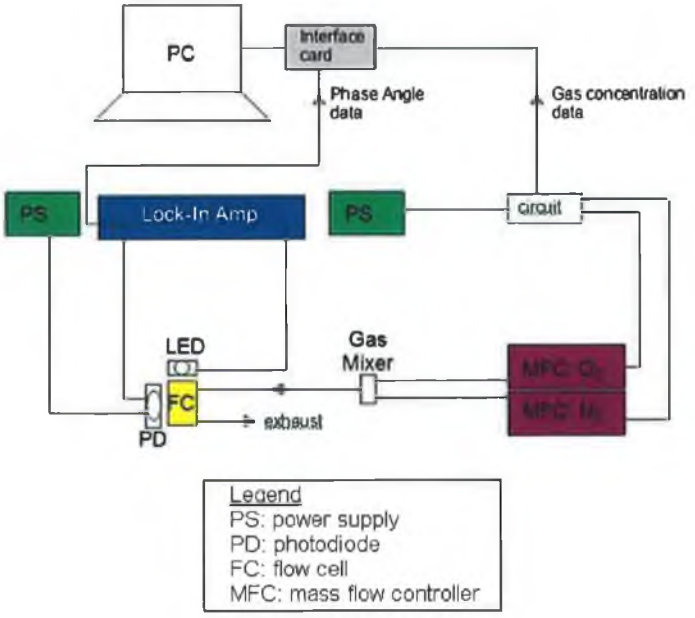

Figure 4.1: Schematic of Phase Fluorometry System

4.4 Determination of the effect of solvent vapour on the response of O_2 sensor membranes

As described in Section 4.3.2, the O_2 response of the sensor membranes is determined by monitoring the luminescence signal at known O_2 concentrations, where N_2 is the carrier gas. In order to investigate how solvent vapour might affect the sensor response of the O_2-sensitive membranes, the O_2/N_2 gas mixture was passed through a wash bottle containing the solvent to be investigated, before entering the flow cell. The resulting phase data could then be compared to phase data taken without the wash bottle in the gas flow path.

In order to establish the extent of solvent interference on dissolved O_2 sensing, the xerogel was contained in a cuvette, into which known quantities of ethanol and deionised water were added using disposable pipettes. Phase data was recorded and compared to that of a xerogel in a cuvette of deionised water.

4.5 Spectroscopic Ellipsometry

4.5.1 Introduction

Based on the measurement of the change in light polarization upon reflection from a sample surface, ellipsometry derives thin film thickness and optical properties with extreme accuracy [14].

Ellipsometry means measuring an ellipse. Electromagnetic (EM) radiation is described not only by its wavelength and intensity, but also by its polarisation. Linearly polarised light reflecting from a flat surface generally becomes elliptically polarized after reflection, as illustrated in Figure 4.2. The two components of the EM wave, one in the plane of incidence (p) [1], and the

[1] p and s refer to the electric component of the EM wave.

other perpendicular (s) [1] to the plane of incidence, experience different attenuation and phase shift at the reflection [15], which can be described by Fresnel reflection coefficients r_p and r_s.

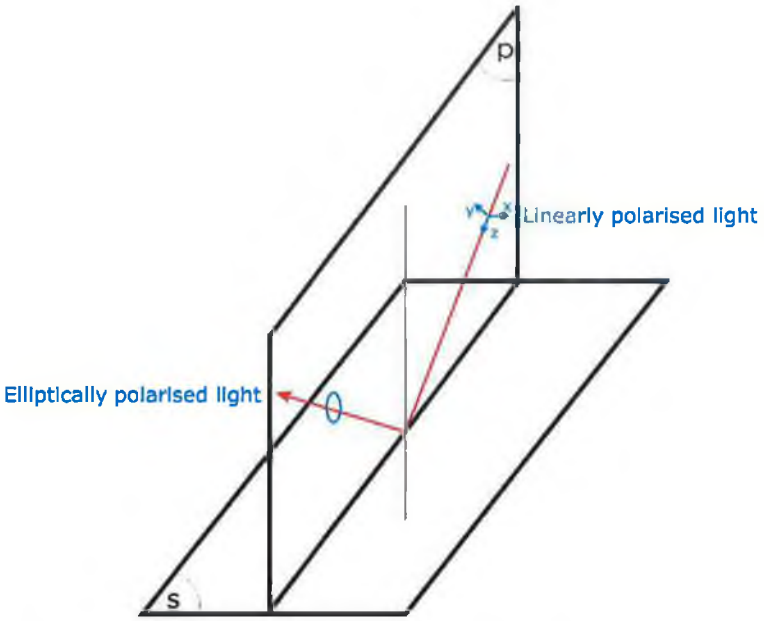

Figure 4.2: Changes in the polarization of light by reflection from a surface

Ellipsometry measures the ratio of these complex reflection coefficients, r_p and r_s. The measured data is expressed as Δ and Ψ, which represent the change in phase and amplitude, respectively, that occurs upon reflection. Δ and Ψ are related to the ratio, ρ, of r_p and r_s in Equation 4.1 [16]. In Equation 4.3, δ_p and δ_s refer to the phase of that component, relative to the other.

$$\rho = \frac{r_p}{r_s} = \tan\Psi e^{i\Delta} \tag{4.1}$$

where,

$$\tan\Psi = \frac{|r_p|}{|r_s|} \tag{4.2}$$

[1] p and s refer to the electric component of the EM wave.

$$\Delta = \delta_p - \delta_s \tag{4.3}$$

Since ellipsometry measures the ratio of two values, this technique provides highly accurate, very reproducible measurements that are not intensity dependent.

The discussion so far refers to the simplified two-phase situation, where the interaction occurs at the interface of two materials of different refractive index. In this work, layered structures are examined and so the system becomes three-phase, as in Figure 4.3. The reflected light in a three-phase system is the sum of the contributions of reflected and transmitted light at each individual interface. As such, the resulting effective reflection coefficients of a multi layer structure are a function of r_p and r_s for each layer [17] and are denoted as R_p and R_s (where, $R_p = \sum r_p$ and $R_s = \sum r_s$, respectively, over all the layers of the system).

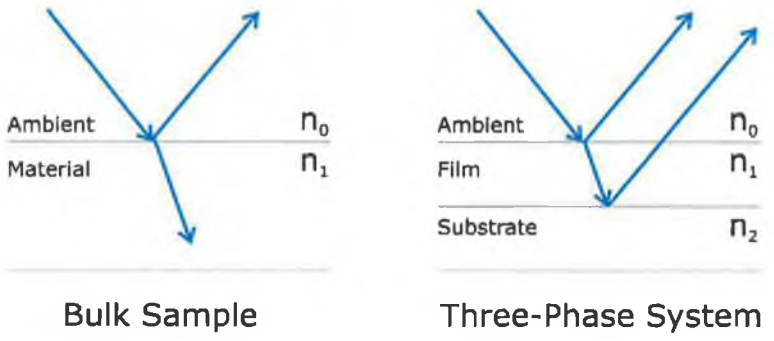

Figure 4.3: Comparing reflection from a bulk sample and a thin film

The ellipsometer (Jobin-Yvon Horiba, UVISEL) used in this work, is shown in schematic form in Figure 4.4. It consists of: a Xenon light source, a polarizer, a sample stage, a photo-elastic modulator (PEM), an analyser, a monochromator and a data acquisition unit. The Xenon light source provides a broad spectral range, from the FUV (190 nm) to the NIR (1.7 μm).

Generally, information such as refractive index or film thickness cannot be accessed directly from the Δ and Ψ wavelength dependent data obtained

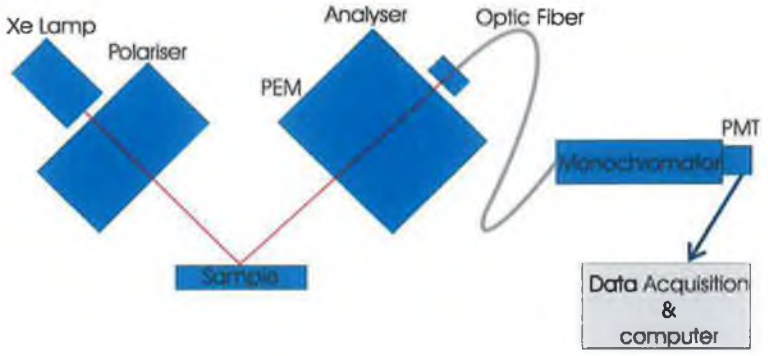

Figure 4.4: Schematic of spectroscopic ellipsometer

from ellipsometry. A mathematical model is required to fit the experimental data and it is from this mathematical representation of the sample that the characteristic information of the sample can be determined.

In this work, all ellipsometric data was recorded at an incidence angle of 70 ° and was analyzed using the Delta-Psi software Version 2.0. The ellipsometric data was modelled using the Tauc-Lorentz relation [18]. The parameters in the model were set to be close to expected values and known information on layer thickness (determined independently using a white light interferometer), was also included to help define the layered sample.

The following sections describe how ellipsometry is used in this work to determine porosity information in a technique known as ellipsometric porosity. In this technique, ellipsomtry is used to measure refractive index changes which in turn provide the volume porosity, V_p and the pore size distribution, PSD.

4.5.2 Experimental procedure: determining volume porosity, V_p, from refractive index

The sample is placed in a flow cell on the table of the ellipsometer. Dry N_2 is flowed into the flow cell to remove any physisorbed water from the pores of the sample [19]. Once humidity in cell has stabilised at 0 %, the ellipsometric

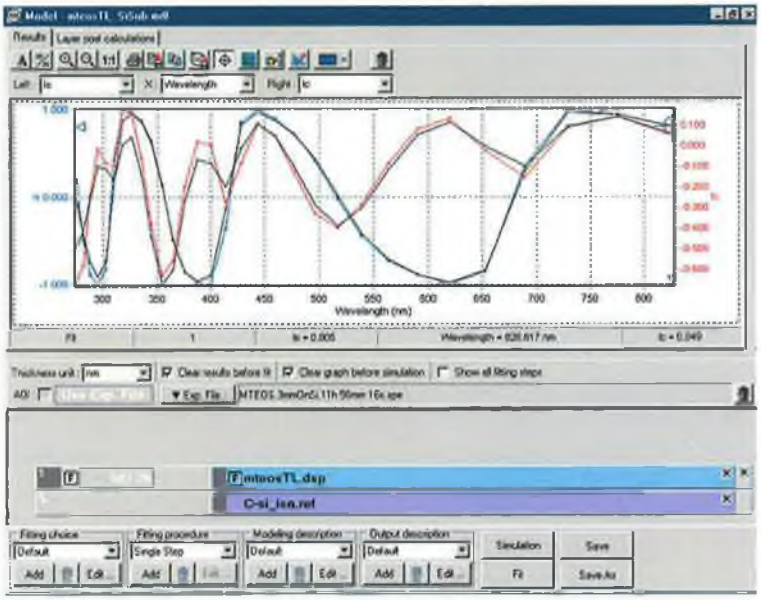

Figure 4.5: Screen grab of model used to recover optical properties from the ellipsometric data of an MTEOS-xerogel

data can be taken.

Humid air is then introduced to the cell until the humidity stabilises close to 100 %, at which point the ellipsometric data can be taken.

The values of refractive index with pores empty and full of adsorbent, are applied to Equation 4.4, the Lorentz-Lorenz equation:

$$\frac{{n_f}^2 - 1}{{n_f}^2 + 2} = (1 - V_p)\frac{{n_s}^2 - 1}{{n_s}^2 + 2} + V_p\frac{{n_p}^2 - 1}{{n_p}^2 + 2} \tag{4.4}$$

where, n_f, n_s and n_p are the refractive indices of the film, solid skeleton and pores respectively. By solving the simultaneous equations, the values of V_p and n_s can be determined. This approach has been widely reported in literature as a means to determine porosity [20].

This approach is based on the assumption that all pores are accessible to the adsorbent, it does not allow for the presence of closed pores within the material. However, the consistency of the results and the correlation with

the diffusion coefficient data imply that the approach is sufficient for this study.

4.5.3 Experimental procedure: determining the pore size determination (PSD)

Many authors have reported using the technique of ellipsometric porosimetry, or molecular probing, to determine the PSD of materials [21,22]. The PSD is obtained by monitoring the change in refractive index, as adsorbent vapour concentration is increased from 0 to 100 %. This section describes how the technique was implemented here, to provide information on the pores of xerogels.

In a similar manner to the previous section, the sample is placed in a flow cell on the table of the ellipsometer. Dry N_2 is flowed [19,23] to remove any physisorbed water from the pores. Once humidity in the cell has stabilised at 0 %, the ellipsometric data can be taken.

Humid air is then introduced to the cell, at 10 % intervals of relative humidity. Relative humidity within the cell is allowed to stabilise at each interval before the ellipsometric data can be taken.

Refractive index values are recovered from the ellipsometric data as in the previous section.

$$Vol_{ads} = \frac{(\frac{n_f^2-1}{n_f^2+2}) - (\frac{n_0^2-1}{n_0^2+2})}{(\frac{n_{ads}^2-1}{n_{ads}^2+2})} \tag{4.5}$$

Using Equation 4.5, the volume of the adsorbent within the xerogel pores, Vol_{ads}, for a given interval, may be determined, where n_f is the refractive index value at a given interval of relative humidity, n_0 is the refractive index value at 0 % RH, and n_{ads} is the refractive index of the adsorbent. This data was used to plot adsorption and desorption isotherms for each xerogel with a range of different adsorbents.

The derivative of the desorption branch of such an isotherm provides the pore size distribution (PSD) for the xerogel [24].

4.6 Diffusion Coefficient Measurements

The diffusion coefficient for xerogels of known thickness was determined from response time data, obtained during a step change in O_2 concentration, using a technique reported previously by this group [25]. The technique is based on a model developed by Mills and Chang [26].

4.6.1 Thickness measurements

Thickness measurements were made using a white light interferometer, (WYCO, N1100 Optical Surface Profiler). Using the interferometer in vertical scanning interferometry (VSI) mode allowed film thickness to be determined in a non-destructive manner by measuring the changes in an interference pattern.

The basic interferometric principle is that light reflected from a reference mirror combines with light reflected from a sample to produce interference fringes, where the best-contrast fringe occurs at best focus. In VSI mode, the white-light source is filtered with a neutral density filter, which preserves the short coherence length of the white light, and the system measures the degree of fringe modulation, or coherence [27].

4.6.2 Response time measurements

Response time measurements were made by recording the luminescence signal from a sensor layer during a change from vacuum to O_2-saturated conditions.

To ensure the response time measured was the intrinsic response of the sensor layer and did not include the time required to fill the gas lines and flow cell, a method including a fast switching solenoid valve was employed. The method and apparatus has been described in detail elsewhere [13]. Briefly,

one outlet of the solenoid valve was connected to an edge-detection flow-cell which contained the sample sensor layer, as depicted in Figure 4.6. The other two outlets were connected to a vacuum pump and O_2 supply, respectively. Both the vacuum and O_2 flow were continuously supplied throughout at a constant flo rate. Through a LabView interface it was possible to switch the solenoid value from vacuum to O_2 flow, thereby exposing the sample to alternate environments, as desired.

Excitation illumination, emission detection and data recording was all performed as outlined earlier for intensity measurements in Section 4.3.1.

The response time t_{90} is obtained from the luminescence signal, where t_{90} is the time taken for the intensity of the luminescence to decrease to 90 % of the equilibrium value [13].

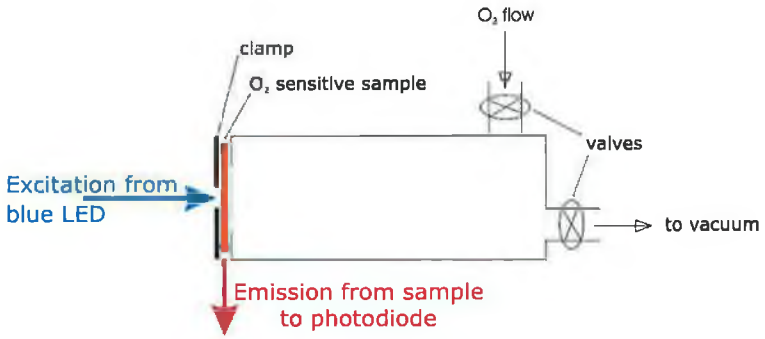

Figure 4.6: Schematic diagram of solenoid value used in response time experiments

4.7 Contact Angle Determination

Contact angle measurements were used to characterise the hydrophobicity of the xerogel surfaces of interest in this work. The measurements were made using the FTA-200 contact angle analyser (First Ten Angstroms, USA) shown in Figure 4.7.

Using the FTA-200, computer software analyses the drop shape of a liquid

Figure 4.7: Image of FTA-200 contact analyser. Reproduced from FTA literature.

on the surface to be characterised, and reports contact angle data with minimal requirement for operator intervention [28]. Contact angles reported here are accurate to $\pm 3°$. Figure 4.8 is a screen-shot showing the captured image of a drop of water on an ETEOS-xerogel, taken with the FTA software.

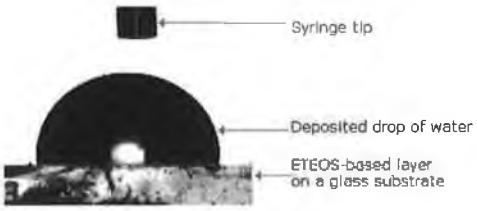

Figure 4.8: Image of drop of water on an ETEOS-xerogel. Captured using FTA camera and software.

4.8 Conclusions

This chapter describes the various experimental techniques and systems used in this work to charaterise O_2-sensitive xerogels.

In the first section, all precursors used in this work were listed and the fabrication procedures, including deposition techniques are reported.

Systems used to characterise the O_2-sensitive luminescence signal in both the time- and intensity- domain have been presented. The experimental system by which phase fluorometry is executed in this work has been detailed.

Spectroscopic ellipsometry has been introduced as the means by which refractive index values were obtained. The techniques used to recover porosity information from these refractive index values have been explained.

The technique used to calculate diffusion coefficient values from the response time data of xerogels of known thickness was outlined.

The commercial apparatus for obtaining contact angle data was also reported.

Each of these techniques are employed to establish the origin of the O_2 response sensitivity. The results of the characterisation process are presented in the following chapters.

Bibliography

[1] A.K. McEvoy. *Development of an optical sol-gel based dissolved oxyen sensor*. PhD thesis, Dublin City University, 1996.

[2] D. Wencel, C. Higgins, A. Klukowska, B.D. MacCraith, and C. McDonagh. Novel sol-gel derived films for luminescence-based oxygen and pH sensing. *Materials Science*, (accepted October 2006).

[3] Y. Tang, E.C. Tehan, Z. Tao, and F.V. Bright. Sol-gel-derived sensor materials that yield linear calibration plots, high sensitivity, and long-term stability. *Analytical Chemistry*, 75:2407–2413, 2003.

[4] R.M. Bukowski, R. Ciriminna, M. Pagliaro, and F.V. Bright. High-performance quenchometric oxygen sensors based on fluorinated xerogels doped with $[Ru(dpp)_3]^{2+}$. *Analytical Chemistry*, 77:2670–2672, 2005.

[5] B.S. Creaven, M.W. George, A.G. Ginzburg, C. Hughes, J.M. Kelly, C. Long, I.M. McGrath, and M.T. Pryce. Laser-pulse photolysis and transient infrared investigation into the effect of solvent or substituents (X) on the reactivity of photogenerated (η^6-$C_6H_{6-y}X_y$)$Cr(CO)_2$ intermediates. *Organometallics*, 12(8):3127–3131, 1993.

[6] G.A. Baker, B.R. Wenner, A.N. Watkins, and F.V. Bright. Effects of processing temperature on the oxygen quenching behavior of tris(4,70-diphenyl-1,100-phenanthroline) ruthenium (II) sequestered within sol-gel-derived xerogel films. *Journal of Sol-Gel Science and Technology*, 17:71–82, 2000.

[7] A.K. McEvoy, C.M. McDonagh, and B.D. MacCraith. Dissolved oxygen sensor based on fluorescence quenching of oxygen-sensitive ruthenium complexes immobilized in sol-gel-derived porous silica coatings. *Analyst*, 121(6):785–788, 1996.

[8] H.M. Rowe, S.P. Chan, J.N. Demas, and B.A. DeGraff. Elimination of fluorescence and scattering backgrounds in luminescence lifetime measurements using gated-phase fluorometry. *Analytical Chemistry*, 74:4821–4827, 2002.

[9] E.R. Carraway, J.N. Demas, B.A. DeGraff, and J.R. Bacon. Photophysics and photochemistry of oxygen sensors based on luminescent transition-metal complexes. *Analytical Chemistry*, 63:337–342, 1991.

[10] E.R. Carraway, J.N. Demas, and B.A. DeGraff. Luminescence quenching mechanism for microheterogeneous systems. *Analytical Chemistry*, 63:332–336, 1991.

[11] C. McDonagh, C. Kolle, A.K. McEvoy, D.L. Dowling, A.A. Cafolla, S.J. Cullen, and B.D. MacCraith. Phase fluorometric dissolved oxygen sensor. *Sensors and Actuators B*, 74:124–130, 2001.

[12] D. Wencel, C. Higgins, A. Guckian, C. McDonagh, and B.D. MacCraith. Novel hybrid sol-gel materials for smart sensor windows. *Proceedings SPIE, OptoIreland*, 5826:696–705, 2005.

[13] C. McDonagh, P. Bowe, K. Mongey, and B.D. MacCraith. Characterisation of porosity and sensor response times of sol -gel-derived thin films for oxygen sensor applications. *Journal of Non-Crystalline Solids*, 306:138–148, 2002.

[14] K. Vedam. Spectroscopic ellipsometry: a historical overview. *Thin Solid Films*, 313-314:1–9, 1998.

[15] M. Born and E. Wolf. *Principles of Optics*. Pergamon Press, Oxford, 6th edition, 1980.

[16] H.G. Tompkins. *A user's guide to ellipsometry.* Academic Press Limited, London, 1993.

[17] R.M.A. Azzam and N.M. Bashara. *Ellipsometry and Polarized Light.* Elsevier Science Publishers, Amsterdam, 1987.

[18] G.E. Jellison and F.A. Modine. Parameterization of the optical functions of amorphous materials in the interband region. *Applied Physics Letters*, 69(3):371–373, 1996.

[19] R.M. Almeida. Sol-gel silica films on silicon substrates. *International Journal of Optoelectronics*, 9(2):135–142, 1994.

[20] F. Horowitz, E.J.C. Dawnay, M.A. Fardad, M. Green, and E.M. Yeatman. Towards better control of sol-gel film processing for optical device applications. *Journal of Nonlinear Optical Physics and Materials*, 6(1):1–18, 1997.

[21] M.R. Baklanov and K.P. Mogilnikov. Characterisation of porous low dielectric constant films by ellipsometric porosimetry. *Semiconductor Fabtech - 14th Edition.*

[22] Q.T. Le, C.M. Whelan, H. Struyf, S. Vanhaelemeersch, A. Azioune, P. Louette, J.J. Pireaux, and K. Maex. Polymer dielectric treatment using ultraviolet-ozone: a photoelectron spectroscopy and ellipsometric porosimetry study. *Journal of Applied Physics*, 96(7):3807–3810, 2004.

[23] A. Bourgeois, A. Brunet Bruneau, S. Fisson, B. Demarets, D. Grosso, F. Cagnol, C. Sanchez, and J. Rivory. Determination of pore size distribution in thin organized mesoporous silica films by spectroscopic ellipsometry in the visible and infrared range. *Proceedings of the 30th International Conference on Metallurgie, Apr 28-May 2 2002*, pages 46–50.

[24] S.J. Gregg and K.S.W. Sing. *Adsorption, Surface Area and Porosity.* Academic Press, London, 1978.

[25] P. Bowe. *Characterisation of porosity and sensor response times of sol-gel-derived thin films for oxygen sensor applications*. MSc, Dublin City University, 2002.

[26] A. Mills and Q. Chang. Modelled diffusion-controlled response and recovery behaviour of a naked optical film sensor with a hyperbolic-type response to analyte concentration. *Analyst*, 117:1461–1466, 1992.

[27] C. Lamb and M. Zecchino. *WYKO Surface ProfilersTechnical Reference Manual*. Veeco Metrology Group, Printed in the United States of America., 1999.

[28] First ten angstroms - product brief, 1999.

Chapter 5

Optimising O_2 Sensor Platforms

5.1 Introduction

This chapter presents the O_2-sensitive luminophore-xerogel systems investigated in this work and highlights how the fabrication process has been adapted to produce systems suitable for particular applications.

The initial objective was to obtain maximum O_2 sensitivity. Two approaches were undertaken to achieve this goal. The first approach exploits the versatile nature of the sol-gel process, to produce materials exhibiting characteristics that yield increased O_2 sensitivity. The second approach looks at chemical modification of the O_2-sensitive luminophore complex to increase its excited-state lifetime.

The O_2 sensitivity of each system is presented in terms of the Stern-Volmer constant, recovered from the two-site Demas model. Other parameters such as, diffusion coefficient, water contact angle and excited-state lifetime of the luminophore complex in each host xerogel have also been determined with a view to establishing the origins of O_2 sensitivity for these materials.

Additional issues relevant to producing viable, reliable sensor platforms have been addressed. Specifically, these issues are, the possibility of sterilising

the sensor membranes, without altering O_2 sensitivity, and the ability of sensor membranes to retain their photostablity over prolonged periods of illumination by the excitation source. The manner in which these issues have been addressed is presented in this chapter.

5.2 Optimising O_2 sensitivity

5.2.1 Benchmark O_2 Sensor Membrane: MTEOS

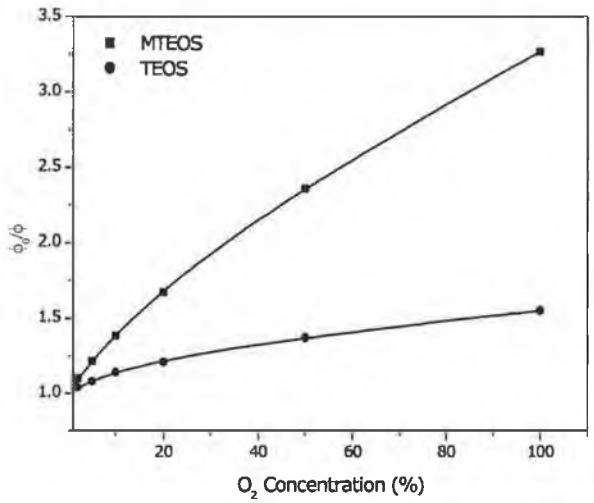

Figure 5.1: Quenching data of an inorganic TEOS-xerogel and that of the benchmark MTEOS-xerogel

Figure 5.1 presents the quenching data of an inorganic TEOS-xerogel and that of an ORMOSIL MTEOS-xerogel. The luminophore $[Ru(dpp)_3]^{2+}$ has been immobilised in each xerogel. The data has been fit to the Demas model. As mentioned in Chapter 2, quenching data obtained from a luminophore in a solid matrix often deviates from the linear ideal of the Stern-Volmer model. The two-site Demas model accommodates the curvature toward the positive x-axis, characteristic of a luminophore immobilised in an amorphous solid

matrix, and so is often the best model to describe quenching data from such sensor elements.

Table 5.1 compares the recovered parameters for the data from Figure 5.1, when fit to the Stern-Volmer and the Demas models. As mentioned in Chapter 2, the Stern-Volmer constant K_{SV} is the parameter governing O_2 sensitivity in that model. For the Demas model, the recovered parameters K_{SV1} and K_{SV2} are the quenching constants associated with luminophore sites 1 and 2, respectively. The fraction of the total emission in unquenched conditions, contributed by each site is f_i. In this work, the largest quenching constant is always assigned to K_{SV1}, so care must be taken to note whether this value relates to the largest fraction of the luminophore population.

precursor	Stern-Volmer	
	K_{SV} $[\%\ O_2]^{-1}$	R^2
TEOS	0.006 ± 0.001	0.8935
MTEOS	0.022 ± 0.001	0.9696

precursor	Demas			
	f_1	K_{SV1} $[\%\ O_2]^{-1}$	K_{SV2} $[\%\ O_2]^{-1}$	R^2
TEOS	0.23 ± 0.02	0.078 ± 0.001	0.002 ± 0.000	0.9997
MTEOS	0.66 ± 0.01	0.060 ± 0.002	0.005 ± 0.000	0.9999

Table 5.1: Comparing fit parameters for the Stern-Volmer and Demas models

From Table 5.1, the R^2 value improves from 0.8935 for TEOS and 0.9696 for MTEOS, to greater than 0.99 for each system, when the quenching data is fit with the Demas model, rather than the Stern-Volmer model. Generally, a model that returns an R^2 approaching 1.00 is deemed to suitably describe the experimental data, and so the two-site Demas model is used throughout this work, unless otherwise stated.

In Table 5.1, the majority of the total luminophore population for the TEOS-based sample is described by the discrete K_{SV2} of 0.002 % O_2^{-1}, while the majority of the total luminophore population for the MTEOS-based sam-

ple is described by the discrete K_{SV1} of 0.06 % O_2^{-1} for MTEOS. This variation in sensitivity is clear from the differing slopes of the two plots in Figure 5.1, which illustrates the improvement in O_2 sensitivity that is achieved through the use of an ORMOSIL glass.

As discussed in Chapter 3, ORMOSILs may be employed to provide particular characteristics to a glassy material. ORMOSILs are used in this work to provide desirable features, in addition to enhanced O_2 sensitivity. These features will be presented in this chapter, for example, TFP-TMOS is used as a starting material for a sol-gel glass in order to enhance photostability.

The MTEOS-xerogel is the standard O_2-sensitive film used as a benchmark for this work. The sensitivity of films made with this luminophore/xerogel combination, forms the benchmark to which the new materials used in this project can be compared.

Novel luminophores are also tested by immobilising them in an MTEOS-xerogel. The resulting O_2 sensitivity can then be directly compared to that of $[Ru(dpp)_3]^{2+}$ immobilised in an MTEOS-xerogel.

5.2.2 Optimising O_2 sensitivity via host xerogel modification

The sol-gel route was employed to produce a range of hybrid xerogels using organosilicon precursors of the form $(C_nH_{2n+1}) - Si - (OR)_3$, where n = 1, 2, 3, 8 and R = Et. This series of precursors was selected to explore the possibility of tuning the hydrophobicity and O_2 sensitivity of the resulting sensor glasses. In addition to this group, PhTEOS and the fluorinated precursor TFP-TMOS, were also investigated, to determine the effect of phenyl groups and fluorine, respectively, on O_2 transport in the sensor glasses. The composition of all of these xerogels has been detailed in Chapter 3.

Figure 5.2 shows the quenching data for each of the xerogels in this work. Each plot in this figure represents data obtained from a xerogel produced using a particular precursor solution. The differing slopes clearly indicate that

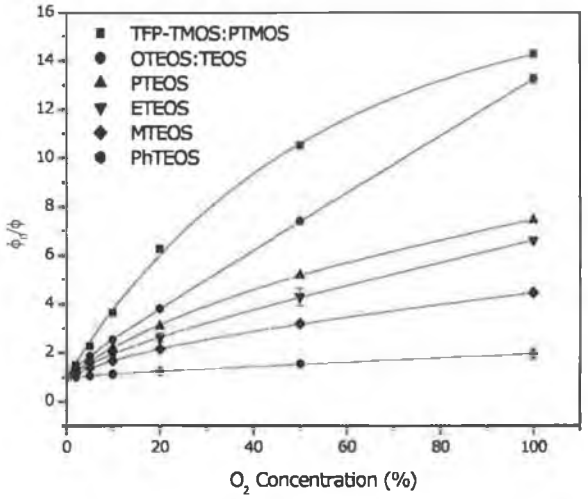

Figure 5.2: Comparison of quenching data for all O_2 sensor layers of relevance to this work. All data has been fit to the Demas model

the choice of precursor solution impacts on the resulting O_2 sensitivity of the glasses. The precursor solutions used in this work, listed in order of increasing O_2 sensitivity are: PhTEOS, MTEOS, ETEOS, PTEOS, OTEOS:TEOS and TFP-TMOS:PTMOS.

Table 5.2 reports on the effect of precursor type on O_2 sensitivity, as quantified by the recovered Demas parameter, K_{SV1}. For each xerogel in the table, K_{SV1} accounts for the quenching constant for more than 60 % of the total luminophore population. Additional data for each xerogel is also included, such as diffusion coefficient, D; water contact angle, and the excited-state lifetime, τ_0, of $[Ru(dpp)_3]^{2+}$ immobilised in that xerogel.

All of the O_2 sensor layers reported here are based on diffusional quenching. As such, their O_2 sensitivity depends on the Stern-Volmer constant, which is a function of two parameters, τ_0 and P, from Equation 2.5. The same luminophore is used in each xerogel, and the differing values of τ_0, recorded in Table 5.2, for the luminphore immobilised in each material, vary too little to account completely for the observed changes K_{SV1}. Therefore,

precursor solution	Demas parameters		D [x 10^{-6} $cm^2 s^{-1}$]	Contact Angle [°]	τ [$\pm$ 0.8μs]
	K_{SV1} $[\%O_2]^{-1}$	R^2			
MTEOS	0.060 $\pm$ 0.002	0.9999	9.86	85	4.92
PhTEOS	0.012 $\pm$ 0.002	0.9990	0.03	90	5.81
ETEOS	0.100 $\pm$ 0.015	0.9994	62.1	95	4.91
PTEOS	0.158 $\pm$ 0.010	0.9997	67.3	102	5.11
OTEOS:TEOS	0.160 $\pm$ 0.048	0.9967	80.0	113	5.98
TFP-TMOS:PTMOS	0.323 $\pm$ 0.022	0.9991	–	102	6.03

Table 5.2: Influence of precursor on xerogel properties

the observed variations in O_2 sensitivity must be due, in the most part, to varying contributions to P, the permeability of the xerogel.

From Table 5.2, it can be seen that the increased alkyl chain length corresponds to increased K_{SV}, which indicates an increase in O_2 sensitivity. As the alkyl chain of the organoalkoxide precursor increases in length (from MTEOS, to ETEOS, to PTEOS, to OTEOS), the relative hydrophobicity increases, as indicated by the contact angle. As discussed in Section 3.5, membranes with increased hydrophobicity, exhibit increased O_2 sensitivity.

However, a PhTEOS-xerogel exhibits a similar water contact angle to that of an ETEOS-xerogel, yet its K_{SV} value indicates a reduced O_2 sensitivity, by comparison. This is likely due to the steric effect of the bulky phenyl groups in the material [1]. The steric effect impedes the transport of O_2 molecules within this material, resulting in a value of D which is three orders of magnitude less than that of an ETEOS-xerogel.

A glass produced using a fluorinated precursor, TFP-TMOS, greatly improves the O_2 sensitivity of the resulting sensor layer. The hydrophobicity of the TFP-TMOS:PTMOS-xerogel is similar to that of a PTEOS-xerogel, but the K_{SV1} of this material is observed to be approximately double that of a PTEOS-xerogel. The origin of this increased O_2 permeability is thought to be due to this material's fluorine component. The high electronegativity of fluorine results in good O_2 affinity. This in turn increases the permeability of

the material to O_2, which improves the transport of O_2 through the material and contributes to the K_{SV1} [2, 3]. Unfortunately, due to issues relating to both the high quenching efficiency and the poor surface quality of sensor elements based on TFP-TMOS attempts to quantify the diffusion coefficient have been unsuccessful.

5.2.3 Optimising O_2 sensitivity via luminophore modification

As mentioned in Section 2.4, the O_2 sensitivity of a luminophore/xerogel sensor membrane may be increased by increasing the excited-state lifetime of the luminophore.

This was achieved in this work by replacing the hydrogen atoms in $[Ru(dpp)_3]^{2+}$ with deuterium, a process known as deuteration.

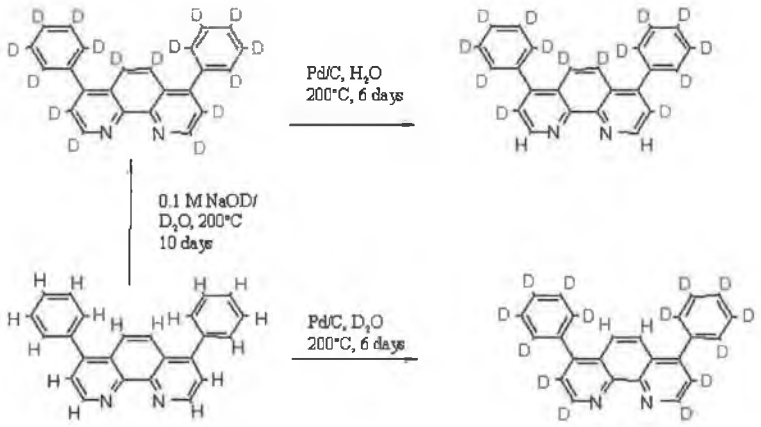

Figure 5.3: The deuteration process

Figure 5.3 (provided by Dr. Adrian Guickian who performed the synthesis of this complex and the standard $[Ru(dpp)_3]^{2+}$ complex used in this work) illustrates the process of deuterating a single diphenyl-phenanthroline (dpp) ligand.

This new luminophore was immobilised in an MTEOS-xerogel. The resulting Stern-Volmer plot is compared to that of the standard $[Ru(dpp)_3]^{2+}$ immobilised in an MTEOS-xerogel in Figure 5.4. The Stern-Volmer model has been used here in order to directly compare the effect of the extended τ_0 on the O_2 sensitivity. This model returns an acceptable $R^2 > 0.96$ and so is deemed appropriate for use in this discussion.

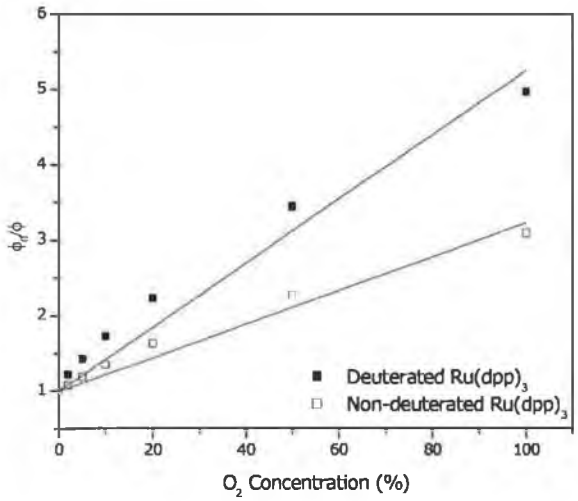

Figure 5.4: Effect of deuteration on O_2 sensitivity

From the plot in Figure 5.4, K_{SV} for the sensor layer containing the deuterated complex is $\sim$ 50 % greater than that of the benchmark sensor layer.

The increase in K_{SV} originates in the extension in τ caused by a reduction in the rate of radiationless decay, k_{nr} (as given in Equation 2.1). The dominant mode of radiationless decay is by loss of energy to the stretch vibration of the C-H bond. Replacing hydrogen atoms with heavier deuterium atoms, reduces the frequency of this vibration. As a result, less energy is required for, what is now, the C-D stretch and so the probability of radiationless decay is reduced. From Equation 2.1, a reduction in the rate of non-radiative decay results in an increase in the observed excited-state lifetime of the complex.

From Table 5.3, the deuteration process leads to an extension of τ_0 by 1 μs, which is an increase of 20 %. Therefore, the observed increase in K_{SV} of 50 % is 30 % larger than expected. However, this discrepancy is thought to lie with the large experimental error in τ_0 of $\pm 0.8 \mu s$. In any case, the O_2 sensitivity has been greatly improved by the deuteration process.

Luminophore	τ_0 [$\pm$ 0.8 μs]	R^2
Non-deuterated *Ru(dpp)*$_3$	4.92	0.9901
Deuterated *Ru(dpp)*$_3$	6.04	0.9987

Table 5.3: Excited-state lifetime data

It should be noted however, that while the observed increase in O_2 sensitivity is encouraging, this complex is costly to produce. This cost has so far proved prohibitive to the commercial use of this luminophore.

It is also worth noting, that the increase in K_{SV} obtained using the deuterated complex is comparable to that obtained by immobilising the non-deuterated *Ru(dpp)*$_3$ in an ETEOS-xerogel. This is a more cost-effective and less complex route to increased O_2 sensitivity.

5.3 Achieving sterilisable sensor membranes

In order to ensure instruments used in bioprocessing are free from live bacteria or other micro-organisms, they are steam sterilised. Steam sterilisation is a process of killing micro-organisms through the application of pressurised steam. Heat damages the micro-organism's essential structures, causing irreversible damage to its metabolic functions. This process eventually kills the organism. Steam sterilisation is performed using an autoclave.

A requirement of sensor membranes developed for use in bioprocessing applications, is that they should be capable of withstanding steam-sterilisation by autoclaving, without requiring additional calibration between autoclave cycles. This section deals with the production of such membranes and

presents results demonstrating their O_2 sensitivity after repeated autoclaving.

The temperature program, subsequent to coating the sol layer onto the substrate, has proved an important step in producing autoclavable films. It was found that the temperature used to cure the films must be higher than that of the intended autoclave process.

The requirement for this work was that the films be capable of withstanding autoclaving at 130 °C and so the films were heat treated at 140 °C as part of the processing procedure. Films cured at temperatures lower than 140 °C showed poor stability after autoclaving, as the microstructure of these films continues to undergo densification when exposed to the relatively higher temperatures within the autoclave. This additional densification of the film's microstructure impacts on the transport of O_2 molecules through the material, which causes a corresponding change in the O_2-sensitive response of the layer. As a result, the sensor layer must be re-calibrated.

Even films cured at 140 °C required additional conditioning, involving exposure to several autoclave cycles, before yielding a stable O_2 response.

MTEOS-based xerogels were tested initially. The resulting O_2 quenching data are presented in Figure 5.5. While the sensor layers were found to retain O_2 sensitivity, the actual O_2 sensitivity changed with subsequent autoclave cycles. This rendered these sensor elements unreliable. This variation in the calibration curve is assumed to be due to the distortion of the matrix due to the capillary action of water in the material's pores during the autoclave process. Cracking and other mechanical defects in porous membranes have been reported by other authors and are thought to be due to an uptake of water during the autoclave process. This water is liquid at 130 °C, due to the high pressure in the autoclave. As the pressure in the autoclave is eventually reduced the boiling point of the water is reduced and it is the subsequent evaporation of that water that is thought to lead to defects in the membrane [4]. The capillary pressure of water in the membrane pores is also thought to contribute to the degradation of the membrane through cracking.

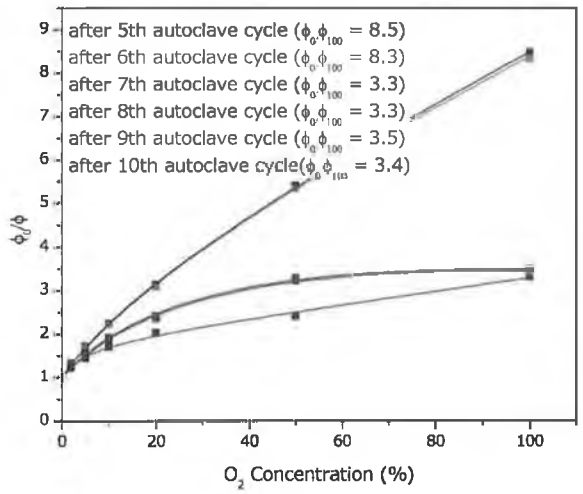

Figure 5.5: O_2 quenching data for an MTEOS-based xerogel obtained following an autoclave cycle. Data taken following the 5th to the 10th autoclave cycles inclusive. Error bars represent standard deviation over 3 samples.

ETEOS-based xerogels were thought to be relatively more flexible than MTEOS-xerogels, due to the increased alkyl chain length of the organosilicon precursor. As such, these membranes should withstand the capillary pressure from the uptake of water during autoclaving, while retaining appropriate rigidity, required to retain a stable O_2 response. As such, ETEOS-based xerogels were examined.

Figure 5.6 shows the quenching data for a typical ETEOS-based xerogels. The film has been cured at 140 °C and then subjected to four autoclave cycles prior to testing. The data in this figure shows the O_2 response of the film, recorded after each autoclave cycle, for six cycles, after the initial conditioning.

In Figure 5.6, the ETEOS-based xerogels are seen to retain their O_2 sensitivity after autoclaving and their O_2 response remains stable, within the standard deviation, at low O_2 concentrations. This level of stability was achieved after six autoclave cycles. These autoclave cycles would have to

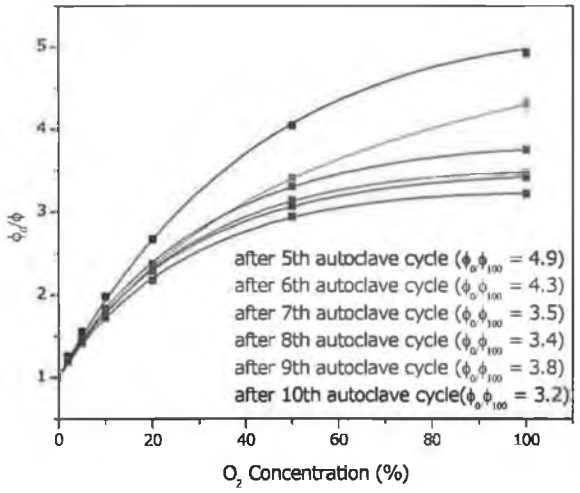

Figure 5.6: O_2 quenching data for an ETEOS-based xerogel obtained following an autoclave cycle. Data taken following the 5th to the 10th autoclave cycles inclusive. Error bars are generally within the space occupied by the data makers and represent standard deviation over 3 samples.

be incorporated into the fabrication process, for the production of steam-sterilisable sensor elements.

5.4 Improving photostability

Any luminophore will experience photodegradation to some extent when exposed to excitation light for a prolonged period [5]. In applications where continuous O_2 monitoring is desirable, the sensor systems in this work may be exposed to an excitation light source for days at a time. Any photodegradation occurring over this time, will alter the luminescence signal and render the sensor platform unreliable.

Figure 5.7 presents the phase angle data for an MTEOS-based film, recorded at ambient O_2 concentration over a 24 hr period. The continual downward phase drift corresponds to an increase in O_2 concentration of $\sim$1 %. This

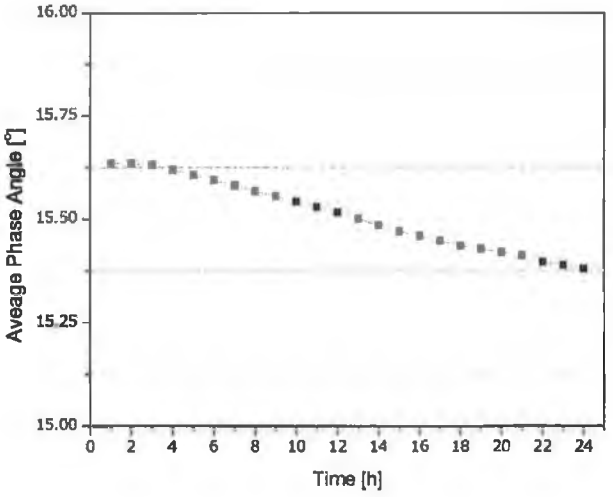

Figure 5.7: Phase angle drift with illumination time for an MTEOS-based film

trend was observed to continue at a similar rate for tests lasting up to and beyond 72 hr. Since no such change in O_2 concentration occurred during the test period, the drift is thought to be a result of photodegradation of the luminophore.

A possible source of this degradation is thought to be due to attack on the luminophore by singlet oxygen, $O_2(^1\Delta_g)$, which is a by-product of dynamic quenching by O_2. The process of dynamic quenching has already been presented in Chapter 2 and is repeated here in the the following expressions [6]:

$$D + h\nu \rightarrow D^* \qquad excitation \tag{5.1}$$

$$D^* + O_2 \xrightarrow{k_q} D + {}^{*1}O_2 \qquad quenching \tag{5.2}$$

Singlet oxygen is an extremely destructive molecule which has been observed to cause ligand dissociation in ruthenium-based luminophores [7].

Another source of the observed phase drift is due to photobleaching of the

luminophore. Klimant et al. have noted that the by-product of photobleaching has an associated lifetime [8]. This implies that the technique of phase fluorometry is not immune to drift caused by photobleaching as previously believed, as the lifetime of the by-product will distort the observed phase data, assumed to result from the O_2-dependent luminophore lifetime.

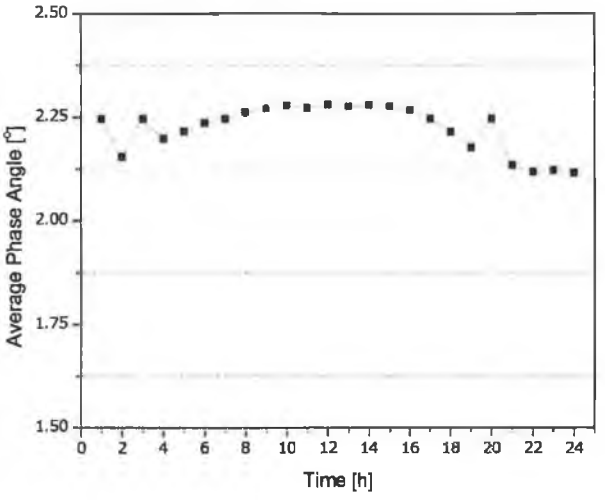

Figure 5.8: Phase angle drift with illumination time for a TFP-TMOS:PTMOS-film

The literature suggests different methods to reduce the effect of photodegradation. Materials containing fluorine have been noted in the literature as being particularly suited for O_2 applications. This is due to the high electronegativity of fluorine which results in relatively good O_2 affinity and good photostability . The improved photostability is attributed to the large bonding energy of a C-F bond, which is 116 kcal mol^{-1}, compared to the 99.5 kcal mol^{-1} bonding energy of a C-H bond [9]. The larger bonding energy greatly improves the ability of materials containing fluoro-groups to withstand photo-oxidation. As such, the fluorinated organosilicon precursor, TFP-TMOS, was used to produce a sensor membrane, as outlined in Chapter 3, with a view to addressing the photostability issue. The resulting

membrane was exposed to the LED excitation for a 24 hr period, as the MTEOS-based xerogel mentioned above.

No notable drift was observed for the phase angle data obtained from the TFP-TMOS:PTMOS-based xerogel, as the plot in Figure 5.8 shows.

Another possible solution is the use of singlet oxygen scavangers. Hartmann et al. suggest DABCO ™ [10]. In the same paper, it is suggested that the choice of host material is of importance, for example, a material in which singlet oxygen has a relatively short lifetime will subsequently experience less damage. However, these approaches have not been examined here.

5.5 Conclusions

This chapter has outlined the properties of an O_2 sensor that are desirable in the applications of interest to this work. These properties include, increased O_2 sensitivity, the capability to withstand autoclaving, and improved photostability.

These properties were achieved through the selection of suitable organosilicon precursors, combinations of precursors and appropriate processing parameters, which have been explained here and have been supported by data where relevant.

A further consideration for sensor membranes is the issue of cross-sensitivity to interferant substances, this issue is addressed separately in Chapter 8.

Bibliography

[1] C. Rottman, G. Grader, and D. Avnir. Polarities of sol-gel-derived ormosils and of their interfaces with solvents. *Chemistry of Materials*, 13:3631–3634, 2001.

[2] Y. Amao, Y. Tabuchi, Y. Yamashita, and K. Kimura. Novel optical oxygen sensing material:metalloporphyrin dispersed in fluorinated poly(aryl ether ketone) films. *European Polymer Journal*, 38:675–681, 2002.

[3] R. M. Bukowski, M. D. Davenport, A. H. Titus, and F. V. Bright. O_2-responsive chemical sensors based on hybrid xerogels that contain fluorinated precursors. *Applied Spectrosopy*, 60(9):951–957, 2005.

[4] H. S. Voraberger, H. Kreimaier, K. Biebernik, and W. Kern. Novel oxygen optrode withstanding autoclavation: technical solutions and performance. *Sensors and Actuators B*, 74:179–185, 2001.

[5] O. S. Wolfbeis. *Fiber optic chemical sensors and biosensors*. Boca Raton : CRC Press, 1991.

[6] J. N. Demas and B. A. DeGraff. Applications of luminescent transition metal complexes to sensor technology and molecular probes. *Journal of Chemical Education*, 74(6):690–695, 1997.

[7] T. P. Roth. *Ruthenium(II) diimine complexes for luminesence-based oxygen sensors and Impedence spectroscopy of nitrogen dioxide-sensitive polymeric membranes*. PhD thesis, Swiss Federal Institue of Technology, 2001.

[8] I. Klimant, F. Ruckruh, G. Liebsch, A. Stangelmayer, and O. S. Wolfbeis. Fast response oxygen micro-optodes based on novel soluble ormosil glasses. *Mikrochimica Acta*, 131:35–46, 1999.

[9] Y. Amao, T. Miyashita, and I. Okura. Novel optical oxygen sensing material: platinum octaethylporphyrin immobilized in a copolymer film of isobutyl methacrylate and tetrafluoropropyl methacrylate. *Reactive and Functional Polymers*, 47:49–54, 2001.

[10] P. Hartmann, M. J. P. Leiner, and P. Kohlbacher. Photobleaching of a ruthenium complex in polymers used for oxygen optodes and its inhibition by singlet oxygen quenchers. *Sensors and Actuators B*, 51:196–202, 1998.

Chapter 6

Phase Fluorometry Study

6.1 Introduction

Phase fluorometry is a useful detection method in luminescence-based sensing. Both the theory behind this technique and the experimental implementation have been discussed in Chapters 2 and 4, respectively. Its advantages over time-domain techniques include the possibility to use low-cost, readily available, discrete opto-electronic components, such as LEDs and photodiodes. By facilitating the use of such components, phase fluorometry makes possible the design of miniaturised sensor platforms, which are necessary for portable sensors but also suited to commercialisation and mass-production. Additionally, phase fluorometry avoids time consuming data analysis synonymous with traditional time-domain techniques, since it is relatively easy to monitor changes in phase angle. As discussed previously, phase fluorometry data is, theoretically, immune to the artifacts that plague intensity-domain data, such as detector drift or fluctuations in excitation signal.

Despite these advantages, certain issues must be addressed when implementing a phase fluorometric scheme. This chapter will highlight the care required to successfully execute phase fluorometry in practice. For instance, optical filter choice is of great importance since any excitation light reaching the detector will combine with the sample's emission to distort the phase

angle data. Selection of modulation frequency is another important consideration, since the sensor platform's response to the analyte varies with modulation frequency.

An anomaly with the phase data which was obtained during a long-term stability study instigated an investigation in to the implementation of the phase fluorometric technique. That investigation is the focus of this chapter.

6.2 Initial observations

Stern-Volmer data have already been presented for OTEOS:TEOS films in Chapter 5. Phase fluorometry measurements, as part of a long-term stability study for these films are presented in Figure 6.1. In this figure, the quantity ϕ_0/ϕ_{100} is seen to fluctuate. This implies that the response of OTEOS:TEOS-membranes varies with time and is not stable.

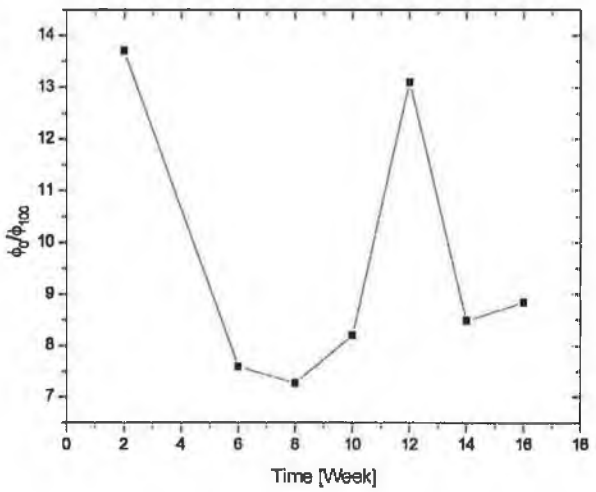

Figure 6.1: Apparent long-term stability issue associated with OTEOS:TEOS membranes

Initially, it was thought that the changes in sensitivity were due to ma-

trix evolution, that somehow the matrix microstructure was changing with time. Fourier transform infrared (FTIR) spectroscopy was used to investigate whether this was the case. For consistency the ratio of the Si-O-Si peaks to Si-OH peaks, for the same OTEOS:TEOS film, was monitored over several months. The data is presented in Table 6.1. These measurements indicated small variations in the matrix structure. However, these small changes did not cause any observable effect in either intensity or direct lifetime measurements, as explained in the following section.

Week	Ratio (Si-O-Si peak: Si-OH peak)
1	2.24
3	2.29
4	2.06
8	1.95
10	2.08
12	2.46

Table 6.1: FTIR data monitoring the ratio of the Si-O-Si and Si-OH peaks, in order to observe small changes in the microstructure of OTEOS:TEOS samples

6.3 Comparing frequency, intensity and time domain data

To confirm that there was an issue with the implementation of the phase fluorometric approach, the frequency-domain data was compared to that obtained in the intensity- and time-domain.

The intensity data, obtained from OTEOS:TEOS samples, is presented in the Stern-Volmer plot (black line), in Figure 6.2. From this data, it is clear that the the intensity data does not coincide with the phase data (green line).

Initially, this discrepancy was thought to be a consequence of static quenching occurring in addition to dynamic quenching. Static quenching refers to

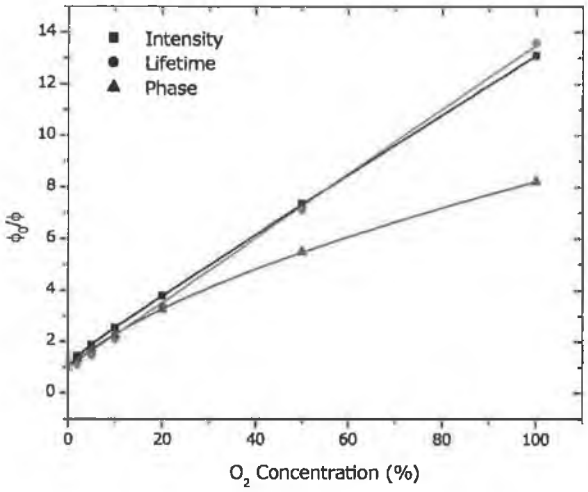

Figure 6.2: Comparison of intensity, lifetime and phase Stern-Volmer plots

the situation where an O_2 molecule forms a ground state complex by combining with an excited $[Ru(dpp)_3]^{2+}$ molecule. This complex returns to ground state without the emission of a photon.

Since the $[Ru(dpp)_3]^{2+}$ molecule is no longer in the excited state the observed luminescence intensity is decreased. As the lifetime of the complex remains unchanged, static quenching is not detected by phase fluorometry or direct lifetime measurements. Therefore, static quenching was thought to be contributing to the quenching process, but that this contribution was not detected via phase measurements. This suggestion was rejected following lifetime measurements.

The lifetime data, shown in Figure 6.2 (red line), is coincident with the intensity data. Static quenching is not detectable by lifetime measurements. Since the lifetime data matches the intensity data, static quenching cannot be occurring in these samples and cannot be responsible for the difference observed between the phase and intensity data.

As further confirmation that the quenching process did not include static

mechanisms, the intensity plot in Figure 6.2 is found to be essentially linear, yielding $R^2 = 0.9987$ when fit to the single-site Stern-Volmer model, given by Equation 2.4. In a case where both static and dynamic quenching occur, the Stern-Volmer tends to deviate from linearity and curve upwards toward the positive $y - axis$ [1]. This is clearly not the case here and so the origins of the discrepancy must lie elsewhere.

The phase data changed virtually each time a reading was taken. A study was carried out to determine whether the intensity and lifetime data changed after the initial reading. Figure 6.3 displays the results of this study. For the study, intensity (black lines), direct lifetime (red lines)and phase (green lines) measurements were taken a week after the films were fabricated (Week 1) and these measurements were repeated the following week (Week 2).

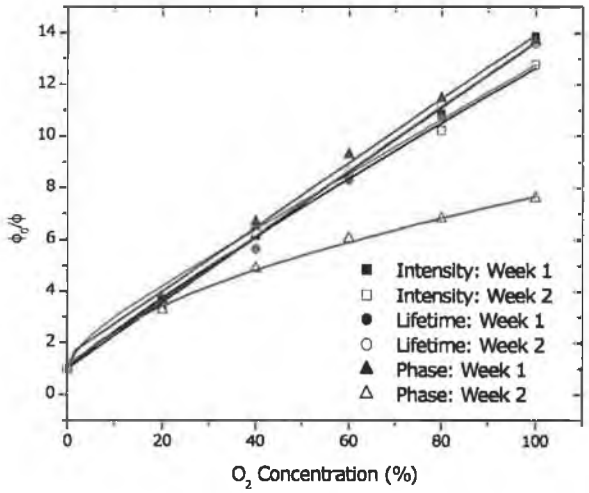

Figure 6.3: Comparison of stability study using three measurement techniques: intensity, lifetime and phase angle

In Figure 6.3, the slope of the phase Stern-Volmer plot was found to vary with time after fabrication, while the Stern-Volmer plots obtained from intensity or direct lifetime measurements did not.

This data, coupled with the FTIR study, which indicated minimal if any

variations in sample microstructure, showed that the phase data is obscured in some fashion, which alluded to a problem with the instrumental implementation of the phase fluorometric technique rather than with the actual samples.

6.4 Filter Study

Having established that the origins of the observed effect did not lie with the sensor film, but with implementation of the phase fluorometric technique, an overhaul of the implementation was prompted. This began with an inspection of the emission filters used at the detector.

Figure 6.4 presents Stern-Volmer plots obtained from intensity and phase data of an MTEOS-sample, the benchmark material in this work. In Figure 6.4(a) the emission filter is a LEE135 and in Figure 6.4(b) the emission filter is a LEE027. A blue Schott BG12 excitation filter was used for all data. The intensity data yields a steeper Stern-Volmer plot than that of the phase data when the LEE135 filter is used. However, the intensity data coincides with the phase data when the LEE027 filter is used.

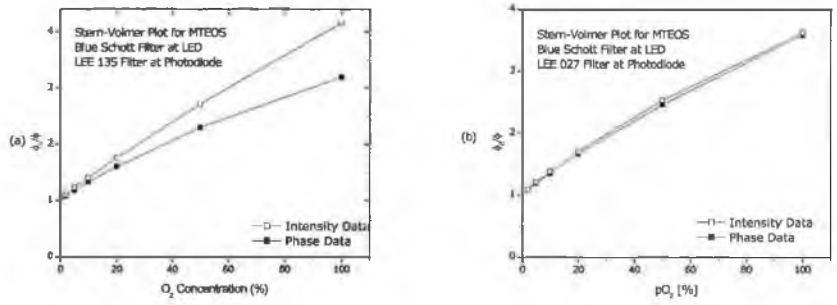

Figure 6.4: Stern-Volmer plots obtained from intensity and phase data using a LEE135 emission filter (a); and a LEE027 emission filter (b). A blue Schott BG12 excitation filter was used for all data

The difference in the transmission spectra of the two LEE filters is presented in Figure 6.5. From this figure, the LEE135 (left panel) will transmit

light at wavelengths above approximately 560 nm, while the LEE027 (right panel) will only transmit above 600 nm. The tail of the LED emission over laps with the transmission of the LEE135 and so this part of the excitation light will reach the detector. The excitation light that is transmitted by the emission filter adds, by phasor addition, to the signal from the sample, as illustrated in Figure 6.6. In this figure, the sample signal is represented by the red arrow and the excitation component that reaches the detector is represented by the blue arrow.

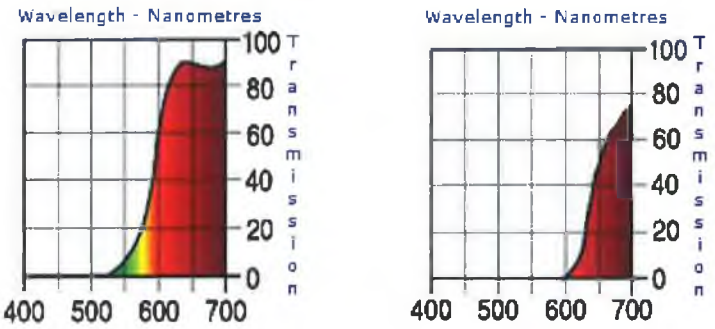

Figure 6.5: Transmission of LEE135 emission filter (left panel); and a LEE027 emission filter (right panel). Obtained from http://www.leefilters.com

The net result of the phasor addition of the sample signal with the blue light component is that the phase angle observed is lower than that of the sample signal. Also, since this component is excitation light and not the phase shifted signal, it behaves as an intensity signal. Therefore, the resulting data is prone to the same issues as reported for intensity-based data, such as fluctuations due to sample positioning and changes in excitation signal. It is this component that is thought to be responsible for the observed phase fluctuations, such as those presented in Figure 6.1.

A more in-depth filter study was pursued by others in this laboratory [2] and so the details of that study are not presented here. The optimum filter combination resulting from that study employs a blue interference filter to eliminate most of the tail of the LED signal that tends to longer wavelengths,

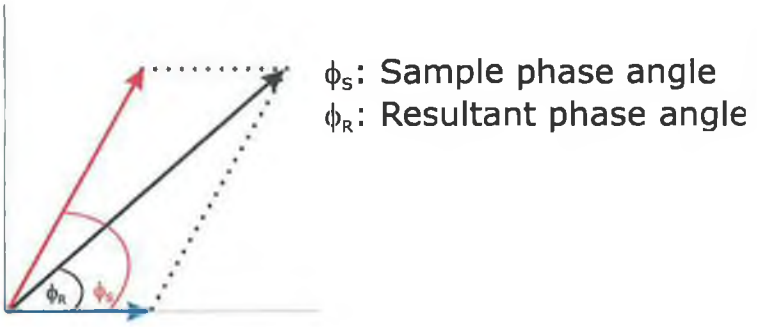

Figure 6.6: Representation of phasor addition. Sample signal (red arrow) adds by phasor addition to the excitation light that reaches the detector (blue arrow). The resultant (black line) yields a lower phase angle (ϕ_R) that the true phase angle of the sample signal (ϕ_S)

and a red dichroic emission filter which has a similar transmission spectrum to the LEE027 filter in Figure 6.5 (right panel). This combination has been adopted for the remainder of this work.

It should be noted that while this filter combination has been determined as the optimum combination for this work, it is not assumed to be a universal solution. In fact, the choice of filter combination has been found to be a function of the desired sensor platform configuration and the application requirements [2]. As such, the filter solution reported here may not be suited to other sensor platforms.

It is worth mentioning that a move away from the use of filters is possible. Maruyama et al. have reported a filter-less luminescence detection technique employing a CMOS detector [3]. While their implementation is intensity-based, a phase-based version would also be possible following the same principles.

6.5 The Influence of Modulation Frequency

Having determined the optimum filter combination the choice of modulation frequency is the next parameter to consider. The influence of modulation fre-

quency on the observed Stern-Volmer plot can be seen in Figure 6.7. Clearly, the choice of modulation frequency has an impact on the slope of the Stern-Volmer plot obtained from a sample, which is a measure of the observed sensitivity of a film. This implies that the modulation frequency can be used to tune the film sensitivity and accordingly, care must be taken when selecting the operating modulation frequency.

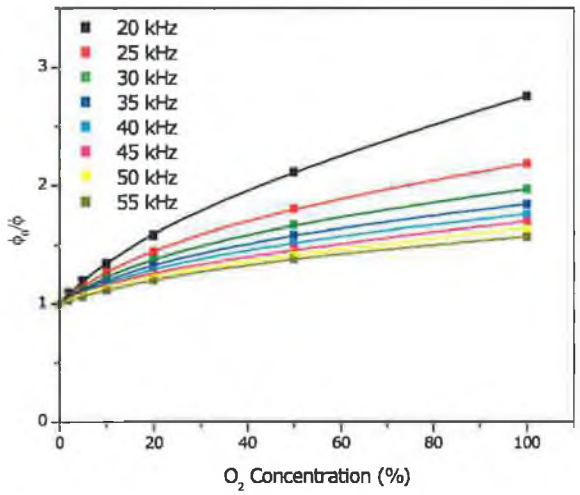

Figure 6.7: Influence of modulation frequency on Stern-Volmer plot

When implementing the phase fluorometry technique the modulation frequency of the excitation light source should, ideally, be matched to the lifetime of the luminophore via Equation 2.12. This match is based on the assumption that the lifetime of the luminophore is single exponential.

As discussed earlier, the observed lifetime for a luminophore population immobilised in a glassy material may tend to be multi-exponential. Additionally, the lifetime of a luminophore can also differ depending on the type of sol-gel matrix it is immobilised in.

Each of these conditions are observed for the samples in this work, since single-exponential lifetimes are observed in the absence of O_2 (see Chapter

5). Also, the luminophore employed is $[Ru(dpp)_3]^{2+}$, which is relatively independent of its environment, returning similar lifetimes in each material examined in this work (see Chapter 5).

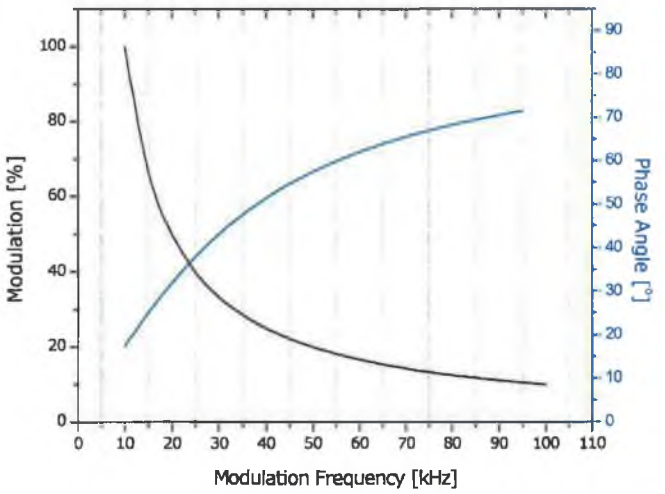

Figure 6.8: Theoretical plots of the variation in modulation and phase angle with modulation frequency. An excited-state lifetime of 5 μs is assumed

When selecting a modulation frequency, the optimum frequency is defined, as above, as that which satisfies Equation 2.12, however there is usually a range of suitable frequencies. The useful frequencies are those for which the phase is frequency dependent [1]. Traditionally, this can be determined by plotting the dependence of either the demodulation factor or the phase angle as a function of the modulation frequency. A theoretical plot of modulation and phase angle for a system exhibiting a lifetime of 5 μs is given in Figure 6.8. A lifetime of 5 μs was chosen for this theoretical plot as that is comparable to the lifetime of $[Ru(dpp)_3]^{2+}$ in each of the materials used in this work, as reported in Chapter 5.

For the frequency range examined in Figure 6.8, the modulation is seen to decrease from 100 to 10 % with increasing modulation frequency. This reduction in modulation results from the excited-state lifetime which causes

a delay in the emission and reduces the peak-to-peak amplitude of the modulated emission signal. The phase angle is seen to increase from 15 to 70 °, for the same frequency range. Both the modulation and phase angle plots undergo the greatest change in the frequency interval from 10 to 50 kHz. The rate of change of the modulation and phase angle, tends to decrease with frequencies above this range.

However, the data in Figure 6.8 are simply theoretical. In operation, the data do not always conform to this ideal, on account of factors such as excitation light reaching the detector (as discussed earlier). In addition, the signal-to-noise ratio decreases as the modulation frequency increases and so for practical applications the selection of an optimum modulation frequency must account for this. Figure 6.9, presents the experimental modulation and phase angle data obtained for an MTEOS-based sample. The data in this figure are intended to highlight the discrepancy between the theoretical and experimental modulation and phase data. The data in Figure 6.9(a) have been obtained using the optimum filter combination. Neither the modulation or the phase data achieve the maximum range of values predicted by the theoretical plots in Figure 6.8. The reason for this discrepancy is thought to be that, in spite of good choice of filters, excitation light is still reaching the detector electronics where it adds to the sample signal (as discussed in the previous section). To confirm this, the data in Figure 6.9(b) has been obtained with no excitation filter. In this case, further excitation light is available to reach the detector, as a result the discrepancy between the obtained data and the theory is greater still.

In practical terms, it can prove difficult to completely eliminate the portion of the excitation light that reaches the detector. Therefore, it must be accepted that the phase data alone (at least in the context of the implementation in this work) cannot be used to recover the luminophore lifetime on account of the additional component resulting from the excitation light. Despite this, phase fluorometry data may be used to successfully interpret O_2 concentration as a function of quenching. For sensing applications based on phase data, the issue of selecting an optimum modulation frequency still ex-

ists since it has been shown that the theoretical means of satisfying Equation 2.12, is not completely satisfactory since it does not account for the problem of phasor addition of the excitation light.

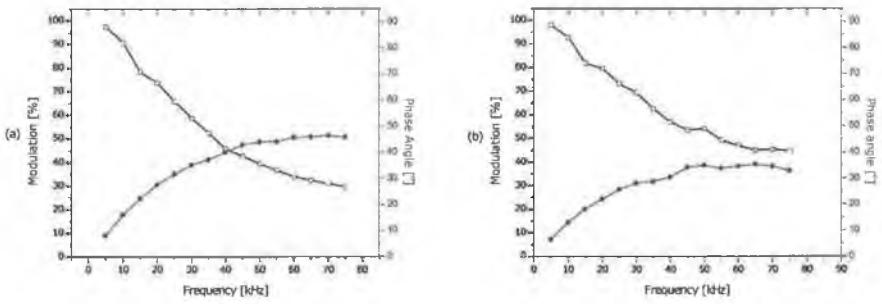

Figure 6.9: Modulation and phase angle as a function of modulation frequency for an MTEOS-sample taken (a) with optimum filter combination (b) with no excitation filter

To address this issue, an alternative approach to determine the useful range of frequency is employed in this work. In this approach, the change in the dynamic range of a sample over a range of frequencies is recorded. From these results, the optimum modulation frequency range is that which yields the appropriate dynamic range. This technique has been employed in a similar manner by other authors in this laboratory [4]. The dynamic range is defined here as the change in phase angle as the environment is switched from N_2 to O_2. This is quantified as:

$$\Delta\phi = \phi_0 - \phi_{100} \tag{6.1}$$

The dependence of the quantity $\Delta\phi$ on modulation frequency is plotted in Figure 6.10. The data in Figure 6.10 were obtained from MTEOS- and OTEOS:TEOS-samples. For each sample, $\Delta\phi$ is observed to increase with modulation frequency and then reaches a plateau. This indicates that the dynamic range of each of the sensor materials increases with modulation frequency up to a point, after which no significant change is observed.

The MTEOS- and OTEOS:TEOS-samples differ considerably in terms of

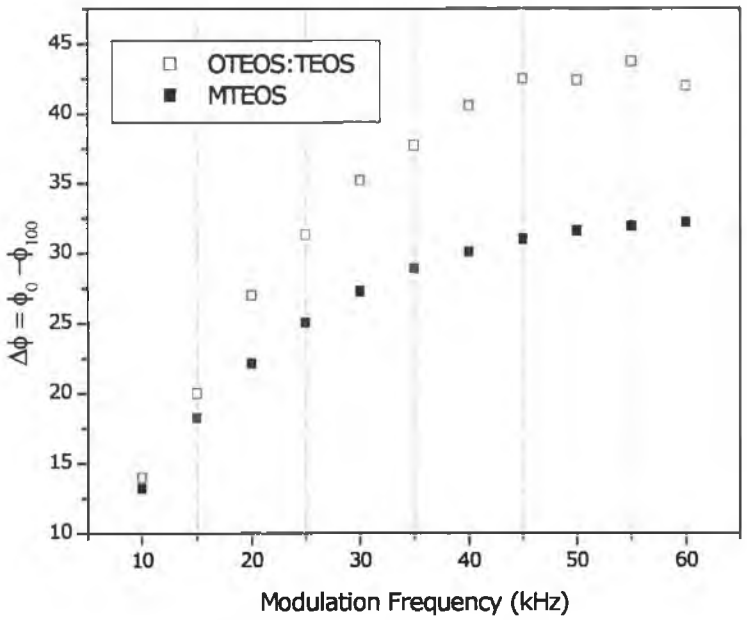

Figure 6.10: Dynamic range, of MTEOS and OTEOS:TEOS samples, as a function of modulation frequency

the sensitivity of their respective O_2 response (see K_{SV} data in Chapter 5). This difference in sensitivity is manifested in Figure 6.10 by the difference in magnitude of $\Delta\phi$ recorded for each sample. For OTEOS:TEOS-samples, $\Delta\phi$ is always greater than that for MTEOS-samples. However, the plots for each sample plateau at approximately the same frequency, $\sim$ 45 kHz. This is as expected considering that the dependence of phase angle on modulation frequency is governed by the excited-state lifetime as in Equation 2.11. Since the lifetime of the luminophore $[Ru(dpp)_3]^{2+}$ should be similar in each of the materials, it follows that the dependence of ϕ, and subsequently the dependence of $\Delta\phi$, is similar for each of the materials.

From Figure 6.10, the optimum modulation frequency for MTEOS- and OTEOS:TEOS-samples is in the 30 - 40 kHz range. This coincides with Equation 2.12 which relates the lifetime to the modulation frequency which yields the maximum phase shift. This relation predicts a modulation frequency of

32 kHz for a lifetime of 5 μs, as exhibited by $[Ru(dpp)_3]^{2+}$.

In the samples examined here, the theoretically predicted value of the optimum modulation frequency compares well with the experimentally recovered values. However, this is not always the case and as a sensor platform is reconfigured for a miniaturised or specialised application, care must be taken to note any time lag or alteration in the signal-to-noise induced by the use of different electronic components or emission filters. Such artifacts may require the reselection of optimum modulation frequency.

Even in the case of the samples examined in this work, where the theoretically predicted value of the optimum frequency coincides with the range of frequencies which yielded the maximum phase shift, the issue of decreasing signal-to-noise for increasing frequencies must still be addressed. When this was investigated, slightly lower frequencies than the 30 - 40 kHz range were found to yield a sufficient phase shift while retaining an acceptable signal-to-noise. As such, the optimum frequency for the experiments in this work was $\sim$ 20 kHz.

Referring back to the OTEOS:TEOS data presented in Figure 6.1, it is important to note that the concentration of the ruthenium-complex in these films is more than 7 times lower than that in the other films presented here. This accounts for the fact that the so-called unstable behaviour shown in Figure 6.1 was not observed for the other films. The relatively low luminescence intensity from the OTEOS:TEOS-film was comparable to the random intensity changes which occurred due to the leakage of excitation light as the film was continuously inserted and removed from the flow cell. In the earlier part of this work, looking at films produced with the higher luminophore concentration, the effect of the excitation light leakage on the sensor response was not obvious. Hence, it was somewhat fortuitous that an investigation into the apparent unstable Stern-Volmer behaviour of OTEOS:TEOS-films led to the conclusion that the choice of filter and, ideally, complete exclusion of excitation light from the detector is crucial for optimum implementation of phase fluorometry.

6.6 Summary and Conclusions

The issues observed for data obtained via phase fluorometry have been presented. The fluctuating signal, first thought to be a function of the luminophore or host material, was found to be an issue with the implementation of the phase fluorometry technique. The choice of filter system has been shown to be of utmost importance in designing a phase fluorometry system. Having selected the optimum filter combination, selection of the optimum modulation frequency range for a particular material is the next criterion to consider. The modulation frequency used to drive the excitation LED has been shown to have a significant effect on the signal observed from a given film.

This chapter has shown that the implementation of phase fluorometry in practice is non-trivial. Care must be taken to ensure excitation light does not reach the detector. This has been achieved here through considered choice of filters. The lifetime of the luminophore must be known and should influence the choice of modulation frequency.

While the initial design of a phase fluorometric system has been shown to require considerable consideration, the technique remains attractive as it has been implemented here with relatively low-cost, readily available opto-electronic components.

Bibliography

[1] J. R. Lakowicz. *Principles of fluorescence spectroscopy.* Kluwer Academic/ Plenum Publishers, New York, 2nd edition, 1999.

[2] Ongoing PhD research project by J. Moore MSc.

[3] Y. Maruyamaa, K. Sawada, H. Takao, and M. Ishida. The fabrication of filter-less fluorescence detection sensor array using CMOS image sensor technique. *Sensors and Actuators A*, 128(1):66–70, 2006.

[4] G. O'Keeffe, B. D. MacCraith, A. K. McEvoy, C. M. McDonagh, and J. F. McGilp. Development of a led-based phase fluorimetric oxygen sensor using evanescent wave excitation of a sol-gel immobilized dye. *Sensors and Actuators B*, 29:226–230, 1995.

Chapter 7

Porosity Study

7.1 Motivation: Correlation of diffusion coefficient with O_2 sensitivity

The study of the O_2 sensitivity of ORMOSIL-based xerogels reported in Chapter 5, indicated that the O_2 sensitivity, quantified by K_{SV}, varies with precursor. This is clear from Figure 5.2, which compares the respective Stern-Volmer plots of a selection of sol-gel-derived sensor layers, fabricated from various organosilicon precursors.

The sensing mechanism at the core of this work is based on dynamic quenching. For dynamic quenching to occur, molecular contact of the analyte and indicator compound must be achieved during the excited-state lifetime of the indicator. For the sensor layers described here, this requires that O_2 molecules must enter the pores of the sol-gel material and collide with the $[Ru(dpp)_3]^{2+}$ molecules encapsulated there. As such, K_{SV} is governed by the quenching process which is dependent on the value of the luminophore excited-state lifetime, and the O_2 permeability of the sol-gel-based material. The excited-state lifetime does not vary significantly for each precursor, as shown in Chapter 5. Therefore, the observed variation in K_{SV} must lie with the respective permeability of the materials. More specifically, variations

in K_{SV} must be due to the diffusion coefficient changing from material to material, as mentioned in Chapter 5.

The origins of the diffusion coefficient are outlined in Chapter 3. It was shown in Equations 3.6 and 3.7 that the diffusion coefficient is proportional to the average pore radius, R_h, of a material, all other factors remaining constant. The average pore radius was also highlighted as being proportional to the total volume porosity, V_p, in Equation 3.8.

A study was undertaken to determine porosity information of the xerogels and to confirm the contribution of porosity to O_2 sensitivity as defined by Equations 3.6 and 3.7.

Ellipsometric porosimetry is used here to obtain porosity information about the ORMOSIL-xerogels by monitoring the refractive index of the membranes during the uptake of an adsorbent into the pores of the material, as described in Chapter 4. Porosity data is recovered from the refractive index data in this work by two techniques: (1) obtaining adsorption isotherms with a view to establishing the pore size distribution (PSD) of the films, and (2) applying the Lorentz-Lorenz equation, which provides volume porosity, V_p.

The results are presented in terms of the precursor, either TEOS, MTEOS or ETEOS, and also in terms of R-value. The V_p data will be shown to correlate with diffusion coefficient data in Chapter 5, which explains the contribution to K_{SV}. In addition, the MTEOS results are compared to the results of a study undertaken by a commercial laboratory.

7.2 Pore size distribution (PSD) obtained via ellipsometric porosimetry

The pore size distribution (PSD) of a porous layer yields significant information relating to the permeability of the membrane and the transport of molecules into the material [1].

The PSD is calculated here using the water desorption isotherm for TEOS

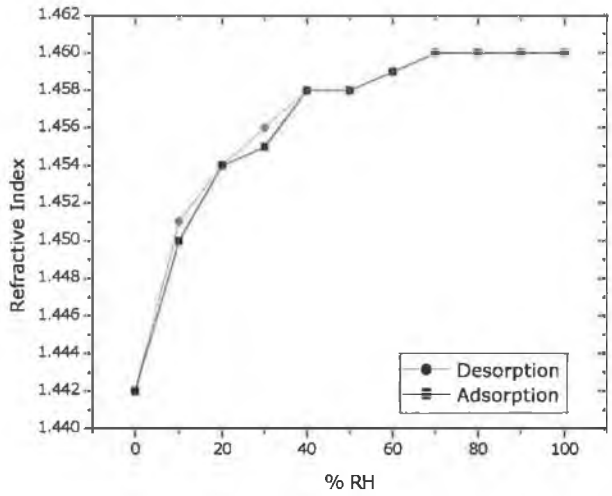

Figure 7.1: Isotherms obtained for TEOS-R=6-based xerogel with water as the adsorbent

R=6, TEOS R=4 and TEOS R=2 samples. An example of the adsorption/desorption isotherm for TEOS R=6 is given in Figure 7.1. This isotherm shows little hysteresis and is typical of the samples examined in this work. By applying Equation 4.5, the change in the adsorptive volume may be recovered from the change in refractive index of the sample at each interval of relative humidity. From the resulting data the PSD may be obtained.

However, the isotherms obtained in this work, including the isotherm presented in Figure 7.1, are all Type I isotherms, as defined by the BET classification. Type 1 isotherms indicate a predominantly microporous structure, where all available pores are filled at the lower relative humidities. As such, little porosity information may be derived by obtaining the PSD from the isotherms of these materials [2]. For completeness, the PSD for TEOS R=6, TEOS R=4 and TEOS R=2 samples are presented in Figure 7.2.

The PSD for each of the samples are very similar. This is not unexpected since the isotherms imply the majority of the pores are likely to be micropores (of radius < 2 nm) and therefore not represented using this technique.

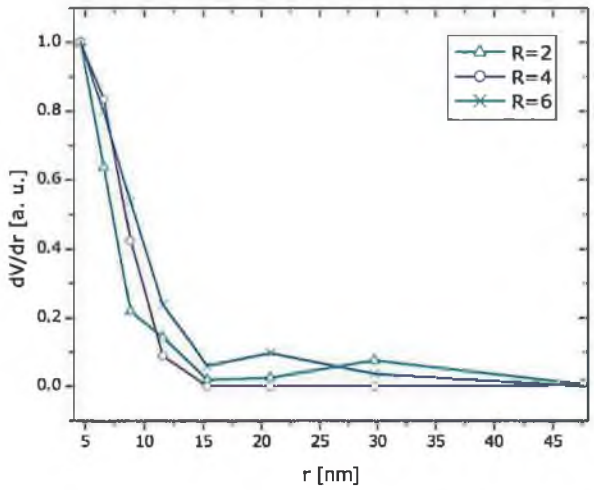

Figure 7.2: PSD obtained for TEOS R=2, R=4 and R=6 samples with water as the adsorbent

In addition, there is a possible source of error in the data due to difficulties repeating the humidity conditions for each samples. Such difficulties would lead to inaccurate RH values recorded for the desorption branch of an isotherm, which distort the PSD. This issue is found to be a drawback of this approach to obtaining porosity information. While the high vacuum pumping technique, would afford greater accuracy, the process is time consuming and the equipment is costly.

In order to obtain more useful porosity information the volume porosity is calculated with adsorbents of different critical diameter. This work is presented in the following section.

7.3 V_p obtained via Lorentz-Lorenz equation

The technique of ellipsometric porosity is used here to obtain volume porosity, V_p, data for the sol-gel-based layers. In this technique, changes in refractive

index are recorded as a function of relative humidity, while water vapour is introduced to the sample cell. Organic solvents are also employed as adsorbents. Increases in refractive index can be used to determine the volume of adsorbent occupying the pores. When the refractive index reaches a maximum, the sample is assumed to be saturated, with all open pores filled with the adsorbent. At this point, the volume of adsorbent occupying the pores is assumed to be equal to the total volume of the pores, V_p.

By using adsorbents of varying critical diameter further porosity information can be determined. In this way, the V_p of pores of a particular diameter can be probed. This procedure is known as molecular probing.

The experimental procedure adopted here is detailed in Chapter 4. Briefly, the sample is contained in a flow cell and flushed with N_2 in order to obtain the initial refractive index. The adsorbent is introduced to the cell by adding wash bottles containing the liquid adsorbent to the N_2 pipeline. A constant flow rate is maintained using mass flow controllers. This method uses organic solvents that are readily volatile at ambient conditions and so avoids the cost and safety issues associated with vacuum systems.

For experiments using water as adsorbent, the refractive index of the sample at a relative humidity of 0 %, denoted as n_{dry}, and that at a relative humidity of $\sim$ 100 %, denoted as n_{wet}, was determined for each sample examined. This data was applied to Equation 4.4, the Lorentz-Lorenz relation, in order to recover the V_p value for the material. The value of the refractive index of the solid skeleton, $n_{skeletal}$, is obtained simultaneously with V_p, and is used here as a measure of the quality of the data. It will be shown that the data obtained in this manner compare well to results obtained using the vacuum pumping technique. The data obtained are discussed below.

7.3.1 V_p obtained using water as the adsorbent

The samples examined here are TEOS R=2, TEOS R=4, and TEOS R=6, in addition to ORMOSIL samples derived from MTEOS and ETEOS, respectively. The data obtained for n_{dry} and n_{wet} and the calculated values of V_p

and $n_{skeletal}$ are presented in Table 7.1 for each material.

precursor	n_{dry} [±0.001]	n_{wet} [±0.001]	V_p [± 0.5%]	$n_{skeletal}$ [±0.002]
TEOS R=6	1.442	1.460	4.5	1.466
TEOS R=4	1.427	1.449	5.6	1.456
TEOS R=2	1.411	1.444	8.4	1.455
MTEOS	1.424	1.433	2.3	1.435
ETEOS	1.433	1.433	0.0	1.433

Table 7.1: Volume porosity and skeletal RI values calculated from Lorentz-Lorenz equation with water as adsorbent

From the literature, the refractive index of densified TEOS is 1.460. The calculated value of $n_{skeletal}$ for each of the three TEOS-derived samples, presented in Table 7.1, are in reasonable agreement with the literature value.

The V_p obtained for the TEOS samples is seen to increase with decreasing R-value. This is as expected due to the decrease in gel time that occurs with increasing water content (this is true for the range of R-values examined here, although additional effects occur at larger R-values [3]). This implies that for a given gel time, the sol produced with the lowest R-values will have reached the lowest level of cross-linking, resulting in the largest volume porosity, relative to the sols produced with higher R-values.

From Table 7.1, the V_p obtained for the TEOS R=4-sample is greater than that of either the MTEOS- or ETEOS-sample of the same R-value. This contradicts the O_2 sensitivity data for these layers presented in Chapter 5, where K_{SV} for a TEOS-xerogel is measured to be an order of magnitude lower than that of an MTEOS-xerogel and two orders of magnitude lower than K_{SV} of an ETEOS-xerogel. This discrepancy arises due to the hydrophobicity of the MTEOS- and the ETEOS-material. Each is relatively hydrophobic compared to a TEOS-surface and so water molecules do not readily adsorb into the pores of these materials. Since virtually none of the pores fill with this adsorbent, little or no change in refractive index is observed and so only a minimal V_p is recorded. Hence, water is not an effective adsorbent for porosity determination of ORMOSILs.

This situation highlights the consideration required when choosing a solvent for molecular probe experiments. The experiment was repeated for TEOS R=4-, MTEOS- and ETEOS-samples, this time using less polar ethanol as the adsorbent.

7.3.2 V_p obtained using ethanol as the adsorbent

precursor	n_{dry} [±0.001]	n_{wet} [±0.001]	V_p [± 0.5%]	$n_{skeletal}$ [±0.002]
TEOS R=4	1.427	1.442	3.6	1.445
MTEOS	1.424	1.448	5.7	1.454
ETEOS	1.433	1.491	13.5	1.513

Table 7.2: Volume porosity and skeletal RI values calculated from Lorentz-Lorenz equation with ethanol as adsorbent

Table 7.2, presents the V_p data obtained using ethanol as the adsorbent. The V_p for the TEOS-sample is reduced, compared to that obtained when using water as the adsorbent, suggesting the pores of this material do not accommodate ethanol molecules as well as they do water molecules. This is expected as the critical diameter of ethanol is larger than that of water. The critical diameter of each of the adsorbents is listed in Table 7.4, where that of water and ethanol is 0.28 nm and 0.44 nm, respectively. Since, not all the pores can be filled the assumption for the Lorentz-Lorenz relation is not satisfied and this explains the low value of 1.445 returned for $n_{skeletal}$.

The V_p obtained for the MTEOS-sample, increases from 2.3 to 5.7 % when the adsorbent is changed from water to ethanol. This supports the earlier conclusion that using highly polar water to probe a hydrophobic material, yields falsely low V_p values, as the water will not be adsorbed into the pores.

This is also the case for the ETEOS-sample, where the V_p increases from 0 to 13.5 % when the adsorbent is changed from water to ethanol. In Table 7.2, the V_p for the MTEOS-sample is much lower than that obtained for the ETEOS-sample. This implies that a greater percentage of pores of

the ETEOS-sample are capable of accommodating the critical diameter, 0.44 nm, of the ethanol molecule. This result supports the findings in Chapter 8, which suggested that ethanol molecules can penetrate the pores of an ETEOS-xerogel but not those of an MTEOS-xerogel. This relatively larger pore capacity of an ETEOS-xerogel is suggested as the explanation for luminophore leaching from an ETEOS-xerogel when contained in a vial of ethanol, whereas an MTEOS-xerogel, under the same conditions, shows no leaching. This is discussed in Chapter 8.

Overall, these experiments show the V_p of MTEOS-xerogel to be 7.8 percentage points less than that of an ETEOS-xerogel. This is found to contribute to the difference in K_{SV} of these two materials, which is discussed in Section 7.4.2.

7.3.3 V_p obtained using toluene as the adsorbent

precursor	n_{dry} [±0.001]	n_{wet} [±0.001]	V_p [± 0.4%]	$n_{skeletal}$ [±0.001]
TEOS R=4	1.427	1.435	1.4	1.434
MTEOS	1.424	1.438	2.5	1.437
ETEOS	1.433	1.475	7.4	1.473

Table 7.3: Volume porosity and skeletal RI values calculated from Lorentz-Lorenz equation with toluene as adsorbent

Adsorbent	Critical Diameter [nm]	n_{ads}	Dielectric Constant
Water H_2O	0.28	1.333	88.0
Ethanol CH_3CH_2OH	0.44	1.360	24.3
Toluene $C_6H_5CH_3$	0.67	1.496	2.0 - 2.4

Table 7.4: Adsorbent information

The experiment was repeated using toluene as the adsorbent. The critical diameter of a toluene molecule, at 0.67 nm, is significantly larger than that

of either water or toluene. The larger molecule will not be accommodated by pores of smaller pore diameter. Since fewer pores can be filled, the volume of adsorbent will be reduced, indicating a lower V_p. This is the case for each sample. The TEOS-based sample returned a V_p of 1.4 %. Its overall V_p, that obtained using water, is 5.6 %. This implies that about 75 % of the porosity of the TEOS-based sample consists of pores of diameter less than 0.67 nm (or of radius less than 0.34 nm).

For the MTEOS-based sample, the V_p obtained using toluene is 2.5 %, indicating that 56 % of its overall porosity is accounted for by pores of diameter less than 0.67 nm (or of radius less than 0.34 nm). For the ETEOS-based sample, the V_p obtained using toluene is 7.4 %, indicating that 45 % of its overall porosity is accounted for by pores of diameter less than 0.67 nm (or of radius less than 0.34 nm). These variations in V_p with the critical diameter of the adsorbent molecule are plotted in Figure 7.3. The results show that the ETEOS-based sample has the largest pore volume of the three xerogel types examined.

7.4 Summary

7.4.1 Influence of R-value on xerogel V_p

TEOS-xerogels have been produced using sols of varying R-value. The motivation was to determine how the R-value influences the V_p of the resulting material. The R-values used for this comparison were 2, 4 and 6.

From the data in Table 7.1, V_p is seen to decrease, from 8.4 to 5.3 to 4.5 %, as R-value is increased from 2 to 4 to 6, respectively. The adsorbent used to determine this V_p data is water. All pores are assumed to be filled with water as the $n_{skeletal}$ values are comparable with the literature value of 1.460 for the refractive index of densified silica.

The reduction in V_p with the increased water content occurring for increased R-values is expected, as explained earlier. This result is also consis-

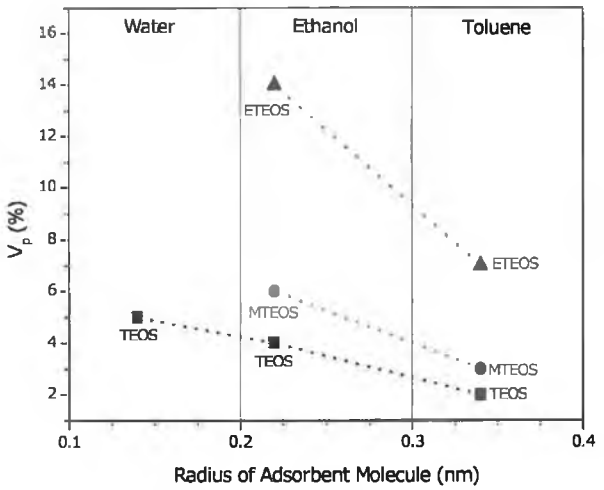

Figure 7.3: Variation of V_p with critical diameter of adsorbent molecule. V_p data obtained for MTEOS- and ETEOS-based samples using water as adsorbent have been omitted as this data is believed to be obscured by the hydrophobicity of these materials

tent with the lower K_{SV} data measured for films with larger R-value determined in other work carried out in this laboratory [4].

7.4.2 Influence of organosilicate precursor on xerogel volume porosity

The V_p of MTEOS- and ETEOS-based ORMOSIL films, is investigated to correlate this data with the O_2 sensitivity and diffusion data in Chapter 5.

Initially, the V_p data obtained for MTEOS- and ETEOS-based xerogels was acquired using water as the adsorbent. This data is presented in Table 7.1, and is misleading since it appears that the V_p of a TEOS-based xerogel is greater than that of either an MTEOS- or ETEOS-based xerogel. This occurs since both MTEOS- and ETEOS-based xerogels are relatively hydrophobic, and so water will not readily adsorb into pores of either material. Since

relatively little water is adsorbed into these materials, compared to that for the TEOS-based xerogel, it appears that these materials have a smaller pore capacity.

A more suitable adsorbent proved to be ethanol. The experiment was repeated using ethanol and more realistic values of V_p were returned for both the MTEOS- and ETEOS-based xerogels. The results are presented in Table 7.2 and they highlight the increase in porosity as the organic group in the material is increased.

In order to gain some information regarding the range of average pore sizes, the experiment was repeated using toluene. The critical diameter of this molecule is $\sim$ 50 % greater than that of ethanol. The V_p values for all samples, obtained using toluene, were reduced. The V_p obtained indicated the portion of the overall volume porosity that was representative of the pores of diameter greater than 0.67 nm, or of radius greater than 0.34 nm. Since the theory in Chapter 3 refers to the pore radius rather than pore diameter, pore radius is the parameter of interest in this discussion.

There is a general correlation with the V_p data and the diffusion coefficient data, given in Table 5.2, for MTEOS- and ETEOS-based samples. However, the porosity data obtained here does not correlate exactly with the diffusion coefficient data. The diffusion coefficient for an ETEOS-sample, D_{ETEOS}, is greater than D_{ETEOS} by a factor of 6.3. If we can assume, for the V_p data that the average pore radius of an ETEOS- and an MTEOS-based xerogel is approximately 0.34 nm and 0.22 nm, respectively, this implies that the square of the average pore radius for an ETEOS-sample, $R^2_{h-ETEOS}$, is 0.116 nm, and $R^2_{h-MTEOS}$ is 0.048 nm. Therefore, $R^2_{h-ETEOS}$ is greater than $R^2_{h-MTEOS}$ by a factor of only 1.6. This also indicates that $R^2_{h-ETEOS}$ and R^2_{hMTEOS} are each greater than R^2_{h-TEOS} by a factor of 5.8 and 1.6, respectively. These relatively increases does not completely account for the observed increase in D obtained for both MTEOS- and ETEOS-based samples, compared to TEOS-samples. However, the values of R^2_h are approximations and so further molecular probing experiments are required to return more accurate and reliable values. In addition, the samples used in the ellipsometry experiments

could not be used for the diffusion coefficient experiments and vice versa, as a result two different sets of samples were required. Therefore, some discrepancy is expected.

7.5 Results of SOPRA's investigation

In order to determine the validity of the experimental approach used in this work for determining porosity information, MTEOS- and ETEOS-based samples were sent for examination by a commercial company. The company, SOPRA [5], conducts porosity investigations using a similar principle to that used in this work, but a high vacuum system and a dry pumping system is used to controlled the adsorptive pressure.

SOPRA's investigation employed toluene as the adsorbent. During the experiment the ETEOS-based sample was damaged and so no porosity data was obtained. Their investigation of the MTEOS-based sample returned values of 1.431 and 1.447 for n_{dry} and n_{wet}, respectively. They used these values to obtain V_p of 2.8 % for the MTEOS-based sample, which is comparable to the value of 2.5 % obtained in this work, for toluene as the adsorbent. The n_{dry} value of 1.431 for the MTEOS-based sample obtained by SOPRA is larger than the value obtained in this work, 1.424. It is difficult to determine the reason for this discrepancy as SOPRA provided no information on their modelling technique. Despite this, it is encouraging that the difference in refractive index, n_{dry} - n_{wet}, is similar for both techniques. This suggests that using a solvent that is suitably volatile at atmospheric pressure removes the need for a costly vacuum system, in porosimetry measurements.

SOPRA also reported n_{dry} for the ETEOS-based sample to be 1.435. This does compare reasonably well with the experimental data in this work, which found n_{dry} for the ETEOS-based samples to be 1.433, however the lack of information on the model used again makes it difficult to comment further on this.

7.6 Conclusions

V_p is seen to increase with decreasing R-value and is also found to increase as the alkyl chain length of the organic group increases from TEOS to MTEOS to ETEOS.

V_p infomation was established by ellipsometric porosimetry at atmospheric pressure. The results were consistent with the predicted behaviour of sol-gel porosity in terms of R-value, for the TEOS-based samples. The V_p data for the TEOS R=4-, MTEOS- and ETEOS-based samples were consistent with the O_2-sensitive data in Chapter 5. There the increase is K_{SV} from TEOS to MTEOS to ETEOS was suggested to be due to a corresponding increase in diffusion coefficient, which in turn was most likely due to increasing porosity.

That the data coincides with theoretically predicted behaviour is encouraging as it lends support for this approach. Further support for the ellipsometric porosimetry technique is that a good agreement was found with the data obtained in a commercial laboratory employing a more sophisticated and expensive high vacuum pumping technique.

Finally, the V_p data confirms that MTEOS-based xerogels exhibit less porosity than ETEOS-based xerogels and this supports the findings in the solvent study in Chapter 8.

In summary, it is clear from the data presented in this chapter and in Chapter 5, that there is general correlation between pore volume, O_2 diffusion coefficient and O_2 sensitivity measured by the K_{SV} parameter, for TEOS-, MTEOS- and ETEOS-based samples. This behaviour, in turn, is consistent with predicted sol-gel microstructure variations as a function of R-value and precursor alkyl-chain length.

Bibliography

[1] Y. Lee, J. Jeong, I. J. Youn, and W. H. Lee. Modified liquid displacement method for determination of pore size distribution in porous membranes. *Journal of Membrane Science*, 130:149–156, 1997.

[2] S. J. Gregg and K. S. W. Sing. *Adsorption, Surface Area and Porosity.* Academic Press, London, 1978.

[3] C. Jeffery Brinker and George W. Scherer. *Sol-Gel Science: The Physics and Chemistry of Sol-Gel Processing.* Academic Press Inc., San Diego, 1990.

[4] P. Bowe. *Characterisation of porosity and sensor response times of sol-gel-derived thin films for oxygen sensor applications.* MSc, Dublin City University, 2002.

[5] SOPRA. *http://www.sopra-sa.com.*

Chapter 8

Effect of Solvent Vapour on O_2 Response

8.1 Introduction

Currently, there is a market for reliable sensors of O_2 for bio-processing applications. Some of the optical sensors discussed in this work are being developed for this market.

An O_2 sensor intended for use in a bio-fermenter must be immune to cross-sensitivity to other analytes in the environment, such as ethanol. In this chapter, the interference of ethanol with the luminescence response signal of the sensor layers, for both gaseous and dissolved O_2 sensing, is investigated. The cross-sensitivity of ORMOSIL-based O_2-sensitive films to other solvents is also highlighted.

Data resulting from attempts to quantify the interference are examined and a possible explanation for the interference mechanism is presented.

8.1.1 Initial observations: Ethanol interference with gaseous O_2 sensing

The quenching data obtained from an MTEOS-xerogel taken with and without an ethanol wash bottle in the gas flow (as outlined in Chapter 4), are shown in Figure 8.1. In this figure, the plot obtained from data taken in the presence of ethanol vapour yields a lower slope than that taken without ethanol. As in earlier chapters, a lower slope indicates that the O_2-sensitivity of the sensor layer has been reduced.

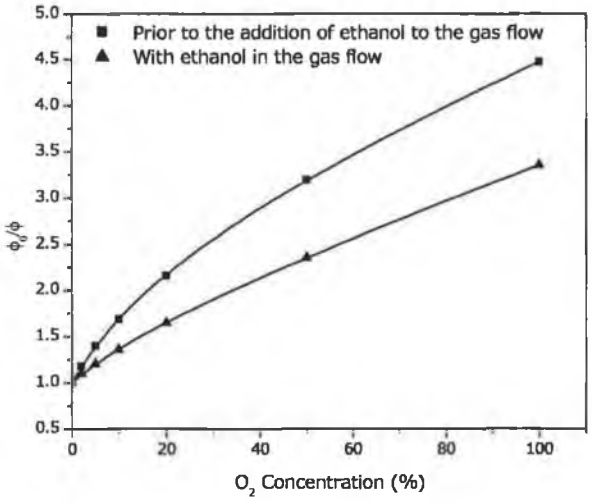

Figure 8.1: Effect of interference from ethanol vapour on an MTEOS-xerogel

The reduced sensitivity observed must be due, in some way, to the presence of ethanol, since all other parameters remain unchanged.

Interference from ethanol vapour in the O_2/N_2 gas mix was observed for all O_2-sensitive xerogel systems in this work. The results for ETEOS- and PTEOS-xerogels are presented in Figures 8.2 and 8.3, respectively.

The Stern-Volmer plot of an ETEOS-xerogel in the absence of ethanol vapour almost overlaps with that in presence of ethanol vapour.

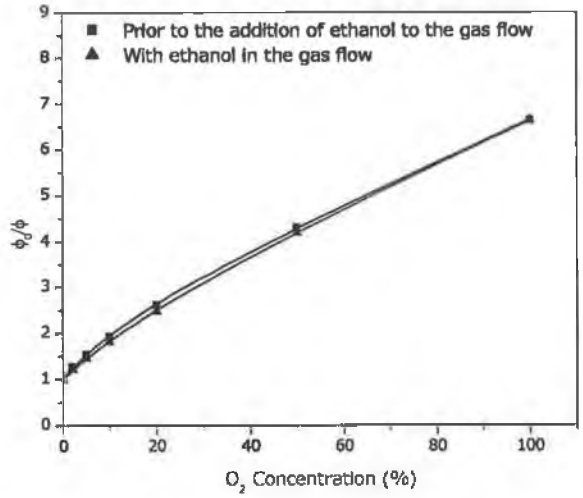

Figure 8.2: Effect of interference from ethanol vapour on an ETEOS-xerogel

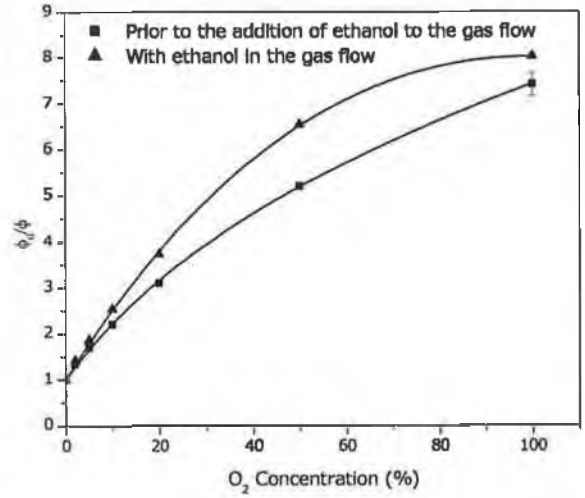

Figure 8.3: Effect of interference from ethanol vapour on an PTEOS-xerogel

The behaviour observed for the quenching data of a PTEOS-xerogel in

the presence of ethanol is counter to that of the MTEOS-xerogel. From Figure 8.3, the slope of the Stern-Volmer plot, for PTEOS-samples, is seen to increase in the presence of ethanol vapour. The curvature of plot, toward the positive x-axis also becomes more pronounced.

These results are explored and an explanation is presented later in this chapter.

8.1.2 Initial observations: Ethanol interference with dissolved O_2 sensing

The interference of ethanol with dissolved O_2 sensing was also observed. Table 8.1 compares the phase angle recorded for an MTEOS-based sensor layer in various quantities of ethanol in deionised water, to those obtained for the same sample in 100% deionised water and in air.

Environment of MTEOS-xerogel	Absolute Phase Angle [°]
Ambient (Air)	21.17
Water	22.23
5% EtOH 95% Water	24.03
25% EtOH 75% Water	24.23
100% EtOH	24.47

Table 8.1: Effect of ethanol on dissolved O_2 sensing

The observed phase angle was seen to increase with increasing ethanol concentration. From Equation 2.11, an increase in phase angle indicates an increase in τ, which indicates a reduction in dynamic quenching and so signifies a reduction in the O_2 concentration. Since no change in O_2 concentration has occurred, the change in signal must be due to some interference with the O_2 sensing mechanism caused by the ethanol, as observed for gaseous measurements above.

8.2 Interference effects of other solvents

The influence of other solvents on the O_2 sensitivity of ORMOSIL-based sensor layers was investigated. The solvents tested were ethanol, hexane and chloroform.

Table 8.2 shows the influence of solvent vapour on K_{SV1} for MTEOS-, ETEOS- and PTEOS-xerogels. Information on the critical diameter of each of the solvents and the O_2 diffusion coefficient, D, of each of the xerogels is also included. The diffusion coefficient data has been included as an indication of the average pore radius of the xerogels. (It was shown in Chapter 3, that the O_2 diffusion coefficient is proportional to the average pore radius, since the O_2 solubility is taken as being constant for the materials examined here.)

Precursor	D [x 10^{-6} cm^2s^{-1}]	Solvent	Critical Diameter [nm]	Δ f	ΔK_{SV}
MTEOS	9.86	Hexane	0.51	-0.04 $\pm$ 0.05	-0.12 $\pm$ 0.03
		Chloroform	0.69	-0.13 $\pm$ 0.07	-0.13 $\pm$ 0.02
		Ethanol	0.44	-0.14 $\pm$ 0.08	-0.16 $\pm$ 0.03
ETEOS	62.1	Hexane	0.51	+0.05 $\pm$ 0.07	+0.02 $\pm$ 0.03
		Chloroform	0.69	+0.15 $\pm$ 0.08	+0.02 $\pm$ 0.03
		Ethanol	0.44	+0.05 $\pm$ 0.08	+0.04 $\pm$ 0.03
PTEOS	67.3	Hexane	0.51	+0.03 $\pm$ 0.03	+0.06 $\pm$ 0.03
		Chloroform	0.69	+0.12 $\pm$ 0.04	+0.07 $\pm$ 0.03
		Ethanol	0.44	+0.07 $\pm$ 0.02	+0.02 $\pm$ 0.02

Table 8.2: Solvent data. In this table, Δ f and ΔK_{SV} refer to the relative change in f and K_{SV}, respectively, observed when each parameter is obtained in the absence and then presence of solvent vapour

From the data in Table 8.2, the nature of the interference appears to be a function of the solubility of $[Ru(dpp)_3]^{2+}$ in the solvent and the relative size of the critical diameter of the interferant molecule to the average pore radius of the xerogel. The implications of these results are discussed in the

following sections with a view to establishing the origins of the interference mechanism.

8.3 Origins of the solvent interference mechanism

8.3.1 The role of the luminophore in the solvent interference mechanism

Some luminophores exhibit variations in their luminescent properties when exposed to solvents. For example, $[Ru(bpy)_3]^{2+}$ has been reported to exhibit a bathochromic shift in its emission spectrum when exposed to methanol and to a lesser extent when exposed to ethanol [1, 2]. Such a change in the emission spectrum of $[Ru(bpy)_3]^{2+}$ would alter the luminescence signal of a sensor platform based on this luminophore in the presence of a suitable solvent.

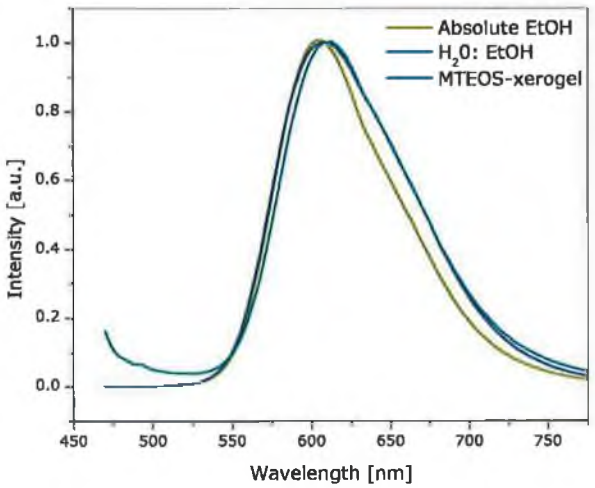

Figure 8.4: Effect of environment on the emission spectra of $[Ru(dpp)_3]^{2+}$

However, as Figure 8.4 shows, the emission spectrum of $[Ru(dpp)_3]^{2+}$ exhibits no such solvent sensitivity, as the excited-state is shielded from the external environment by the phenyl groups [3,4], as discussed earlier in Chapter 2. As such, the interference observed for the O_2-sensitive signal in the presence of solvent vapour is not thought to be due to a solvent dependent change in the intrinsic luminescence properties of the luminophore. Instead, the variation in the luminescence signal is thought to originate with the interaction at the xerogel/solvent interface.

8.3.2 The role of the xerogel material in the solvent interference mechanism

The role of the xerogel material in the solvent interference mechanism is dealt with here by determining the nature and extent of solvent interference on ORMOSIL-based sensor layers (i) by investigating whether the issue is related to the sol-gel-derived materials (ii) by analysing the recovered parameters of the two-site Demas model, presented in Table 8.2, and (iii) by conducting a leaching study.

Investigating polymer-based materials

Before any investigation was initiated, an $[Ru(dpp)_3]^{2+}$-doped polymer film was tested for ethanol interference. The polymer selected was polysulfone (PSU). This test was used to determine whether the issue of ethanol interference was exclusive to sol-gel-based materials. Figure 8.5 presents Stern-Volmer plots obtained from the PSU-membrane, before and during exposure to ethanol vapour.

Since the data in Figure 8.5 is comparable to the data in Figure 8.1, obtained for an MTEOS-xerogel, it was concluded that the issue of ethanol interference is not specific to the sol-gel material.

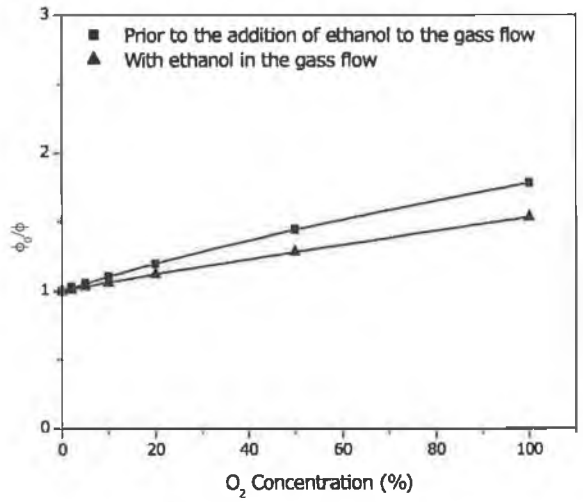

Figure 8.5: Effect of interference from ethanol vapour on an PSU-membrane

Analysing the Demas parameters

The two-site Demas model has been applied to the O_2 quenching data for MTEOS-, ETEOS- and PTEOS-xerogels before, during and after exposure to solvent vapour.

From the Demas model (discussed in Chapter 2), the quantity f_1 refers to the fraction of the luminophore population most accessible to O_2 and K_{SV1} refers to the Stern-Volmer constant of that fraction.

Figure 8.6 presents the effect of the presence of ethanol on the recovered quenching parameters, f_1, K_{SV1} and K_{SV2} of the Demas model, for MTEOS-xerogels. The data for K_{SV1} and K_{SV2} is presented in Figure 8.6(a) and the data for f_1 is given in 8.6(b). From Figure 8.6(b), it was observed that upon exposure to ethanol vapour, f_1 decreases. When the solvent vapour is removed, f_1 then returns to its original value.

In Figure 8.6(a), K_{SV1} is observed to behave in the same way, showing a reduction in the extent of quenching in the presence of solvent vapour, then returning to within the standard deviation of its original value when

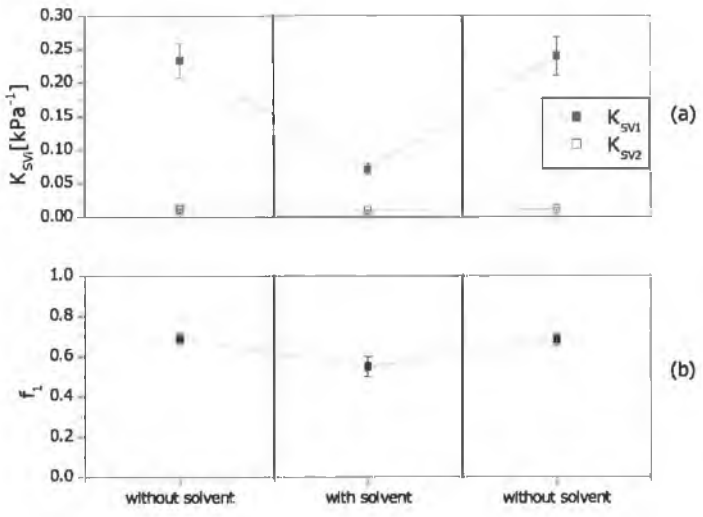

Figure 8.6: The variation of the recovered Demas quenching parameters, before, during and after exposure to ethanol vapour: for an MTEOS-xerogel

the solvent is removed from the gas flow path. Similar trends were observed for the presence of chloroform and hexane, respectively, where f_1 and K_{SV1} decrease in the presence of each of these solvents and then return to the original value when the solvent vapour is removed.

PTEOS-xerogels were seen to behave in the opposite manner, as Figure 8.7 shows. That is, in the presence of solvent vapour, f_1 is seen to increase in Figure 8.7(b). K_{SV1} is also seen to increase in the presence of solvent vapour in Figure 8.7(a), indicating an increase in the extent of quenching.

When the solvent vapour is removed f_1 returns to within the standard deviation of its original value. However, K_{SV1} is found to remain at a marginally increased value, 17 % greater than its original value. This behaviour is observed for both ethanol and chloroform vapour. Although, when the chloroform vapour is removed from the gas flow, K_{SV1} does return to within the standard deviation of its original value. However, the important parameter to note is f_1, which increases in the presence of both ethanol and chloroform vapour, and returns to its original value when the vapour source is removed.

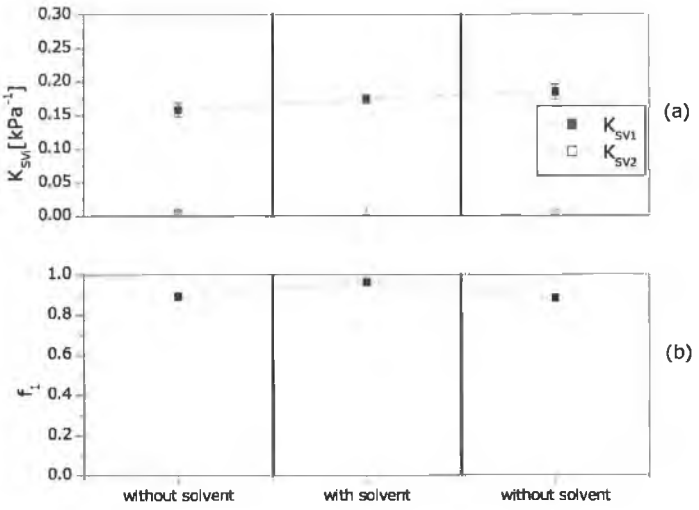

Figure 8.7: The variation of the recovered Demas quenching parameters, before, during and after exposure to ethanol vapour: for an PTEOS-xerogel

When hexane vapour is introduced to the gas flow, f_1 does not change. That is, the portion of the population accessible to O_2 remains unchanged. While f_1 remains virtually constant, K_{SV1} is observed to increase in the presence of hexane vapour and then returns to within standard deviation of its original value when the vapour is removed.

ETEOS-xerogels were observed to behave neither exactly as MTEOS- or PTEOS-xerogels but somewhere in the interim. Figure 8.8 presents the recovered Demas parameters for quenching data obtained from an ETEOS-xerogel in the presence and absence of ethanol vapour. Similar data has been obtained for chloroform vapour. In Figure 8.8(b), f_1 is seen to increase in the presence of ethanol vapour, within the large standard deviation. K_{SV1} is seen to decrease in the presence of ethanol vapour, in Figure 8.8(a). This implies that while the fraction of the luminophore population accessible to O_2, f_1, has increased (see progression from the left to the center panel in 8.8(b)), the K_{SV1} of that fraction decreases (see progression from the left to the center panel in 8.8(a)). These effects counteract each other and this may explain

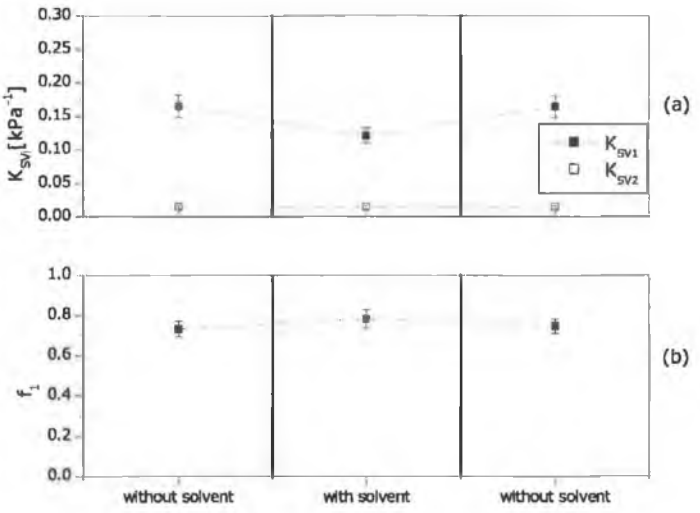

Figure 8.8: The variation of the recovered Demas quenching parameters, before, during and after exposure to ethanol vapour: for an ETEOS-xerogel

why there is little variation on the Demas plots of the quenching data of the ETEOS-xerogel in Figure 8.2.

Chloroform elicits a similar response from the Demas parameters of an ETEOS-xerogel, however the increase in f_1 is more pronounced, exceeding the standard deviation and consequently, the Stern-Volmer plot of the quenching data increases significantly.

When hexane vapour is introduced to the gas flow the behaviour of the recovered Demas parameters is slightly different. In the presence of hexane vapour, both f_1 and K_{SV1} remain unchanged.

These results indicate that the effect of solvent vapour on the quenching data differs, depending on the material. The differences in behaviour can be explained by comparing the average pore radius of the xerogels and the critical diameter of the solvent molecules.

For MTEOS-xerogels, which exhibit a relatively small diffusion coefficient and therefore presumably are of a smaller average pore radius, K_{SV} is ob-

served to decrease in the presence of solvent vapour. This is similar to the effect previously observed for humidity interference [5]. Figure 8.9 illustrates the effect of humidity on the O_2 sensitivity of an MTEOS-xerogel

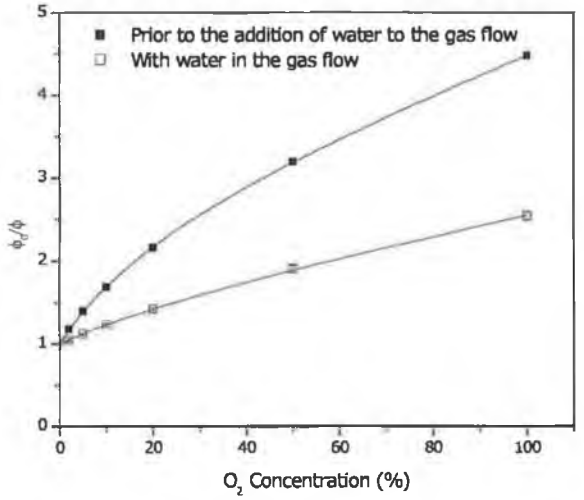

Figure 8.9: Effect of interference from humidity on the quenching data for an MTEOS-xerogel

In the presence of water vapour the O_2 sensitivity of the membrane is reduced. It is proposed that this is due to the water molecules blocking the pores of the sol-gel matrix. By blocking the matrix pores, the water molecules form a barrier to O_2 molecules, inhibiting the transport of the O_2 molecules through the matrix to the sensing luminophore. It is thought that the ethanol interference, observed for MTEOS-xerogels, occurs by the same mechanism, where the ethanol molecules prevent the O_2 molecules entering the sol-gel matrix. Since less O_2 is reaching the luminophore, less quenching can occur and so the slope of the resulting Demas plot will decrease. With time the ethanol vapour leaves the matrix, the pores are unblocked and O_2 transport to the luminophore continues unimpeded. Eventually, the film recovers its original sensitivity and O_2 sensing takes place as before. The recovery of the O_2-sensitive response for films exposed to ethanol vapour has been in shown

in Figure 8.1.

The solvent vapour interference causes a different effect on the response of PTEOS-based sensor xerogels. These xerogels have a larger average pore radius than MTEOS-xerogels, as suggested by an increased diffusion coefficient, and these xerogels exhibit an increase in f_1 in the presence of solvent vapour, where the solvent is a good solvent for $[Ru(dpp)_3]^{2+}$ (such as ethanol or cholorform). The increased pore radius suggests that solvent molecules may penetrate into the pores and interact with the luminophore. In cases where the luminophore is soluble in the solvent, it is possible that the luminophore may be leached from the pore. Such leaching would increase the accessibility of the luminophore to O_2 molecules, and so would explain the observed increased in f_1.

ETEOS-xerogels exhibit a slightly smaller diffusion coefficient than PTEOS-xerogels and therefore are of slightly smaller average pore radius. The interface mechanism for these membranes appears to be similar to that of PTEOS-xerogels but less pronounced. Presumably, the average pore size being similar to, but smaller than that of PTEOS-xerogels, reduces the extent of luminophore leaching.

To summerise, f_1 is observed to increase, for ETEOS- and PTEOS-xerogels in the presence of ethanol and chloroform vaopur. The luminophore $[Ru(dpp)_3]^{2+}$ is soluble in both ethanol and chloroform. The increase in f_1 , implies that the accessibility of O_2 molecules to the luminophore is increased. A possible explanation for the increased accessibly, is that leaching is occurring for those xerogels of sufficiently large average pore radius.

Leaching study

The study of the Demas model, applied to O_2 quenching data for ORMOSIL xerogels in the presence of solvent vapour appears to indicate that luminophore leaching is occurring for xerogels of sufficiently large pore size. As such, a leaching study was implemented.

$[Ru(dpp)_3]^{2+}$-doped MTEOS-, ETEOS- and PTEOS-xerogels were immersed

in vials of the liquids to be tested, for intervals of 5 min, 1 hr and 24 hr. The liquids to be tested were, deionised water, ethanol, hexane and choloroform. The emission spectrum of the liquid in each vial was examined after each interval in a fluorometer for traces of $[Ru(dpp)_3]^{2+}$. The presence of $[Ru(dpp)_3]^{2+}$ in the liquid was identified by an emission peak around 610 nm.

Sample	Dielectric Constant	Good solvent for $[Ru(dpp)_3]^{2+}$
Hexane	2.0	No
Chloroform	5.0	Yes
Ethanol	24.0	Yes
Deionised Water	80.0	No

Table 8.3: Polarity of liquids examined in leaching study and the solubility of $[Ru(dpp)_3]^{2+}$ in each liquid.

Data relating to the polarity and solubility of $[Ru(dpp)_3]^{2+}$ in each of the liquids tested is presented in Table 8.3. The polarity of the liquids used, ranges from the relatively non-polar hexane and chloroform, with dielectric constants of 2.0 and 5.0, respectively, through to ethanol, which exhibits an intermediate dielectric constants of 24.0, to water with a dielectric constant of 80.0. Of the liquids tested, $[Ru(dpp)_3]^{2+}$ is only soluble in chloroform and ethanol.

The luminescence traces detected for the vials of hexane and ethanol, are presented in Figures 8.10 and 8.11, respectively. The MTEOS-xerogels exhibited no leaching of luminophore molecules in deionised water, ethanol, chloroform or hexane, even after 24 hr. ETEOS- and PTEOS-xerogels exhibited no leaching of luminophore molecules in deionised water or hexane, however leaching was observed for xerogels immersed in ethanol and also for xerogels immersed in chloroform. Leaching was observed for the ETEOS- and PTEOS-xerogels after just 1 min immersed in either ethanol or chloroform.

These results indicate: (1) that the polarity of the interferant molecules does not appear to have any bearing on the extent of leaching (2) that xerogel average pore size determines the permeability of solvent molecules into the

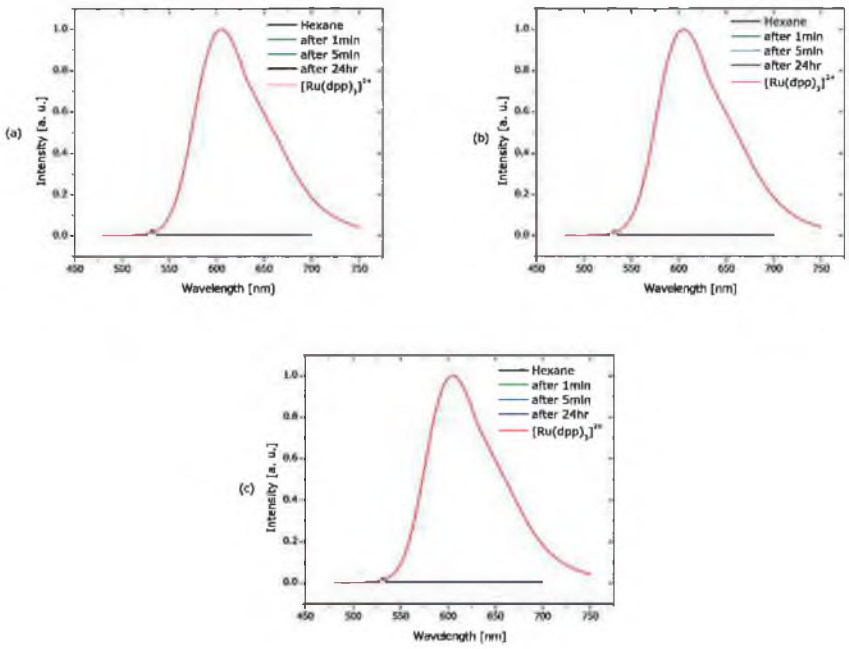

Figure 8.10: Luminescence detected from vial of hexane, which contained an $[Ru(dpp)_3]^{2+}$-doped MTEOS-xerogel (top left panel); ETEOS-xerogel (top right panel) and PTEOS-xerogel (bottom panel)

matrix, and (3) that leaching will occur when the solvent, is both, of suitable critical diameter to permeate the xerogel, and one in which the immobilised luminophore is soluble.

The results from the leaching study imply that the average pore size of an MTEOS-xerogel is smaller than that of either ETEOS- or PTEOS-xerogels. The diffusion coefficient data reported in Chapter 5 and results of the V_p study, in Chapter 7 support this.

8.4 Summary

All films produced as part of this work have been found to be subject to cross-sensitivity from solvent vapour.

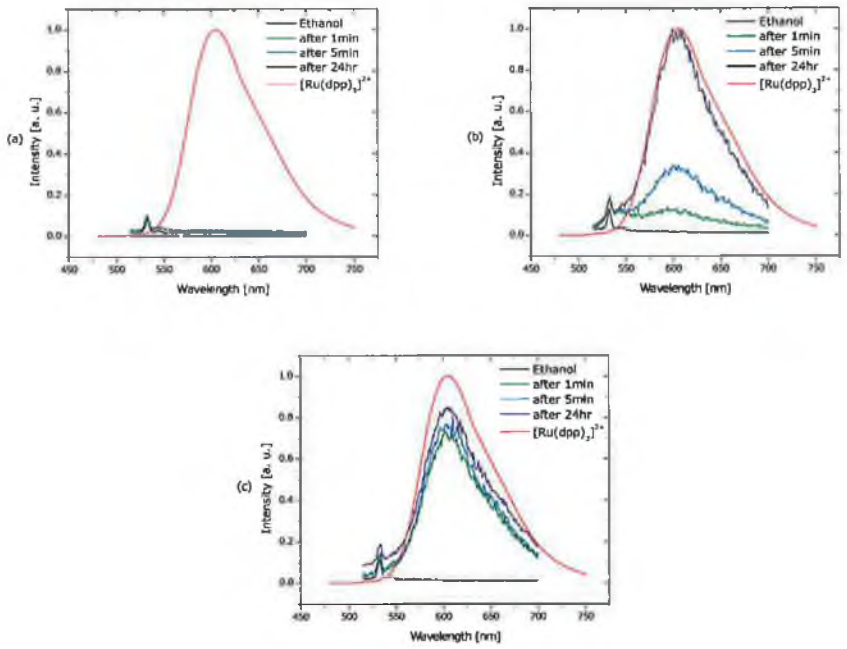

Figure 8.11: Luminescence detected from vial of ethanol, which contained an $[Ru(dpp)_3]^{2+}$-doped MTEOS-xerogel (top left panel); ETEOS-xerogel (top right panel) and PTEOS-xerogel (bottom panel)

The nature of the interference appears to differ depending on ORMOSIL type and the extent of the interference appears to depend on the interfering solvent.

The interference of each solvent with the quenching behaviour of each xerogel sensor layer, was quantified by examining the recovered parameters of the two-site Demas model. This approach indicated a decrease in f_1 for MTEOS-films, but an increase in f_1 for the ETEOS- and PTEOS-layers in the presence of ethanol vapour. The increase in f_1 implied the possibility that luminophore leaching was occurring for PTEOS-, and to a lesser extent ETEOS-xerogels. As such, a leaching study was prompted, which verified these findings.

Demas and Bacon reported previously that an O_2 sensor, based on

$[Ru(dpp)_3]^{2+}$ immobilised in silicone rubber, will not be impaired by solvent molecules that do not penetrate the membrane [6]. This appears to be the case for those xerogel membranes produced in this work, such as MTEOS-xerogels, whose average pore radius is sufficiently small to effectively block the passage of the interferant molecules. In this case, the vapour molecules appear to interfere via the pore-blocking mechanism observed with humidity interference. The interference is manifested in an observed reduction in f_1 for the film in the presence of solvent vapour.

A different situation occurs in the case of xerogel films, such as ETEOS- and PTEOS-xerogels, that exhibit a sufficiently large average pore radius to accommodate the interferant molecules. If the interferant is a good solvent for the luminophore, then the possibility of leaching of the luminophore arises. It is proposed that some leaching occurs, where a portion of the encapsulated luminophore molecules, dissolve in the interferant solvent molecules. This is thought to have the effect of mobilising these luminophore molecules, increasing their accessibility to O_2, and so increasing the observed O_2 sensitivity of the film. This interference is manifested in an observed increase in f_1 for the film in the presence of solvent vapour.

This leaching effect, caused by solvent vapour, is less dramatic than that observed in the leaching study in Section 8.3.2, and so it is thought that for the most part the luminophore molecules are not leached out from the xerogel film completely. This is evidenced by the return of f_1 to its original value when the solvent vapour is removed from the gas flow.

A proposed strategy, to eliminate the leaching issue, is to produce ETEOS- and PTEOS-films with smaller pores, by increasing the R-value during the sol-gel process. In this way, the attractive non-polar properties of the films will be retained but leaching will be minimised and hopefully eliminated. This would leave only one issue to address, that of pore blocking.

From the literature, it appears that the issue of liquids collecting on a film surface may be addressed through particular deposition and curing techniques [7–10]. It is hoped that by further research into the effect of both deposition and curing on surface quality, xerogel surfaces will be produced of suit-

able quality to prevent the possibility of pore-blocking by solvent molecules.

Bibliography

[1] Q. Chang, J.R. Lakowicz, and G. Rao. Fluorescence lifetime-based sensing of methanol. *Analyst,*, 122:173–177, 1997.

[2] P. Hartmann, M.J.P. Leiner, S. Draxler, and M.E. Lippitsch. Specific solvent effects of linear alcohols on the emission spectrum and the excited state decay of tris(2,2'-bipyridyl) ruthenium(ii). *Chemical Physics*, 207:137–146, 1996.

[3] E.R. Carraway and J.N. Demas. Photophysics and oxygen quenching of transition-metal complexes on fumed silica. *Langmuir*, 7:2991–2998, 1991.

[4] E.R. Carraway, J.N. Demas, B.A. DeGraff, and J.R. Bacon. Photophysics and photochemistry of oxygen sensors based on luminescent transition-metal complexes. *Analytical Chemistry*, 63:337–342, 1991.

[5] D. Wencel, C. Higgins, A. Guckian, C. McDonagh, and B.D. MacCraith. Novel hybrid sol-gel materials for smart sensor windows. *Proceedings SPIE, OptoIreland*, 5826:696–705, 2005.

[6] J.R. Bacon and J.N. Demas. Determination of oxygen concentrations by luminescence quenching of a polymer-immobilized transition-metal complex. *Analytical Chemistry*, 59:2780–2785, 1987.

[7] L. Zhu, Y. Feng, X. Ye, and Z. Zhou. Tuning wettability and getting superhydrophobic surface by controlling surface roughness with well-designed microstructures. *Sensors and Actuators A: Physical Selected*

Papers from TRANSDUCERS '05 - The 13th International Conference on Solid-State Sensors, Actuators and Microsystems - Seoul, Korea, 5-9 June 2005, 130-131:595–600, 2006.

[8] S.D. Bhagat, Y. Kim, and Y. Ahn. Room temperature synthesis of water repellent silica coatings by the dip coat technique. *Applied Surface Science*, 253(4):2217–2221, 2006.

[9] P. Fabbri, M. Messori, M. Montecchi, S. Nannarone, L. Pasquali, F. Pilati, C. Tonelli, and M. Toselli. Perfluoropolyether-based organicinorganic hybrid coatings. *Polymer*, 47:1055–1062, 2006.

[10] K. Satoh, H. Nakazumi, and M. Morita. Preparation of super-water-repellent fluorinated inorganic-organic coating films on Nylon 66 by the sol-gel method using microphase separation. *Journal of Sol-Gel Science and Technology*, 27:327–332, 2003.

Chapter 9

Printing and Deposition

9.1 Introduction

This chapter presents a review of the deposition techniques employed in this laboratory to produce sensor layers from sol-gel solutions.

The thickness of a sensor layer is an important parameter, since increased thickness increases the diffusion path of the analyte to the sensor chemistry, subsequently increasing the response time of the sensor. In addition, thicker layers may be prone to concentration issues, for example non-uniform distribution of excitation light may arise in a situation where the majority of excitation signal is absorbed by a highly concentrated portion of sample near the source [1]. Such a situation complicates the sensor's calibration function. As such, an attractive deposition technique is one in which processing parameters may be controlled, allowing deposited layers of reproducible thickness to be produced. In addition, the deposited layers should be of uniform thickness across their surface area.

The deposition techniques presented here are characterised by monitoring the reproducibility of the deposited layers in terms of thickness and O_2 sensitivity.

This chapter begins by presenting the laboratory-based deposition techniques of dip-, spin- and stamp-coating. Following this, deposition tech-

niques suited to mass-production, such as pin-, ink-jet- and gravure-printing are discussed, completing this short review.

9.2 Dip-, spin- and stamp-coating

Dip-, spin- and stamp-coating comprise the most common deposition techniques employed in the production of sol-gel layers in this laboratory. These techniques are compared here in terms of reproducibility. Since the deposited layers are intended as sensor elements, the parameters required to be reproducible are layer thickness, and O_2 sensitivity.

The thickness of 5 sample layers deposited with each technique is compared in Table 9.1. The dip-coated layers were formed with a dip-speed of 3 mm/s. The spin-coated layers were deposited at a spin-speed of 3000 rpm. The stamp-coated layers were produced by hand as described in Chapter 4.

Dip-Coated		Spin-Coated		Stamp-Coated	
Sample	Thickness [μm]	Sample	Thickness [μm]	Sample	Thickness [μm]
1	0.43 $\pm$ 0.01	1	0.76 $\pm$ 0.07	1	1.53 $\pm$ 0.31
2	0.43 $\pm$ 0.01	2	0.67 $\pm$ 0.13	2	2.40 $\pm$ 0.25
3	0.45 $\pm$ 0.01	3	0.74 $\pm$ 0.09	3	2.88 $\pm$ 0.15
4	0.45 $\pm$ 0.03	4	0.73 $\pm$ 0.10	4	2.04 $\pm$ 0.66
5	0.45 $\pm$ 0.02	5	0.63 $\pm$ 0.09	5	2.24 $\pm$ 1.25
Mean	0.44 $\pm$ 0.01	Mean	0.71 $\pm$ 0.04	Mean	2.22 $\pm$ 0.30

Table 9.1: Comparing thickness and standard deviation data for layers deposited by dip-coating at 3 mm/s, spin-coating at 3000 rpm and stamp-coating.

From Table 9.1, it is clear that dip-coating and spin-coating both produce layers with better thickness reproducibility than stamp-coating. The greatest standard deviation in thickness for dip-coating is $\pm$ 0.03 μm, this represents a percentage error of 7 %. The greatest standard deviation in thickness for spin-thickness, is $\pm$ 0.13 μm, a percentage error of 19 %. By comparison, the lack of reproducibility in the thickness of layers produced by stamp-coating

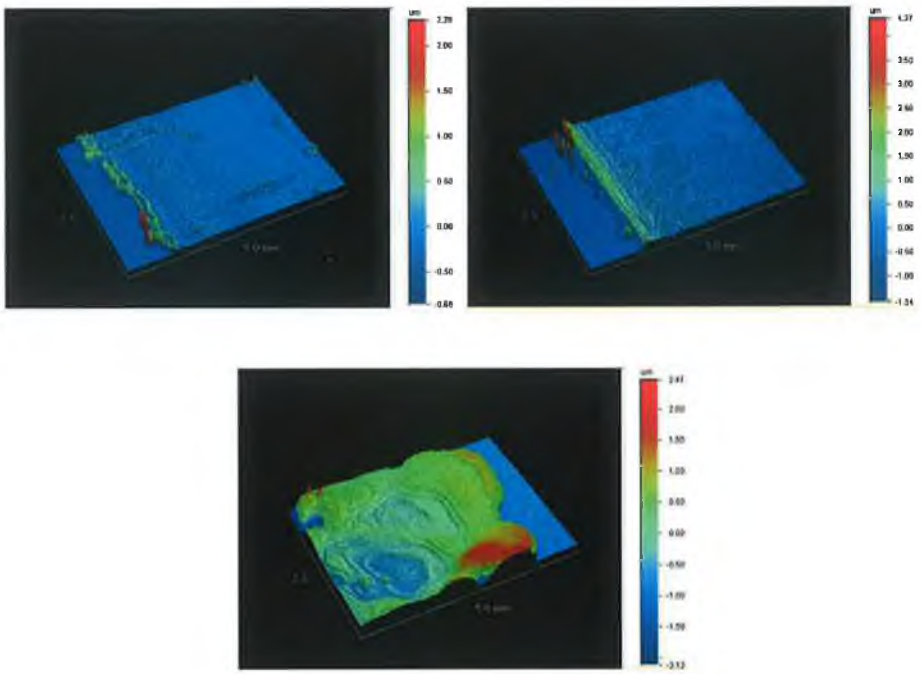

Figure 9.1: Surface profile images of layers produced by dip-coating (top left panel); spin-coating (top right panel) and stamp-coating (bottom panel)

is evident in the large standard deviation of $\pm$ 1.25 μm, a percentage error of 56 %.

The variation in thickness across the surface of samples produced by each of the deposition techniques, may be observed in Figure 9.1, which presents images of the samples obtained with a white light interferometer, (WYCO, N1100 Optical Surface Profiler). In these images, sample thickness is represented by colour. As expected from the standard deviation values in the thickness data above, the images in Figure 9.1, show that the samples produced by dip- or spin-coating (top left and right panels, respectively) show good uniformity in thickness across the surface, while the thickness of the stamp-coated sample is seen to vary considerably across the sample surface.

The sample-to-sample reproducibility of the O_2 response for each of the deposition techniques is compared by examining the Stern-Volmer plots of samples produced by each technique. Figure 9.2 presents the Stern-Volmer

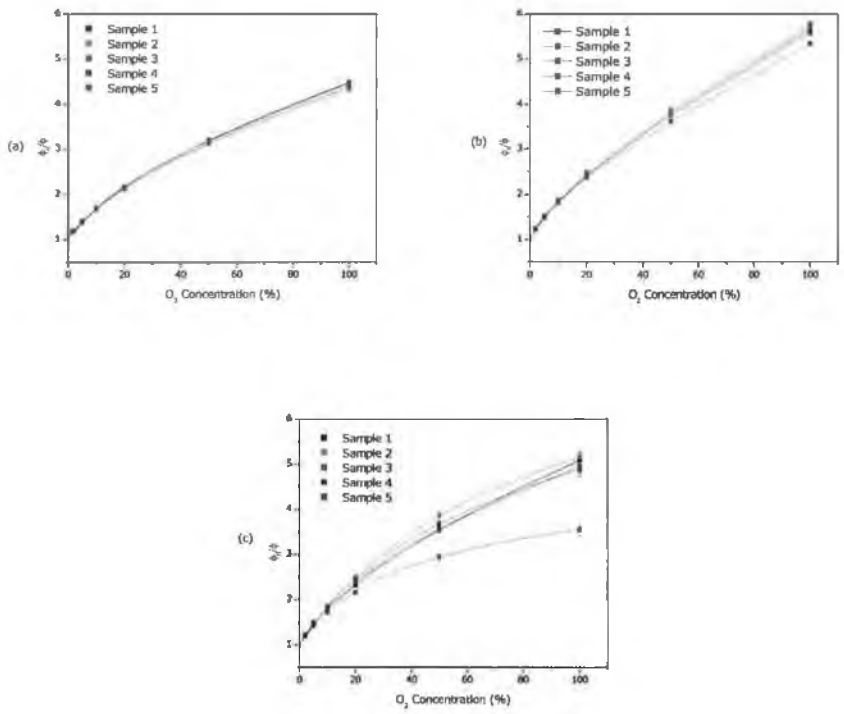

Figure 9.2: Stern-Volmer plots of layers produced by dip-coating (a); spin-coating (b) and stamp-coating (c)

plots obtained for samples produced by dip-coating, in Figure 9.2(a), spin-coating, in Figure 9.2(b), and stamp-coating, in Figure 9.2(c). The greatest reproducibility is observed for the dip-coated samples, exhibiting a standard deviation in K_{SV1} of 0.004 $[O_2]^{-1}$. The spin-coated samples yield a similar standard deviation in K_{SV1} of 0.008 $[O_2]^{-1}$. The stamp-coated samples present the greatest standard deviation in K_{SV1} of 0.014 $[O_2]^{-1}$, an order of magnitude greater than either of the other two deposition techniques. The reproducibility of K_{SV1}, which is a measure of the O_2 sensitivity, correlates with the sample-to-sample thickness reproducibility of the deposition techniques. This is as expected since layer thickness impacts on the diffusion path of the quencher molecules to the luminophores and so any spread in thickness contributes to a spread of the Stern-Volmer constant.

9.3 Pin-printing

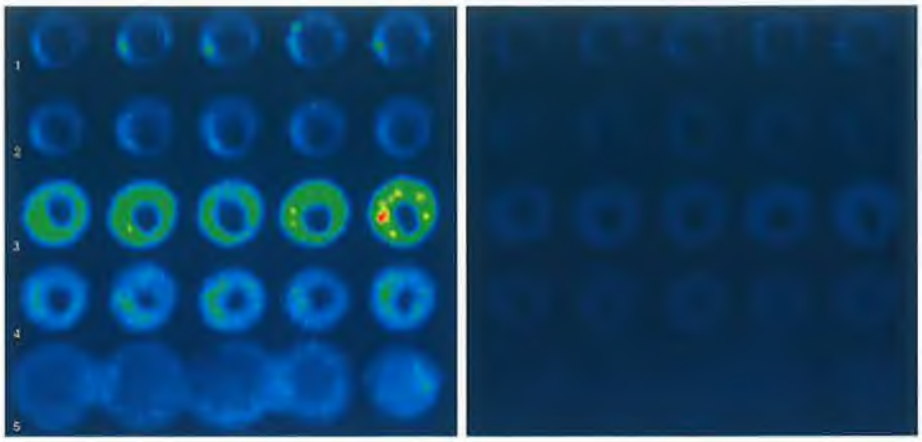

Figure 9.3: False colour CCD image of a pin-printed array under N_2 (left) and under O_2 (right)

Pin-printing is useful for high-throughput sol-gel film characterisation. Its operation allows for reservoirs to be filled with various sols. From these reservoirs, the pin on the robotic arm may pattern arrays of the different sols.

Figure 9.3, presents such an array, produced using sols of varying degrees of O_2 sensitivity. In Figure 9.3, a false-colour CCD-camera, has been used to image the intensity emitted from the array when it is flushed, first with N_2 (left panel) and then with O_2 (right panel).

Using this technique it is relatively quick and easy to determine which sol exhibits the greatest O_2 quenching efficiency, and also to determine which sols present deposition issues. For instance, the sol printed along the third row in the array clearly exhibits the largest degree of quenching when the environment is switched from N_2 to O_2. It is clear that the sols used in the first two rows allow for uniform, reproducible patterning of spots, while the sol used to print the last row, is clearly less suitable for patterning. Therefore this deposition technique allows for a quick assessment of a number of sols, from which an optimum sol may be selected for further characterisation [2].

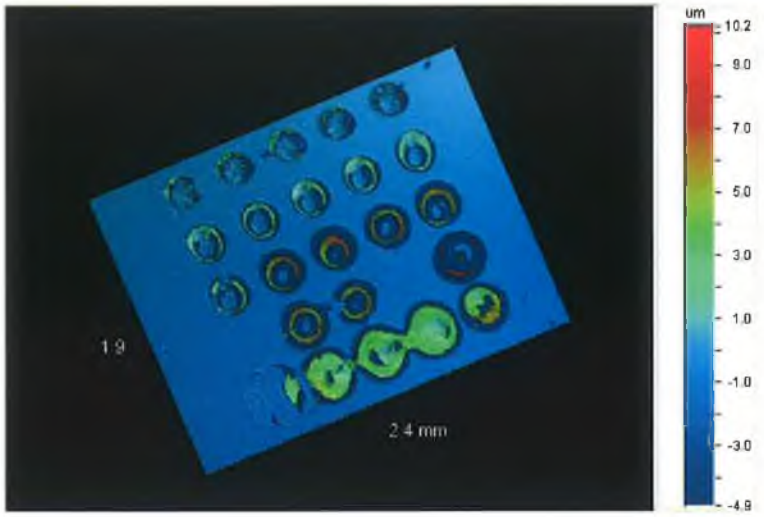

Figure 9.4: Surface profile of the pin-printed array

However, this technique cannot be relied upon to produce layers of uniform thickness. Figure 9.4 is an image obtained using the white light interferometer. This figure highlights the lack of uniformity in the thickness of the sensor spots deposited by pin-printing. It is possible however, that the technique used to pin-print liquid sol could be optimised to produce samples of improved uniformity.

9.4 Ink-jet-printing

Ink-jet-printing is an attractive technique due to the patterning possibilities this method presents. It has proved possible to deposit layers of sol-gel using an ink-jet print head. Discrete sol-gel spots may be ink-jet printed with excellent thickness uniformity across the surface.

Figure 9.5, presents an ink-jet-printed MTEOS-sol-gel layer, imaged by the white light interferometer. This figure highlights the uniformity of the layer's thickness. However, despite the results possible with ink-jet-printing, this method is not compatible with liquid sol-gels. This is on account of the evolving nature of sol-gel materials which continually age and eventually

form glassy materials which then clog and block the ink-jet print head.

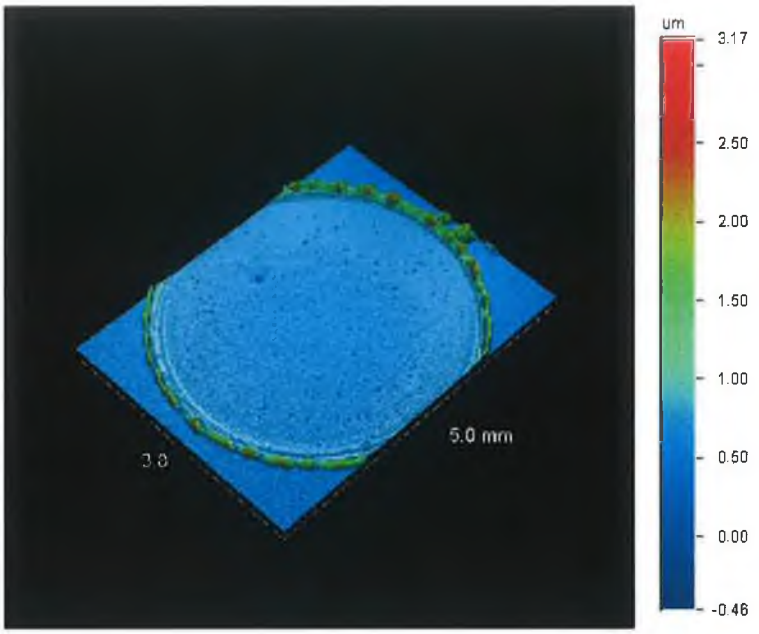

Figure 9.5: MTEOS-based sol ink-jet-printed on a glass substrate

9.5 Gravure-printing

Gravure-printing is a technique used for high-volume printing of fast-drying inks. Gravure-printing is the deposition technique used by the commercial company GSS [1]. This company produces O_2-sensitive sol-gel-based sensor elements printed on adhesive labels. For this work, GSS have provided two such samples, produced from an MTEOS-sol.

Figure 9.6, compares the Stern-Volmer plot obtained from each of the samples. In this figure, the Stern-Volmer plots overlap almost completely, indicating excellent reproducibly in O_2 sensitivity.

[1] GSS (Gas Sensing Solutions) is a DCU campus company that emerged from earlier sol-gel work in this group. See the company website for more information: http://www.gss.ie

Gravure-printing is particularly suited for use with liquid-sols as its non-contact technique overcomes the issues highlighted with ink-jet-printing, where the aging sol-gel material could clog and block the print head.

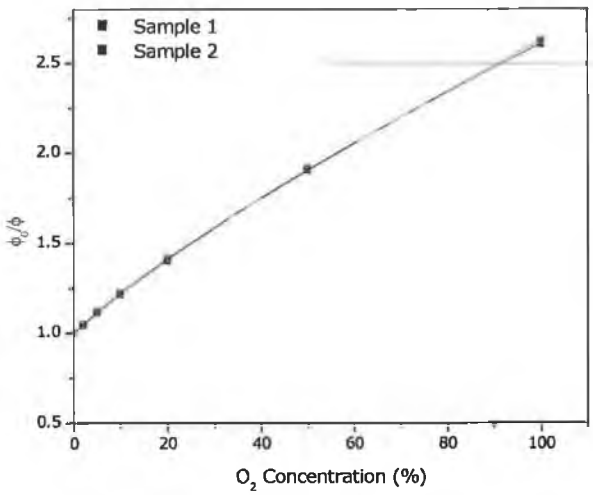

Figure 9.6: Comparing the Stern-Volmer plots of samples produced by gravure-printing

9.6 Conclusions

This chapter has summerised a number of deposition techniques. Dip-, spin- and stamp-coating have been presented as laboratory-based techniques. Good reproducibility in terms of layer thickness and O_2 response, is possible with both dip- and spin-coating. Stamp-coating has been shown to be much less reproducible.

Pin-printing has been presented as it offers the possibility of high-throughput testing techniques.

Ink-jet-printing, while producing good quality layers, has been found to be unsuitable for use with sol-gel liquids used in this work.

Gravure-printing is reported here as the industrial solution to sol-gel deposition. This technique has provided samples yielding excellent reproducibility in O_2 response.

Bibliography

[1] J. R. Lakowicz. *Principles of fluorescence spectroscopy*. Kluwer Academic/ Plenum Publishers, New York, 2nd edition, 1999.

[2] This work was carried out with Liz Tehan in the laboratory of Prof. F. V. Bright in the University at Buffalo.

Chapter 10

Conclusions

The overall aim of this thesis was the characterisation and optimisation of novel materials intended for luminescence-based O_2 sensing applications in the bio-pharm industry. The following list details the specific objectives required of this work (as outlined in Chapter 1) and how each was addressed in order to meet the ultimate goal.

- the O_2 sensitivity of sol-gel-derived sensor layers was optimised through the use of various organosilicon precursors. This approach was undertaken as the origin of O_2 sensitivity was found to lie with the transport of O_2 through the microstructure of the material. As the organic properties of the materials were altered, corresponding variations in the resulting O_2 response of that material were observed.

- O_2-sensitive materials capable of withstanding steam-sterilisation, without requiring recalibration, are a prerequisite for sensors intended for bio-fermenter applications. This was achieved through the use of the organosilicon precursor ETEOS, coupled with a curing program, which afforded the resulting glass the flexibility required to withstand the pressures within the autoclave.

- the performance of the sensor layers in the presence of ethanol was investigated, since this is a likely interferant in a bio-fermenter. All

sensor layers examined were found to experience an interference effect in the presence of ethanol. This was has been shown to be a function of the materials average pore size.

- the effects of photobleaching were countered through the use of the fluorinated organosilicon precursor TFP-TMOS. Using this precursor, a sol-gel-based material was produced which limited the effects of photobleaching. Such a material is suited to the prolonged periods of exposure to excitation light that are likely in long-term monitoring applications.

- O_2 sensing has been executed here via phase fluorometry. The implementation of this technique has been optimised. The advantage of the phase fluorometric technique has been outlined in this work, highlighting that this technique lends itself to miniaturisation and the use of low-cost electronic components, since the sensor platform will be designed for a commercial application.

Overall, this work has satisfied the industrial requirements by exploiting the versatility of the sol-gel route. Future work should include, optimising the R-value to produce membranes of suitable pore size in order to realise sensor layers immune to solvent cross-sensitivity. Following this, trails should be carried out to determine the performance of these sensor layers in the environment for which they are intended. These trials should include a comparison of O_2 sensitivity of these sensors during operation along side commercially available sensors. It is possible that some additional optimisation may be required following the field trials, however the sol-gel-based sensor layers should provide a real alternative to commercially available optical and electrochemical counter-parts.

In addition, multi-analyte possibilities can now be explored since deposition of the liquid sols in this work has proved possible with patterning techniques such as gravure-printing.

The two-site Demas model has been employed throughout this work as it sufficiently fits all the quenching data obtained from each of the samples

and so provides a platform for comparison. However, this model requires two-point calibration. The quenching data of some of the samples in this work can be well described by the single-site Stern-Volmer model. The fit to the Stern-Volmer model for PhTEOS-, ETEOS-, PTEOS- and OTEOS:TEOS-samples yields $R^2 \geq 0.98$, and so it would be interesting to pursue the implementation of single-point calibration sensors based on these materials.

List of Publications

Peer-Reviewed Publications

1. C. Higgins, D. Wencel, C.S. Burke, C. McDonagh and B.D. MacCraith. Novel hybrid optical sensor materials for breath analysis. (2007). *In Manuscript.*

2. D. Wencel, C. Higgins, A. Klukowska, B.D. MacCraith and C. McDonagh. Novel hybrid materials for bio-processing applications. Material Science, (2006). *Accepted.*

Conference Papers

1. J. Moore, C. Higgins, O. McGaughey and B. D. MacCraith. Exploiting cross sensitivity: achieving integrated temperature compensation via a dual-element optical oxygen sensor. Proc xxx. Optics East, 1-4 October 2006. *In Print*

2. D. Wencel, C. Higgins, C. McDonagh and B.D. MacCraith. Novel hybrid materials for smart sensor windows. Proc. S.P.I.E., 5826B-91, Opto-Ireland, 4-6 April (2005).

Oral Presentations

1. Novel hybrid sol-gel films for luminescence-based optical sensing. UK-Ireland Sol-Gel Conference, Institute of Physics, London, UK. 22 March 2005.

Posters

1. J. Moore, C. Higgins, O. McGaughey and B.D. MacCraith. Exploiting cross sensitivity: achieving integrated temperature compensation via a dual-element optical oxygen sensor. BOC Poster Competition, School of Physics, Dublin City University. 14 September 2006.

2. D. Wencel, C. Higgins, A. Klukowska, B.D. MacCraith and C. McDonagh. Novel hybrid materials for bio-processing applications. 4th International Conference on Sol-Gel Materials, Kliczkow Castle, Poland. 18-22 June 2006.

3. C. Higgins, D. Wencel, C.S. Burke, A.K. McEvoy, C. McDonagh and B.D. MacCraith. Novel optical sensor materials for breath analysis. Europt(r)ode VIII, Tubingen, Germany. 2-5 April 2006.

4. D. Wencel, C. Higgins, C. McDonagh and B.D. MacCraith. Novel sol-gel based films for pH and oxygen Sensing. 13th International workshop on Sol-Gel Science and Technology University of California, Los Angeles, U.S.A. 22-26 August 2005.

5. D. Wencel, C. Higgins, C. McDonagh and B.D. MacCraith. Novel hybrid materials for smart sensor windows. Opto-Ireland, RDS, Dublin. 4-6 April 2005.

6. C. Higgins, A. Guckian, C. McDonagh, B.D. MacCraith and J.G. Vos. Novel hybrid materials for luminescence-based sensing. Europt(r)ode VII, Madrid, Spain. 4-7 April 2004.

7. C. Higgins, P. Bowe, A.K. McEvoy, C. McDonagh, B.D. MacCraith and F.V. Bright. Novel hybrid sol-gel films for optical sensing. UK-Ireland Sol-Gel Conference, Cranfield University, UK. 2003.

Training, Collaborations, Misc.

1. Hobra JobinYvon - Spectroscopic ellipsometry training course, Paris, France. (2005)

2. Outward research visit to the lab of Prof. Frank V. Bright, University of Buffalo, State University of New York, U.S.A. (2004)

3. Participated in ASCOS (Advanced Study Course on Optical Chemical Sensors) Sicily, Italy. (2004)